2008

Internal cooling in ribbed rectangular (AR=4:1) passages at high rotation numbers and improvement in finning strategies

Fuguo Zhou
Louisiana State University and Agricultural and Mechanical College

INTERNAL COOLING IN RIBBED RECTANGULAR (AR=4:1) PASSAGES AT HIGH ROTATION NUMBERS AND IMPROVEMENT IN FINNING STRATEGIES

A Dissertation

Submitted to the Graduate Faculty of the
Louisiana State University and
Agricultural and Mechanical College
In partial fulfillment of the
Requirements for the degree of
Doctor of Philosophy

In

The Interdepartmental Program in Engineering Sciences

By
Fuguo Zhou
B.S., Beijing University of Aeronautics and Astronautics, 1985
M.S., Beijing University of Aeronautics and Astronautics, 1988
M.S., Louisiana State University, 2007
August 2008

ACKNOWLEDGEMENTS

I would like to express my sincere gratitude and appreciation to my Graduate Advisor, Prof. Sumanta Acharya, for his sponsoring and guiding my studies and research. Without his support and patient guidance, this work cannot be done.

I would also like to sincerely thank Prof. Dimitris Nikitopoulos, Prof. John Tyler, Prof. Guoli Ding and Prof. Bin Li for their kindly serving in my graduate academic committee.

Special thanks are due to Mr. Jonathan Lagrone, Mr. Barry Savoy, Mr. Jim Layton and Mr. Charlie Smith for their friendly assistance in the lab and machine shop.

TABLE OF CONTENTS

NOMENCLATURE

A	area
Bo	buoyancy parameter, $DR*Ro^2*R/D_h$
C_p	specific heat
D	diameter
DR	coolant to wall density ratio at the inlet, $(\rho_w - \rho_b) / \rho_w = (T_w - T_b)/T_w$
F	force
f	average friction factor
H	the height of the channel cross-section, these two walls are smooth
h	heat transfer coefficient
I	current applied to heater
k	heat conductivity of air, or 1000 in representing Re values
L	channel length
$\dot{m}$	mass flow rate
Nu	Nusselt number
P	pressure, or rib pitch
Pr	Prandtl number
ΔP	pressure drop
q	heat transferred through copper element
q''	heat flux per unit area
R	resistance of heater, or rotating radius

Re Reynolds number, $\rho V D/\mu$

Ro Rotation number, $\Omega D_h / V$

T temperature

TPF thermal performance factor, $(Nu/Nu_0)/ (f/f_0)^{1/3}$

V average velocity

W the width of the channel cross-section, ribs are located on these two walls

X distance along streamwise direction

Ω rotational speed

ρ density of air

ν kinematics viscosity

Subscripts

0 smooth conditions, or start time of test

b bulk value

h hydraulic

i the i-th copper plate

τ time, τ=0 when test starts

w wall

ABSTRACT

Experimental studies have been performed on two-pass rectangular internal coolant channels with aspect ratio AR 4:1 with high rotation numbers. Three passages are investigated: smooth, 90 deg ribbed and 45 deg ribbed. A maximum Reynolds number of 150,000 and a maximum rotation number of 0.6 are achieved in the study. These maximum parameter values are considerably higher than those previously reported for the 4:1 AR geometry, and provide data for parameter ranges that may be representative of certain modern turbine blades. Heat transfer behaviors with rotation in the three passages are presented. Rotation effects, density effects and buoyancy effects are discussed. Friction factors and thermal performance factors are also provided. In addition, innovative finning strategies are proposed and tested in a straight stationary rectangular channel using transient crystal method aiming to enhance the heat transfer rate of heat exchangers. The test results show an overall heat transfer rate of 3 and above for Reynolds numbers up to 65,000.

CHAPTER 1

INTRODUCTION

1.1. Background

Efforts to increase the efficiency of turbines often include increasing the turbine inlet temperature. In order to combat these higher temperatures demands on the first-stage vanes and blades, more effective and innovative cooling techniques have been studied. One of the most widely employed techniques for blade cooling is to circulate coolant air through internal cooling passages within the turbine blade. Maximizing the cooling efficiency of such passages and attempting to accurately quantify the performance of these passages for parameters relevant to engine operating conditions has been the primary focus of many researchers for several decades. As a result, many studies have focused attention on different cross-sectional geometries, turbulator configurations, and flow parameters for both stationary and rotating internal coolant passages. These studies have provided insights on the effect of Coriolis and centrifugal-buoyancy forces on the flow and heat transfer characteristics for specific cooling strategies, and have provided insight for implementing more reliable and/or effective internal-cooling strategies.

Figure 1.1(a) shows a typical turbine blade used in industry. The temperature of the incoming hot gas is well above material limits of the blade, therefore; in order to protect the blade from this harsh environment effective cooling techniques must be employed.

As shown in Figure 1.1(a), multiple cooling techniques are employed in modern turbine blades including film cooling on the external turbine blade surface, impingement cooling inside the leading edge, pin-fin cooling inside the trailing edge, and ribbed turbulated cooling in the internal passages inside the main body of the blade.

The top of Figure 1.1(b) shows the turbine blade airfoil. Constrained by the airfoil geometry, the cross-sections of the coolant passages in the turbine blade airfoil range from tall, narrow passages (low aspect ratio) in the thickest portion of the turbine blade airfoil, to short, wide passages (high aspect ratio) in the trailing edge.

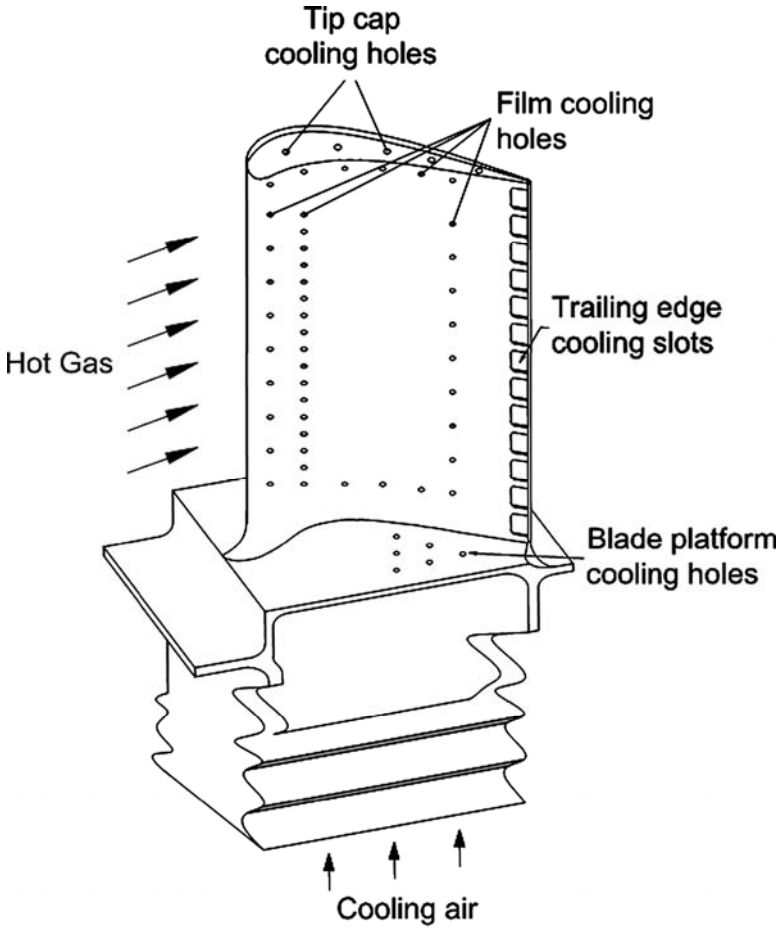

(a) A typical turbine blade

Figure 1.1: Turbine blade and cooling techniques (From Han et al.[23], Figure continued)

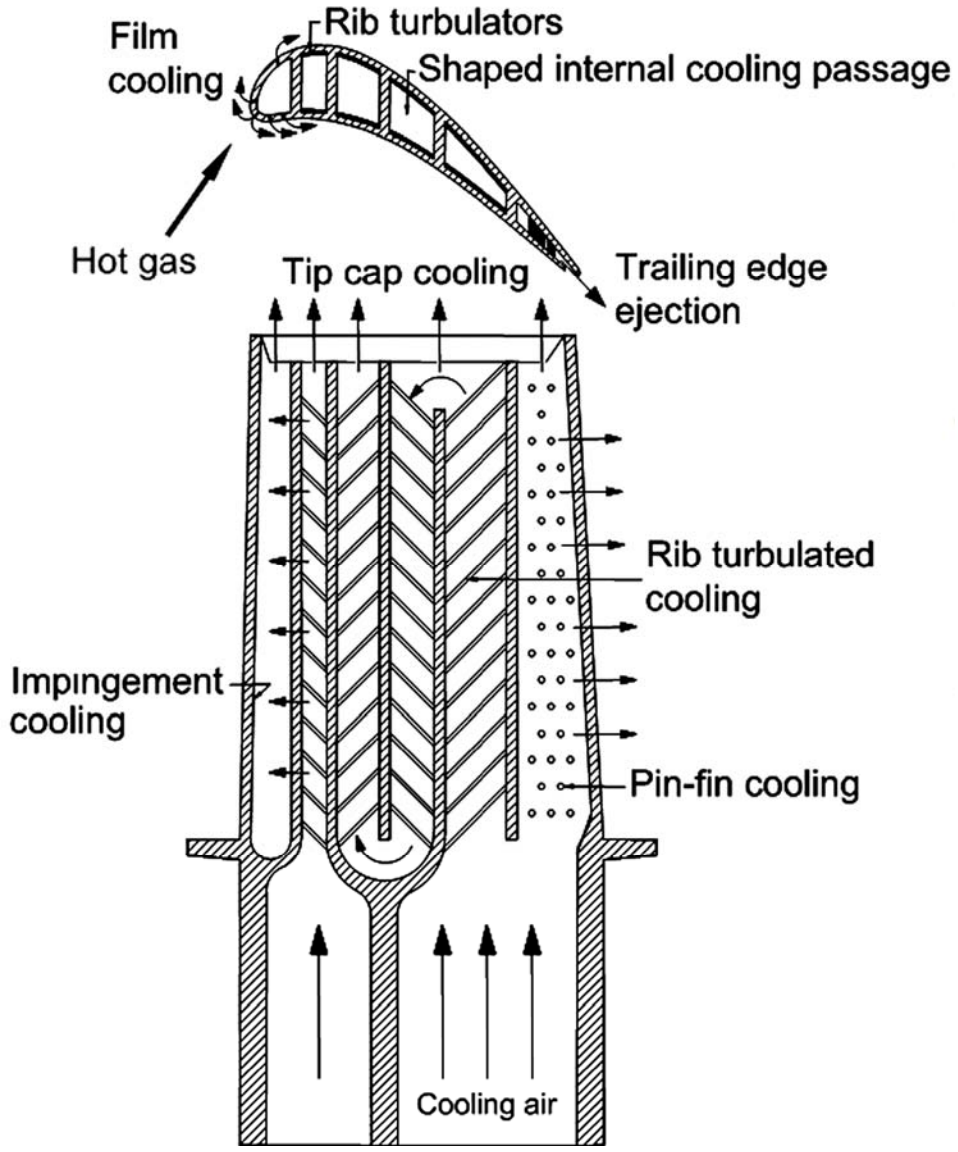

(b) Cross-sectional view of a turbine blade

1.2. Major Flow Patterns Involved

Three major types of secondary flow are present in internal coolant passages. Coriolis force, buoyancy force, and rib geometry all induce secondary flows which affect the heat transfer characteristics of the serpentine passages.

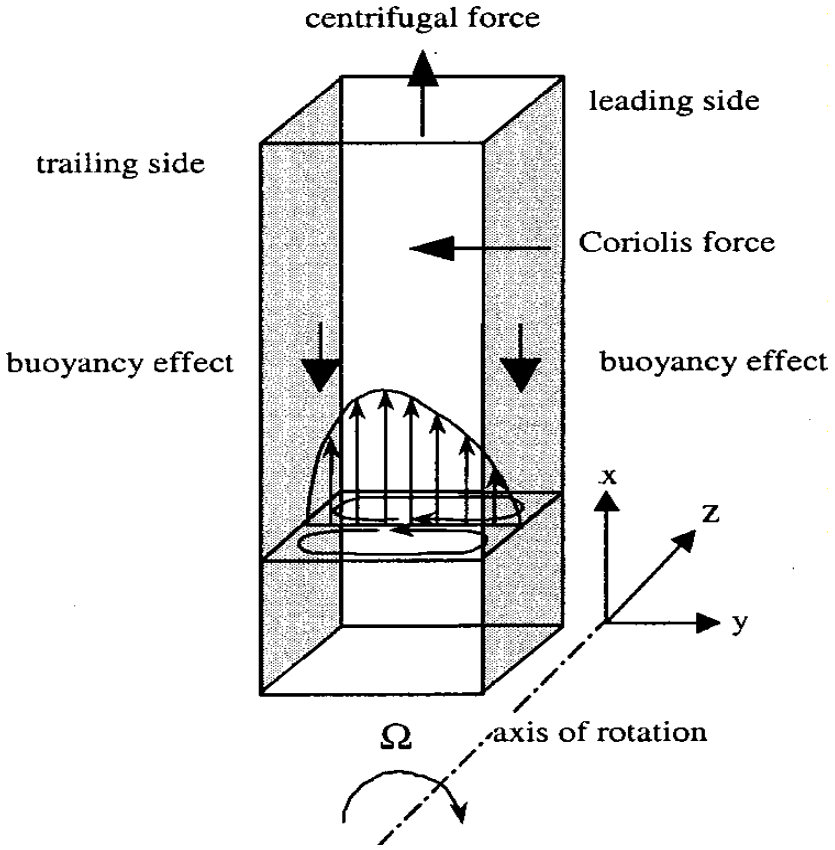

(a) Schematic of a rotating channel with radially outward flow (From Willett et al. [18])

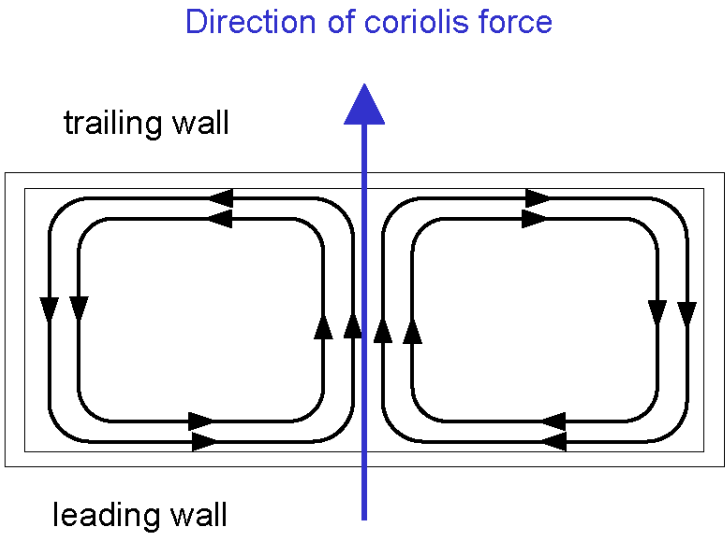

(b) Coriolis force induced secondary flow cells

Figure 1.2: Coriolis force induced secondary flow in a rotating channel

(a) Coriolis Force Induced Secondary Flow

As shown in Figure 1.2 (a), air flows from the bottom of the channel to the top as the channel rotates clockwise. The Coriolis force generated by this radial flow points from the leading wall to the trailing wall as shown if Figure 1.2 (b). If the flow direction reverses, then the Coriolis force will point from the trailing wall to the leading wall.

(b) Rotational-Buoyancy Force Induced Secondary Flow

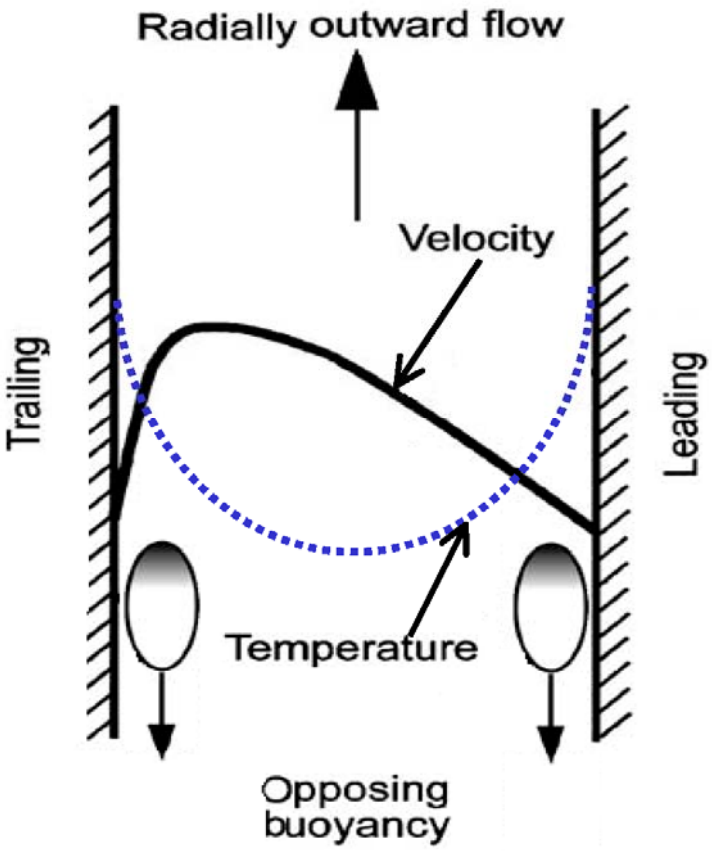

Figure 1.3: Rotational-buoyancy induced secondary flow (From Murata et al. [37])

The relevant buoyancy force in internal turbine blade flows is not due to gravity but centripetal acceleration from rotation, which can be hundreds or thousands times the earth's gravitational force. Like gravity-induced buoyancy, the rotational buoyancy also

depends on the density variation of the flow; therefore, there will be no rotational buoyancy induced secondary flow if the air density is uniform regardless of rotational speed.

Rotational buoyancy characterized by $Bo=DR\ Ro^2\ (R/D_h)$, which contains both the rotation number, $Ro=\Omega D_h\ /V$, and flow density ratio, $DR=(\rho_w - \rho_b)\ /\ \rho W = (T_w - T_b)/T_w$.

The rotational buoyancy force may act in a direction opposite that of the main flow (opposing buoyancy, as shown in Figure 1.3), or may be in the same direction (aiding buoyancy) as the main flow, depending on the flow direction. In general the direction of buoyancy induced secondary flow also depends on whether the flow is cooling or heating the channel, however only cooling is relevant for this study.

(c) Ribs Induced Secondary Flow

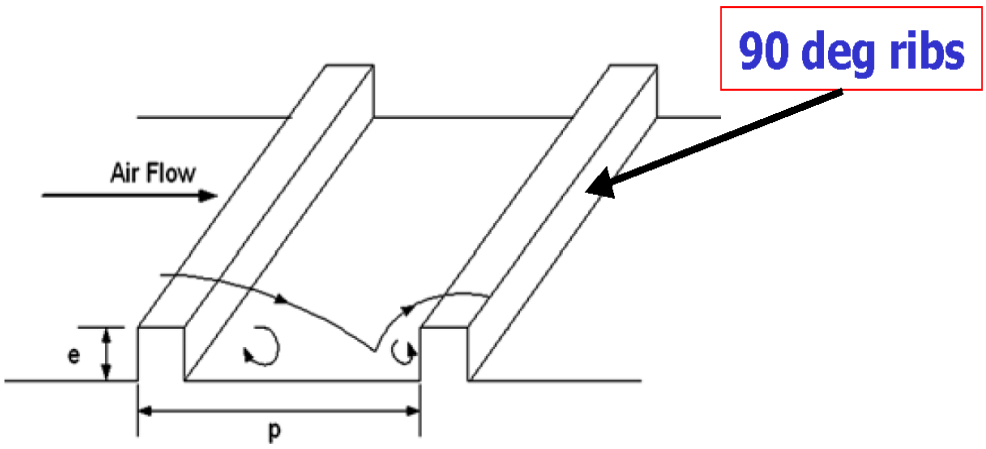

(a) Flow separation and reattachment around 90 deg ribs

Figure 1.4: Schematic of ribs induced secondary flow (Figure continued)

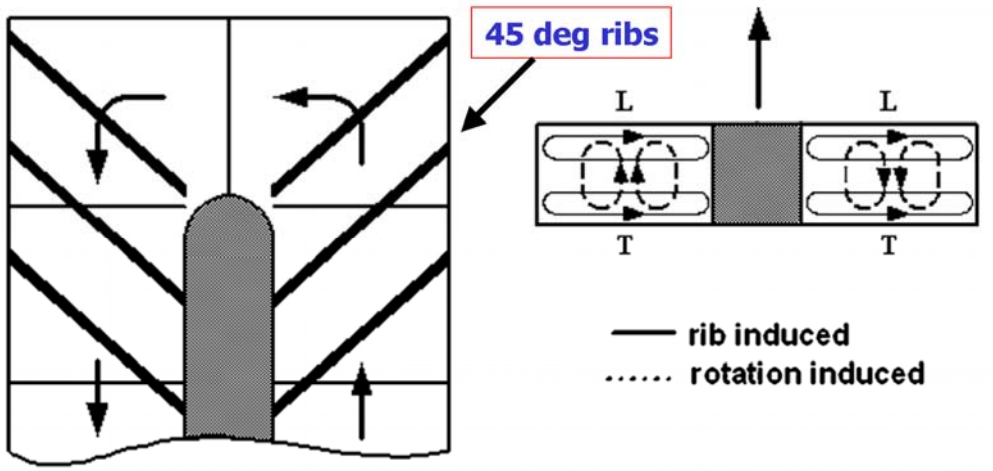

(b) Secondary flow developed along 45 deg ribs (From Al-Hadhrami et. al [72])

In the ribbed passages, the ribs also induce secondary flows. As air flows over perpendicular ribs, flow separation and reattachment occurs on and after each rib. In the case of skewed ribs, an additional secondary flow develops along the ribs.

The strength of each different secondary flow pattern changes with variations in rotation speed, flow conditions, and wall boundary conditions. These secondary flows interact with and influence each other. As a result the flow through the internal channels of turbine blades are quite complex and the heat transfer characteristics on each of these walls are unique.

1.3. Force Analysis

For stationary case, which is a classical fluids problem, only two forces are involved: the inertial force, $F_{inertial}$, and the viscous force, $F_{viscous}$ (constant coefficients are omitted in the formulas).

$$F_{inertial} = \rho \cdot V^2 \cdot D_h^{\,2} \qquad (1)$$

$$F_{viscous} = \rho \cdot \nu \cdot V \cdot D_h \qquad (2)$$

The ratio of $F_{inertial}$ to $F_{viscous}$ can be represented by Reynolds number Re.

$$\frac{F_{inertial}}{F_{viscous}} = \frac{\rho \cdot V^2 \cdot D_h^{\,2}}{\rho \cdot \nu \cdot V \cdot D_h} = \frac{V \cdot D_h}{\nu} = \mathrm{Re} \qquad (3)$$

For rotational case, two more forces act on the coolant flow: the Coriolis force, $F_{coriolis}$, and the rotational buoyancy force, $F_{buoyacy}$ (constant coefficients are omitted in the formulas).

$F_{buoyancy} = g_{rotational} \cdot \Delta\rho \cdot D_h^{\,3}$, where $g_{rotational}$ is the centripetal acceleration:

$g_{rotational} = \Omega^2 \cdot R$, thus

$$F_{buoyancy} = \Omega^2 \cdot R \cdot \Delta\rho \cdot D_h^{\,3} \qquad (4)$$

$$F_{coriolis} = \rho \cdot \Omega \cdot V \cdot D_h^{\,3} \qquad (5)$$

The ratio of rotational buoyancy force $F_{buoyacy}$ to viscous force $F_{viscous}$ is rotational Grashof number.

$$Gr_{rotational} = \frac{F_{buoyancy}}{F_{viscous}} = \frac{\Omega^2 \cdot R \cdot \Delta\rho \cdot D_h^{\,3}}{\rho \cdot \nu \cdot V \cdot D_h} = \mathrm{Re} \cdot Ro^2 \cdot DR \cdot \frac{R}{D_h} \qquad (6)$$

The ratio of rotational buoyancy force, $F_{buoyacy}$, to inertial force, $F_{inertial}$, is rotational buoyancy number, Bo (the equivalent of Gr/Re^2 in the stationary, gravity-driven buoyancy problem).

$$Bo = \frac{F_{buoyancy}}{F_{inertial}} = \frac{F_{buoyancy} \big/ F_{viscous}}{F_{inertial} \big/ F_{viscous}} = \frac{Gr_{rotational}}{\mathrm{Re}} = \frac{\mathrm{Re} \cdot Ro^2 \cdot DR \cdot R}{D_h \cdot \mathrm{Re}} = \frac{R}{D_h} \cdot DR \cdot Ro^2 \qquad (7)$$

Similarly, the ratio of Coriolis force $F_{coriolis}$ to inertial force $F_{inertial}$ is rotation number Ro.

$$Ro = \frac{F_{coriolis}}{F_{inertial}} = \frac{\rho \cdot \Omega \cdot V \cdot D_h^{\,3}}{\rho \cdot V^2 \cdot D_h^{\,2}} = \frac{\Omega \cdot D_h}{V} \tag{8}$$

The ratio of rotational buoyancy force $F_{buoyacy}$ to Coriolis force $F_{coriolis}$ can be expressed as

$$\frac{F_{buoyancy}}{F_{coriolis}} = \frac{\Omega^2 \cdot R \cdot \Delta\rho \cdot D_h^{\,3}}{\rho \cdot \Omega \cdot V \cdot D_h^{\,3}} = \frac{\Delta\rho}{\rho} \cdot \frac{\Omega \cdot D_h}{V} \cdot \frac{R}{D_h} = \frac{R}{D_h} \cdot DR \cdot Ro \tag{9}$$

1.4. Literature Review

(a) Internal Cooling with Smooth Channels

The early research focused mainly on straight, smooth, tubes with a circular cross-section [1-3]. Later, smooth ducts with a square cross-section received extensive attention. For example, Wagner et al. [4] reported detailed measurements in a rotating smooth, square cross-sectional channel. Their study investigated the effects of rotation, density ratio, and Reynolds number. The results showed that rotation has significant effect on heat transfer. By varying the rotation number from 0 to 0.48, the heat transfer ratio on the pressure side (trailing wall) steadily increased, and at a rotation number of 0.48, the heat transfer ratio was 350 percent higher than the stationary case. However, the heat transfer ratio on the suction side (leading wall) demonstrated more complex behavior. Initially the heat transfer ratio decreased as the rotation number increased, but beyond a critical rotation number (depending on the density ratio and streamwise location) the heat transfer ratio increased with rotation number. Heat transfer on sidewalls (walls parallel to the plane of rotation) experienced only slight changes. Increases in density ratio were found to enhance heat transfer ratios of both leading and trailing walls.

Wagner et al. [5] then studied a serpentine, smooth, square cross-section rotating channel. The heat transfer ratio in the bends was found to be nearly double the value of the fully developed straight sections. Mochizuki et al. [20] also conducted experiments in a smooth serpentine square channel with rotation. Their results also showed that the heat transfer ratios in the bend regions were about twice the values in the straight legs of the channel. In addition, their results showed that the heat transfer ratios in the second and third legs were higher than in the first leg due to the bend effects.

(b) Internal Cooling with Ribbed Channels

- **Stationary Ribbed Channels**

Rib turbulators, or trip strips, are the most intensively studied turbulence promoters used in the turbine internal cooling passages. A great number of experimental and numerical studies have been carried out to investigate the effects of ribs on heat transfer in internal channels. The factors considered in the studies include the rib geometry (the cross-sections of the ribs), the rib configuration in the channel (the angle of attack of the ribs and the relative distance between the ribs), the shape and the aspect ratio of the cross-section of the channel, the rotation of the channel, the turn or bend effects of the channel (multi-pass serpentine channels), and orientations of rotating channels with respect to the axis of rotation. The early investigations focus primarily on straight, stationary, ribbed channels with a square or rectangular cross-section. By measuring the wall temperature and flow temperature using thermocouple, Han et al. [21, 22] carried out extensive experimental studies on stationary ribbed channels and identified that heat transfer rate in stationary ribbed channels primarily depends on the flow Reynolds number, the rib spacing, the rib angle, and the pitch to height ratio of ribs,

and the channel aspect ratio. Heat transfer, friction factor, and thermal performance factor were presented. The experimental results showed that the heat transfer on the ribbed walls doubled or increased more compared to the smooth channel; and the skewed ribs promoted higher heat transfer than ribs normal to the main flow. The best heat transfer performance was obtained in the square channel with rib angle of attack from 30 to 45 deg.

Han and Zhang [24] further investigated the heat transfer characteristics of internal air flow in a three-pass square channel by employing the naphthalene sublimation method. The test section consisted of three straight square channels connected by two 180-deg bends. The rib height-to-hydraulic diameter ratio was 0.063; the rib pitch-to-height ratio was 10. Two angles of attack, 60 deg and 90 deg, were studied. For the 60 deg case, both the cross ribs and the parallel ribs on two opposite walls of the cooling channel were investigated. It was found that the rib angle, the rib configuration, and the bend significantly affected the local heat/mass transfer distributions; the 60 deg ribs provided higher heat/mass transfer coefficients than the 90 deg ribs; and the parallel ribs generated higher /mass transfer coefficients than the cross ribs.

Liou et al. [25, 26], Taslim et al. [27, 28] and Acharya et al. [29] also studied the heat transfer and flow filed in the ribbed channels. Liou et al. found that the rib pitch-to-height ratio of 10 resulted in the best heat transfer; the heat transfer showed a periodic behavior between consecutive ribs; and both heat transfer and friction factor increased with decreasing rib spacing. Taslim et al.[27] confirmed Han et al.'s findings that skewed (45 deg) ribs produced higher thermal performance factor than transverse (90 deg) ribs. Taslim et al. [28] further placed ribs on all four walls of square and trapezoidal channels, and found that the heat transfer coefficients and thermal performance factors were

enhanced compared to the channels with ribs only on two opposite walls. Acharya et al. [29] experimentally investigated the flow and heat transfer in a rectangular channel with ribs attached along one wall. Their results also showed the periodic heat transfer profile induced by the ribs. The measured flow field revealed separation regions downstream the ribs followed by reattachment and redevelopment regions.

- **Ribbed Channels with Rotation**

Due to the fact that the turbine blades in practical use always rotate with high speed, so the rotation effects on the ribbed passages also received many researchers' studies [6, 7, 13, 30-32]. Taslim et al. [30] studied a rotating, straight, square cross-section channel with two opposite rib-roughed walls and with radially outward flow. The ribs were made in a parallel staggered fashion with 90 deg to the main flow. Liquid crystals were used to determine heat transfer coefficients. A maximum increase in heat transfer coefficient of about 45% over that of the stationary case on the trailing surface, and a minimum decrease of 6% on the leading surface were reported for the parameters covered in the experiment. Griffith et al. [13] experimentally studied straight, smooth and 45 deg ribbed, rectangular models of AR = 4:1 in the parameter range of Ro = 0.305 at Re = 5,000 to Ro = 0.038 at Re = 40,000. In this study, particular care was taken to identify the variations of heat transfer along the spanwise direction of the ribbed walls. This was accomplished by installing two parallel rows of insulated copper plates on both leading and trailing surfaces along the streamwise direction. Their results showed that on one row the heat transfer was higher than that on the other row at the same streamwise location. Wagner et al. [6] and Johnson et al. [7] further studied serpentine, square cross-sectional rotating channels with ribs on the trailing and leading walls. The ribs were normal (90 deg) or skewed (45 deg) to the flow. For both rib orientations, the rib pitch-to-

height ratio, P/e, was 10, and the rib height-to channel hydraulic diameter ratio, e/D_h, was 0.1. Their results for the two rib orientations showed that heat transfer increased by more than 200% as compared with the corresponding cases on the smooth model; and the rotation effects on the ribbed passages generally augmented the heat transfer on the trailing walls but degraded the heat transfer on the leading walls in the radially outward flow, and vice versa in the radially inward flow, however, the increase and the decrease trends in heat transfer were not monotonic.The nature of rotation effects on the internal cooling flow is basically the effects of Coriolis force on the rotating radially flow when no heat transfer occurs. Hart [31] and Johnston et al. [32] revealed this fact in the early 1970s in rotating smooth channels by flow visualization, flow field measurement and theoretical analysis. Hart [31] observed a formation of secondary flow in the form of paired, longitudinal vortices that drive fluid away from the leading wall toward the trailing wall. Based on the theoretical analysis on the momentum and vorticity equations for rotating channel flow, Hart [31] concluded that the secondary flow was the result of Coriolis force. Johnston et al. [32] observed as well the longitudinal secondary circulation within the rotating channel. They further pointed out that Coriolis force generally acts to stabilize the leading wall boundary layer, but destabilize that on the trailing wall. As the results, the wall shear stress in the destabilized region was greater than the non-rotating value, and consequently, shear stress along the stabilized wall was reduced. When heat transfer occurs on the walls of a rotating channel, the density gradient of the flow close to the wall coupled with the centrifugal force produces the rotational buoyancy force. This buoyancy force is another factor of rotation effects in the rotating channel. Figure 1.2 shows a pictorial view of rotation effects on the radially outward flow in a rotating channel with the Coriolis force and rotational buoyancy force.

As seen in the review above, the experimental studies on the internal cooling channels mainly focus on the square channels. The rectangular channels with different aspect ratios receive fewer attentions.

- **Numerical Predictions**

Extensive numerical investigations were performed to help understand the flow mechanisms behind the experimental heat transfer results. Acharya et al. [33] used the standard high Reynolds number k-ε turbulence model and nonlinear k-ε turbulence model to predict the details of turbulent flow in a stationary, periodically rib-roughened channel. The turbulent shear stress at different locations between the ribs was obtained.

Dutta et al. [34] performed a numerical stimulation using a modified k-ε model on a rotating, straight, smooth, square channel. Both Coriolis force and rotational buoyancy force were included. Their results showed how flow can separate on the smooth leading wall under the combined effects of Coriolis and rotational buoyancy forces.

Iacovides et al. [10] and [14] carried out numerical studies on an AR=2:1, straight, rectangular channel under rotation. Their results revealed that at low rotation numbers Coriolis forces induced a pair of symmetric streamwise vortices. The vortices pair could be transitioned to a more complex four-vortex structure at high rotation numbers due to the flow instability on the pressure wall.

Saha et al. [35] studied the heat transfer in rotating straight channels with AR of 1:4, 1:1 and 4:1 by solving the Unsteady Reynolds Averaged Navier-Stokes (URANS) equations. The channels were all roughened with 90 deg ribs. The results for the 4:1 AR duct showed evidence of multiple rolls in the secondary flow that directed the core flow to both the leading and trailing surfaces. Therefore, the difference between the heat transfer on the leading and trailing walls in the 4:1 AR duct is not significant, unlike the

other two aspect ratios. The average Nusselt number (on all walls) was found to be the highest for the 4:1 case.

Murata et al. [36] numerically investigated centrifugal buoyancy effects on heat transfer in a rotating two-pass square smooth channel by using the large eddy simulation. The effect of the aiding/opposing buoyancy contributions was seen in by different longitudinal vortex structures near the pressure surface depending on the radial flow direction and in larger buoyancy-induced variation of the heat transfer ratio on the pressure surface than that on the suction surface. Murata et al. [37] further studied the centrifugal buoyancy effects on heat transfer in a rotating two-pass square rib-roughened channel with by the same approach. By applying uniform heat flux wall condition, aiding or opposing buoyancy was observed along leading or trailing wall, depending on the main flow direction (radially outward or radially inward). Both computations were based on the wall condition of uniform heat flux, and Reynolds numbers were less than 6,000.

Sleiti et al. [38] and [39] carried out numerical investigation on heat transfer in the rotating, smooth and ribbed internal square channels using RSM turbulence model. The major objectives of these researchers were to study the heat transfer behaviors in the rotating square channels at high rotation numbers and high density ratios. The authors first validated the reliability of the computational method by comparing their results with the experimental results of Wagner et al. [5] and [6]. In selected cases, the computed and experimental heat transfer matched very well. The numerical method was used to predict heat transfer at higher values of Ro (up to 1) and DR (up to 0.3) at a Re=25000.

(c) Internal Cooling with Dimpled Surfaces

- **Early Works in the Former Soviet Union**

Dimples are arrays of depressions or indentations on surfaces. Figure 1.5 shows

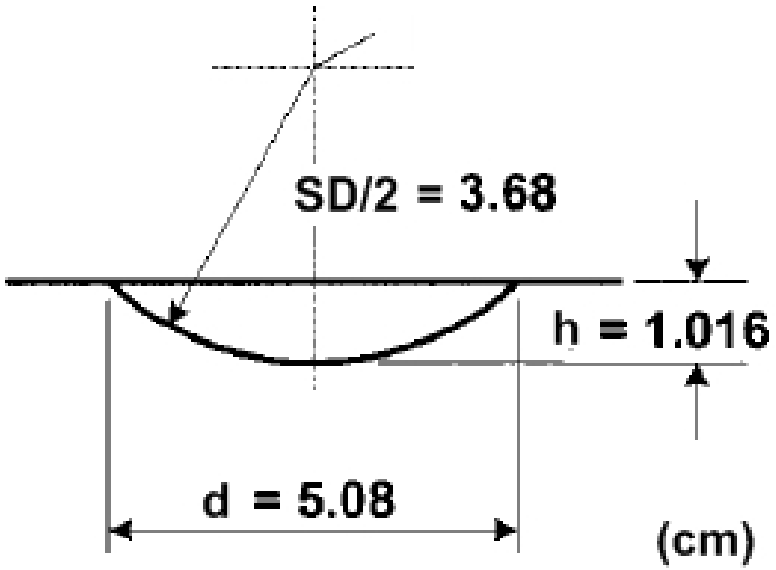

(a) Individual Dimple

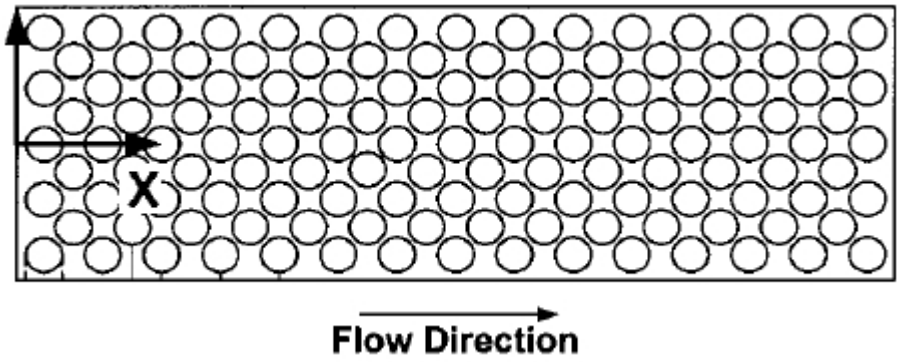

(b) Dimple Arrays

Figure 1.5: Typical Schematic Diagrams of Individual Dimple and Dimple Arrays Arrangement (From Burgess et al. [50])

typical schematic diagrams of a spherical dimple and dimple arrays. Dimpled channel is attractive from a turbine blade cooling perspective, because it is expected that, just like ribs, dimples generate strong vortices when dimples are placed in flow, the vortices then produce higher turbulence around the dimples and in the downstream area of the dimples, thus

augment heat transfer. Moreover, dimples should produce lower pressure drop than ribs, because dimples do not protrude into the flow to induce any form drag.

For these reasons, several investigators have explored the use of dimpled internal coolant turbine blade passages. The first known published research on the flow structure and heat transfer characteristics of dimples are from the former Soviet Union, according to Ligrani et al. [40, 41].

Of these early studies, Schukin et al. [42] studied the effects of channel geometry (constrictor and diffuser channels) on the heat transfer downstream of a single hemispherical dimple with sharp edge; the effect of the turbulence intensity (Tu_∞) in the main flow on the dimple heat transfer was also studied. The diameter of the dimple (d, the diameter of the cavity circle on the surface) is 0.50 mm, and the ratio of depth to diameter (h/d) is 0.5. For the whole range of the constrictor/diffuser angle $\theta/2 = 0$ to 8.5°, the heat transfer coefficient increase to 1.2 times of that on the smooth surface without dimple at Re=140,000. Their results on a dimple of d=150 mm and h/d = 0.5 showed that the dimple enhanced the heat transfer when $Tu_\infty<15\%$, but dimple made no difference in heat transfer for when $Tu_\infty \geq 15\%$.

Terekhov et al. [43] experimentally studied the flow structure, pressure field, and heat transfer in a channel with a single dimple on one wall. Two types of dimple were tested: with a sharp edge and with a rounded off edge. The value of h/d was 0.13, 0.26 and 0.5. The velocity field was measured using LDA, and flow visualization was achieved by use of hydrogen bubbles. Heat transfer measurement was also done within the dimple. The authors claimed that auto oscillations of the flow arose in the dimple for

all the test conditions; pressure loss increased as the depth of dimple increased. The experimental results showed clearly that the heat transfer was stronger in the downstream half of dimple than in the upstream half.

- **Recent Works in the United States**

Chyu et al. [44] reported an experimental study on heat transfer, using transient liquid crystal method, on surfaces with staggered dimple arrays in rectangular channels of aspect ratio of 2, 4 and 12. Hemispheric dimple and teardrop shaped dimple were investigated. The depth to diameter ratio (h/d) was 0.35 for both dimples. Reynolds numbers based on the channel hydraulic diameter and bulk mean velocity varied between 10,000 and 52,000. The heat transfer distributions showed that the heat transfer ratio (Nu/Nu_0) everywhere on the surfaces with dimple arrays was higher than the values in the smooth channels. The peak values of Nu/Nu_0 were more than 2.5 at the immediate downstream areas of dimples for Re=23,000. Their results also indicated that the teardrop dimples generally generated higher heat transfer.

Lin et al. [45] presented flow and heat transfer computational predictions to help explain the observed heat transfer behavior. Flow streamlines and temperature distributions were provided for the dimpled surface. The authors claimed that, as the flow entered into a dimple; two vertices took place within the dimple. Their results also showed that the heat transfer on the surfaces increased when dimples were made on two opposite walls and the two walls were push closer together.

Moon et al. [46] reported an experimental investigation, by using transient thermochromic liquid crystal technique, on the heat transfer and friction in rectangular channels with dimple matrix imprinted on one wall of each channel. The effect of

channel height on the heat transfer and friction of the dimpled walls was studied in rectangular channels with the ratio of the channel height to dimple imprint diameter (H/d) of 0.37, 0.74, 1.11 and 1.49. The ratio of depth to diameter of the dimple (h/d) was 0.193. The heat transfer enhancements of the order of 2.1 over smooth surfaces were reported with pressure drop penalties in the range of 1.6-2.0 over smooth surfaces. The authors claimed that the heat transfer ratio (Nu/Nu_0) and the friction factor in the fully developed region were invariant with Reynolds numbers for Re from 12,000 to 60,000, and no detectable effect of the channel height was found for all of the H/d cases covered. In a later study, by using the same experimental apparatus and test method, Moon et al. [47] investigated the heat transfer and friction on a smooth wall with an opposite dimpled wall installed with a clearance gap of δ/d between. The values of δ/d considered were 0, 0.024, and 0.055. The authors observed overall heat transfer enhancements of 1.4 to 3.08 on the smooth wall augmented by the dimples on the opposite wall for δ/d from 0 to 0.055 and Re from 11,500 to 35,000. As expected, the heat transfer enhancement decreased as the clearance gap increased.

. The researchers at University of Utah performed extensive studies on the flow structure and heat transfer behaviors on the dimpled surfaces (Mahmood et al. [48, 49], Ligrani et al. [41, 42] and Burgess et al. [50]). Mahmood et al. [48] made detailed flow and heat transfer measurements on a dimpled plate, and identified specific vortex structures responsible for augmenting heat transfer, especially along the downstream rim of each dimple. Heat transfer enhancements ranging from 1.8-2.4 over smooth plates were noted. Ligrani et al. [41] performed an elaborate examination on the flow structure

on a dimpled wall by employing flow visualization, pressure and velocity measurement with specially designed five-hole pressure probe, and Reynolds normal stresses measurement with hot-wire probe. The dimpled wall was machined with 13 staggered rows of dimples along the streamwise direction. Each of the dimples had a print diameter (d) of 5.08 cm, and a ratio of depth to print diameter (h/d) of 0.2. The authors identified a primary vortex pair periodically shed from the central portion of each dimple, and observed two additional secondary vortex pairs formed near the spanwise edges of each dimple. Figure 1.4 shows the sketches of three-dimensional flow structure generated by a concave dimple.

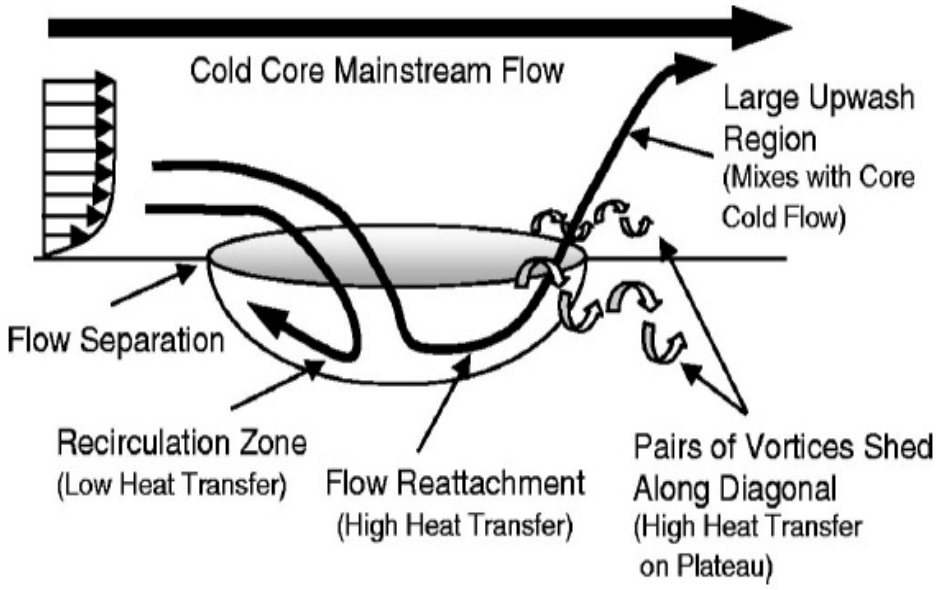

Figure 1.6: Sketches of Three-Dimensional Flow Structure Generated by a Concave Dimple (From Griffth et al. [51])

Ligrani et al. [42] then added protrusions on the wall opposite to the dimpled wall, and found the protrusions produced more vertical, secondary structure and flow mixing resulting higher heat transfer enhancement and higher pressure drop compared to the

channel with dimpled-smooth opposite walls. Mahmood et al. [49] further investigated the effects of the ratio of inlet stagnation temperature to the local wall temperature on the flow structure in a dimpled channel with four values of H/d (channel height to dimple diameter): 0.20, 0.25, 0.50 and 1.00. The authors found that the vortex pairs discussed above became stronger as H/d decreased. Burgess et al. [50] studied the effect of dimple depth on the heat transfer in a rectangular channel with aspect ratio of 8. The ratio of depth to diameter of dimple (h/d) was 0.3 with d = 5.08 cm. In the channel, one wall was machined with 29 rows of dimples, and on each row, 4 or 5 dimples were located. The temperature on the dimpled wall was recorded by thermocouples and an infrared camera. Their results showed that Nu/Nu_0 was lower in the upstream halves of dimples and higher in the downstream halves, however, the value of Nu/Nu_0 everywhere on the dimpled surface including the area inside dimples was greater than 1. The maximum Nu/Nu_0 values occurred around the downstream dimple rims. The most important finding was that the local Nu/Nu_0 and average Nu/Nu_0 were higher for h/d = 0.3 than that for h/d=0.2, while other conditions held exactly the same, indicating that the deeper dimple produced higher heat transfer.

Most recently, Griffth et al [51] studied a straight dimpled rectangular channel of aspect ratio 4:1 with rotation using thermocouple to measure the local average wall temperature, and hence average heat transfer parameters were obtained. The average Nu/Nu_0 was approximately 2.0 for stationary cases with Reynolds number from 5,000 to

40,000. The authors claimed that rotation augmented the heat transfer on both dimpled trailing and leading walls

- **Numerical Simulations**

The numerical simulations on the flow filed and heat transfer inside and around dimples are very limited. Choudhury et al. [52] performed a computation for fluid flow and heat transfer in a parallel plate channel with periodically spaced dimples. The flow is assumed to be of constant property, two-dimensional and with uniform wall temperature. Local results for the periodic fully developed velocity and temperature fields, the average heat transfer and pressure drop were presented. The authors found that decrease in the channel width and the dimple spacing was both accompanied by increase in the heat transfer and pressure drop. It must note that the flow Choudhury et al. [52] studied was laminar, which is not the practical situation in the dimpled internal cooling channel

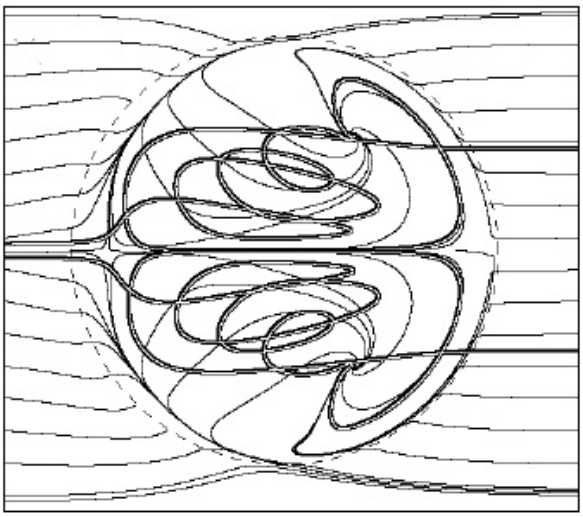

(a) Symmetric Vortex Pattern within the Dimple

Figure 1:5: Vortex Pattern and Heat Transfer Distributions along Streamwise, Main Flow Direction Is from Left to Right. (From Isaev et al. [55], Figure continued)

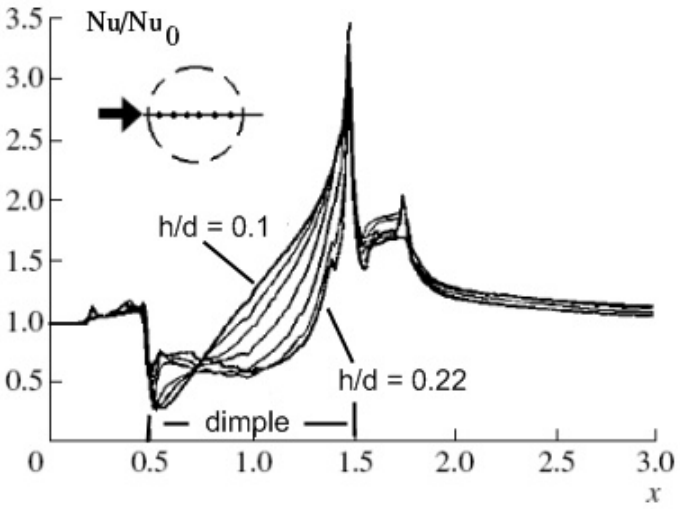

(b) Heat Transfer Distributions along the Streamwise Central Line

Isaev et al [53] then reported a simulation of flow structure on a single spherical dimple in turbulence flow. The flow was assumed to be incompressible liquid. The authors found that, in the cross-sectional view, two large-scale vortex cells were evident, and non-symmetric flow patterns were observed in the dimple, although the dimple itself and main flow were symmetric.

In 2003, Isaev et al [54, 55] presented a numerical simulation in detail of a vortex flow and heat transfer in the vicinity of a dimple in a narrow channel, where a single spherical dimple was made on one of the channel walls. The k-ω turbulence model was employed in the computation. The variation of the ratio of the depth to diameter of dimple (h/d) from 0.04 to 0.22 was examined. Special attention was given to the vortex structure induced by the dimple. Both symmetric and asymmetric vortices were observed, as seen in Figure 1.5 (a). The authors referred this kind of helical or spiral vortex as of tornado-like mechanism. The heat transfer enhancement was also provided along the

longitudinal and spanwise central lines. As shown in Figure 1.5 (b), the heat transfer ratio Nu/Nu_0 dropped below 1 on the upper half of dimple inner surface, and increased along the streamwise direction, the maximum value of Nu/Nu_0, up to 3.5, occurred on the downstream dimple rim within a very narrow band, then Nu/Nu_0 decreased sharply in the immediate wake area of the dimple rim, and reached to about 1.3 at a downstream distance of one dimple diameter. Detailed heat transfer distributions inside the dimple or on the wake area of the dimple were not available.

(d) Other internal Cooling Techniques

The other internal cooling techniques include flow impingement, pin fins [58, 59], and lattice device [56, 57], etc. Most of these methods including ribs and dimples focus on the near wall region, because the heat transfer takes place within the thermal boundary layer. Ribs, pin fins, and dimples are all designed to alter boundary layer structures close to the heated wall, so that the turbulence mixing processes near the wall are intensified, and heat transfer is enhanced. After decades of studies, the turbulence promoters on the wall have been thoroughly investigated, and the magnitude of advances appears to have stagnated.

In an internal coolant channel, there always is a cold core flow along the center line of the channel in both the stationary and rotating frames. The difference between the air temperature close to the wall and the air temperature along the center line of the passage can be in excess of 100ºK. If the cold core flow can be diverted towards the

heated walls and mixed with the hot near-wall flow, higher heat transfer coefficients could be achieved.

This idea is fundamentally different from the near-wall devices; it is designed to alter the core flow instead of tripping the boundary layer of the near-wall flow. Similar ideas are already being implemented in the heat exchanger industry. Heat exchangers with swirl flows, as shown below, can double heat transfer capabilities of traditional straight-pipe heat exchangers. Ligrani et al. [61] also discussed the use of a "Swirl Chamber" which is based on the principle of altering core flow.

Figure 1.6: Twisted metal plate used in the "Swirl-flow heat exchanger" (From Internet, author(s) unknown)

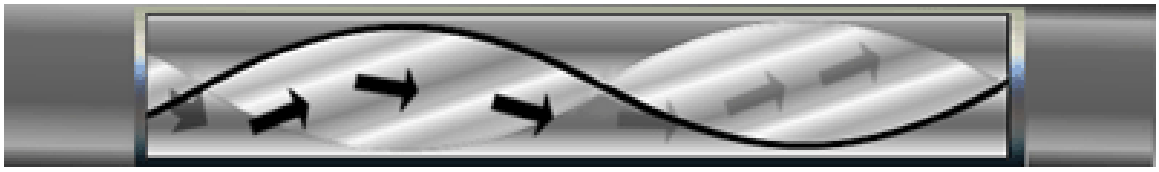

Figure 1.7: Schematic of swirl flow in a pipe (From Internet, author(s) unknown)

1.5. Objectives of the Present Study

The dissertation has two major objectives.

The configuration of the first objective in the present study is that of a rectangular coolant channel with AR = 4:1. This configuration has received limited attention, and only for restricted parameter ranges. For example, at a Re=40,000 a maximum Ro of 0.038 has been reported [13]; whereas, in modern advanced turbine systems realistic

parameter ranges include Reynolds number up to 75,000, and Ro up to 0.3-0.4. Higher parameter ranges occur in closed-loop steam cooled blades. While for the 1:1 AR geometry, Wagner et al. [4], [5] [6] and Johnson el al. [7] have reported data for Ro up to 0.48 at Re=25,000, yet no comparable data is available for the 4:1 AR coolant passages which is encountered closer to the trailing edge of the blades. The objectives of the present study are to investigate the effects of rotation, density ratios, and Reynolds number on the heat transfer and pressure drop characteristics in a two-pass 4:1 AR channel, smooth and rib-roughened with 45 deg and 90 deg ribs, over a wide range of parameter values. The parameter ranges studied include Reynolds numbers from 10,000-150,000, rotation numbers from 0 to 0.6, and density ratios from 0.1 to 0.2. The highest Ro (0.6) is achieved only at the lowest Re (10,000), at intermediate Re of 40,000 highest Ro achieved is 0.2, while at high values of Re (70,000) the maximum Ro is 0.1. No data at these high parameter values have been reported in the literature for a 4:1 AR geometry, which is the primary motivation and contribution of the present work.

The second objective is to find and test an innovative internal cooling technique by altering the main flow. The new technique should have better or equivalent heat transfer characteristics and thermal performance compared to the existing near-wall devices, so that it can be an positive optional to be used in cooling turbine blades today and in the future.

1.6. Outline of the Dissertation

The dissertation consists of eight chapters. The first chapter presents a brief

introduction of the background and literature review on internal cooling of turbine blade. The flow patterns, forces involved in the study, and the objectives of the dissertation are also described in this chapter. Chapter two describes the experimental setup for the tests with the AR 4:1 channel, the test models, and the data reduction procedures. Chapter three, Chapter four and Chapter five discuss smooth model, 90 deg model and 45 deg model, respectively. Chapter six compares the results on the three models. Chapter seven proposes an innovative internal cooling device with new finning strategies. The results obtained using liquid crystal technique are presented and discussed in this chapter. The last chapter is a brief summary on the major conclusions drawn from the experiments discussed in Chapter three through Chapter seven.

CHAPTER 2

EXPERIMENTAL SETUP AND DATA REDUCTION PROCEDURE

2.1 Experimental Setup

The rotating rig shown in the Figure 2.1(a), and originally used by Wagner et al. [4-6], has been utilized in the present study. The facility has two major components: the containment vessel and the rotating arm assembly. The containment vessel is 1.83 meters (6 feet) in diameter and consists of two symmetrical flanged sections. The upper section (not shown in Figure 2.1(a)) of the vessel is removable to allow access to the rotating arm, and the lower section is anchored and supported by a steel support frame shown in Figure 2.1(a). The vessel is designed for operation at 5 mm Hg absolute pressure to reduce the viscous heating and the power requirement of the rotating arm.

The arm assembly consists of the vertical shaft and the horizontal arm which are driven by a 15 horsepower dc motor. The rotational speed of the shaft can be varied from 0 to a maximum tested speed of 1500 rpm by a feedback electronic controller. The vertical shaft consists of the main outer shaft and an inner concentric shaft. Together the shafts provide dual fluid paths for the rotary unions mounted on each end of the main shaft. In the present experiments, only the inner shaft is used as the air path. On the exterior surface of the main shaft, recessed grooves allow signal and power leads to run from the rotating arm assembly to two slip rings, one located on the upper end of the main shaft (not shown in the Figure) and the other on the lower end. The two slip rings

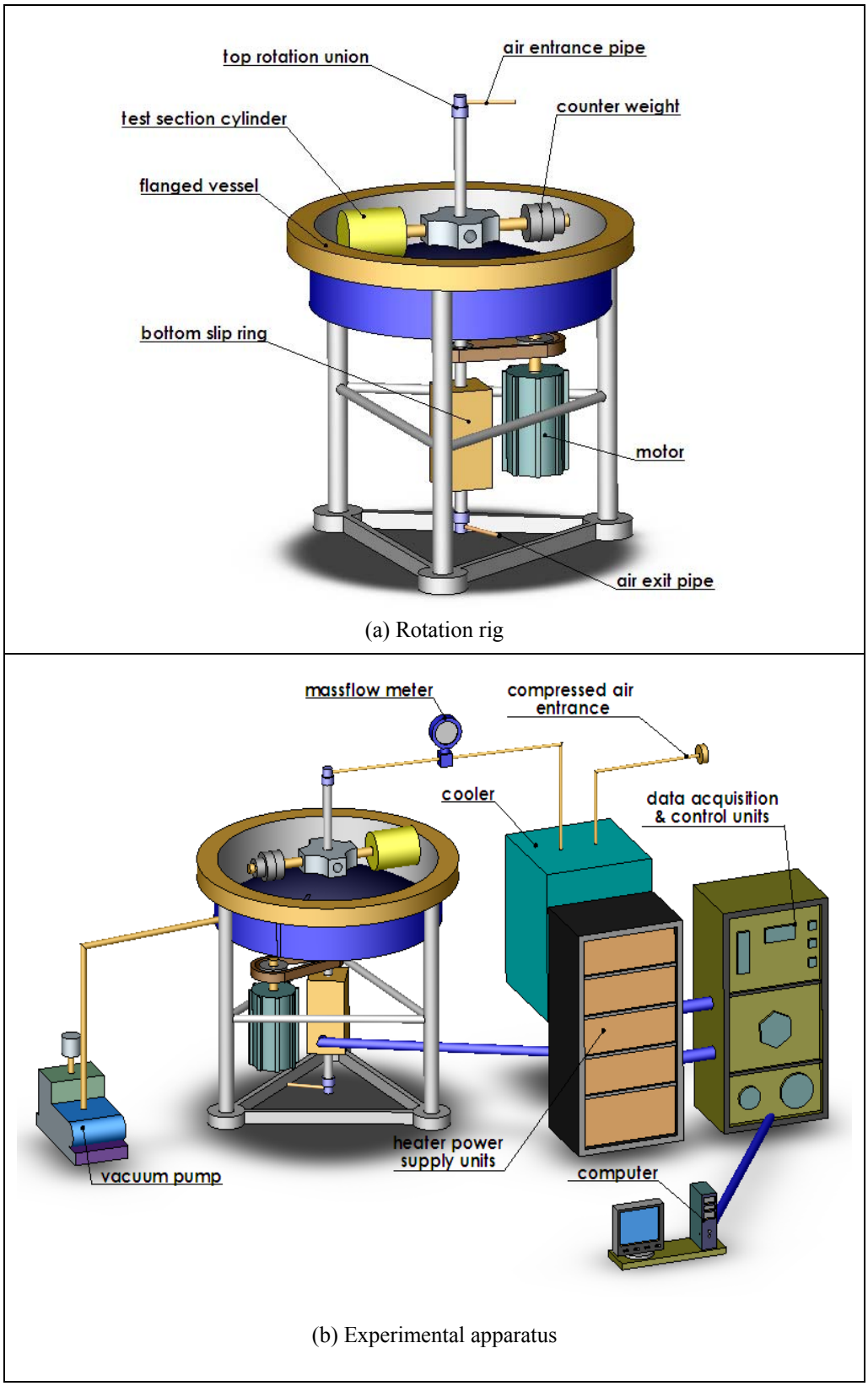

(a) Rotation rig

(b) Experimental apparatus

Figure 2.1: Experimental Setup

provide a total of 240 channels for power and instrumentation wires between the stationary and rotating frames.

A cylindrical pressure vessel containing the test section is mounted on one end to the horizontal arm. On the other end, a counter weight, with variable mass and positioning capabilities, is mounted to allow for static and dynamic balancing of different test sections. Stainless steel tubing along the arm provides an air passage from the test section to the shaft. A ScaniValve pressure transducer assembly is mounted on the arm to measure the absolute pressure and differential pressure inside the test section.

Air entering the test section is circulated through a refrigerant cooling loop to alter and maintain the temperature of the inlet airflow in order to achieve the desired density ratio (Figure 2.1(b)). The air is provided by a compressor-dryer-reservoir system, with a maximum mass flow rate and pressure of 0.5 kg/s and 20 atm (300 psia), respectively. The power supply unit has 72 independent channels for providing the 0-45 volts of dc power for the heaters inside the test section. The data is acquired through a Hewlett-Packard data acquisition systems (HP 3497a and HP 3498a extender), which are connected to a Dell computer through a GPIB port and controlled by a custom-written C program. The pressure signals, shaft speed, thermocouple readings, and heater power readings are all recorded by this system. The mass flow rate of the airflow is read separately through a Rosemount mass flow unit.

2.2 Heat Transfer Models

Figure 2.2 shows a section view of the lower portion of the smooth model. The 45-deg and 90-deg ribbed models have the same geometry as shown in Figure 2.2, the only difference is the copper elements (shown in Figure 2.3). The lower portion consists

of a 6.35 mm (0.25 inch) thick G-10 Garolite (continuous-woven laminated glass fabric with thermal conductivity of 0.1 W/(m-K)) bottom plate, a 0.794 mm (0.031 inch) thick silicon rubber sheet between the bottom plate and the frame, a 12.7 mm (0.5 inch) thick G-10 Garolite central and outer frames, and eleven copper elements (10 rectangular plates plus a bend) that are 3.175 mm (0.125 inch) thick. The copper elements rest on shoulders on both the central and outer frames, and are flush with the bottom surface of the frames. The copper elements on the upper portion (not shown in Figure 2.2) are flush with the top of the frame. Together they form a U-shaped channel with a cross-section having dimensions of 25.4 mm (1 inch) wide by 6.35 mm (0.25 inch) tall (aspect ratio of 4:1 and hydraulic diameter of 10.16 mm (0.4 inch)). An additionol silicon rubber sheet and a G-10 Garolite top plate, identical to the bottom one, rests on the top of the frames, and finally the whole unit is held together by screws through the smaller holes in the frames.

The straight inlet and outlet sections of the test channel are 117.475 mm (4.625 inch) long, and the outer diameter of the bend is 69.85 mm (2.75 inch). The smooth inner and outer sidewalls, which are not heated during the tests, are formed by the G-10 frame surfaces. In the inlet channel, two pressure taps are installed to measure the inlet static pressure and the pressure drop across the length of the first straight leg of the channel. A steel two-channel transition section is inserted between the top and bottom G-10 plates and aligned with the inlet and exit planes of the test section. This section provides the transition between the test channel and the air-feeds on the rotation rig. The transition section is also equipped with screens to stabilize the flow, and two K-type thermocouples to measure the inlet and outlet flow temperatures. The whole unit is bolted between two

steel support plates, and the assembly is mounted inside a cylindrical pressure vessel. The thermocouple leads, power wires, and the pressure transducer tubes are routed out of the vessel through sealed plugs on one of the cylinder's planar faces.

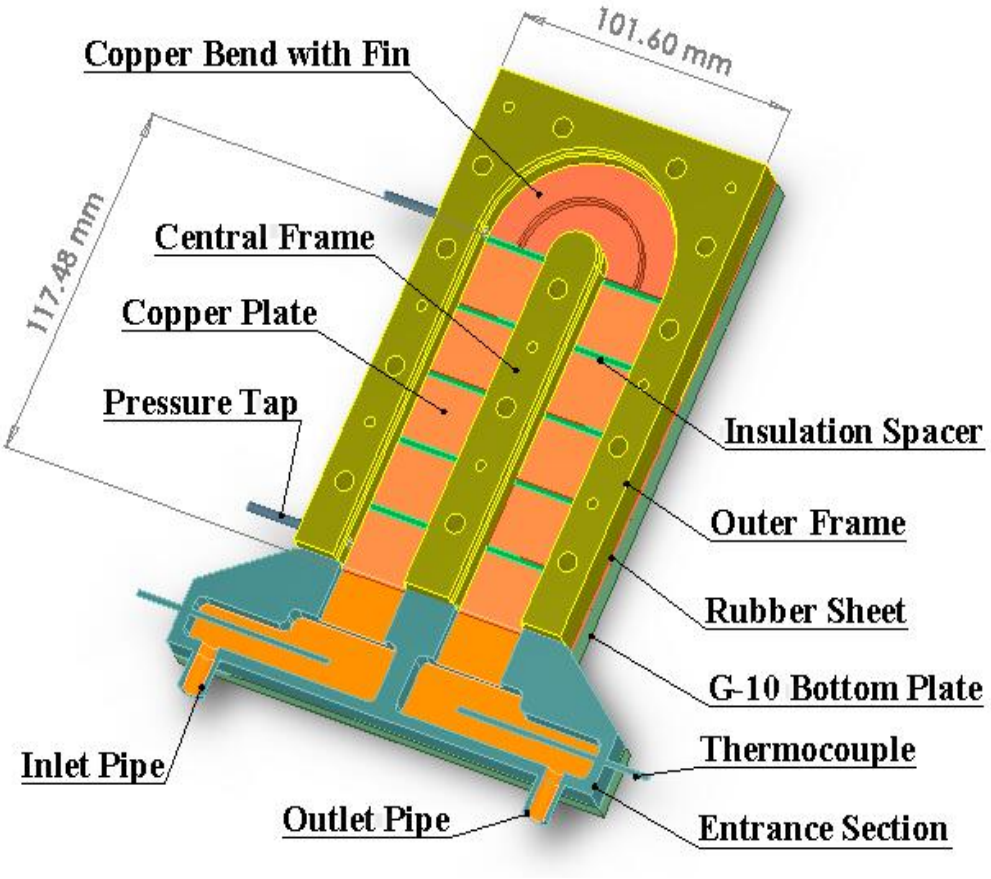

Figure 2.2: Heat transfer model

The typical copper element configurations with smooth surface, 90 deg ribs and 45 deg ribs are shown in Figure 2.3. Each copper plate has the dimensions of 27.432 mm (1.08 inch) by 21.59 mm (0.85 inch) by 3.175 mm (0.125 inch). On the back of each copper plate, a Minco Kapton Aluminium-backed foil heater is installed using thermally

conductive adhesive film. Two K-type thermocouples are installed into two blind holes inside each copper plate using thermally conductive glue. Each copper plate is isolated by a G-10 Garolite spacer with dimensions of 1.905 mm (0.075 inch) by 27.432 mm (1.08 inch) by 3.175 mm (0.125 inch) to impede heat conduction between different copper plates. The inner surfaces of the spacers are carefully flush mounted with the surfaces of the copper elements in the channel. A total of twenty copper plates separated by spacers collectively form the top and bottom of inlet and outlet straight channels.

The ribs for 45 deg model are machined directly on the element surface. However, the ribs for 90 deg model are cut from straight silver bars with a square cross section of height e = 1.02 mm (0.04 inch). Both ends of each rib are inserted into the open slots on the bottom surfaces of the side and central frames, then the ribs are squeezed between the copper plates and the side/central frames, so that the ribs cannot move along any direction. A very thin layer of thermal conductive epoxy is applied between each silver rib and the corresponding copper plate to improve thermal conductivity.

The rib pitch p = 10.16 mm (0.4 inch), resulting in a $e/D_h = 0.1$ and $P/e = 10$. The upper and lower ribs are parallel and staggered. In addition, a continuous copper element is used to form each bend. Each bend plate (top and bottom) is equipped with a foil heater with the same surface area as the bend and two K-type thermocouples.

2.3 Data Reduction

During each experimental run, the wall temperature, T_w of each copper plate is maintained at a constant value. In order to achieve the uniform wall condition, the current to each individual heater is adjusted. By varying T_w and inlet flow temperature,

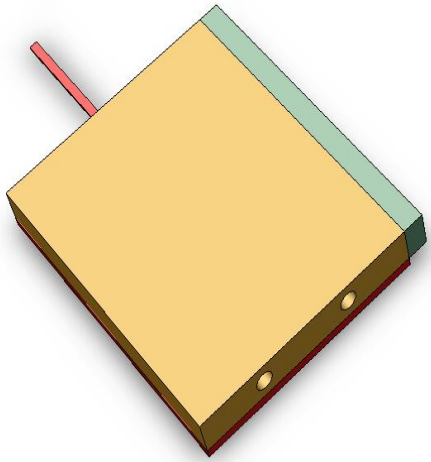

(a) Smooth

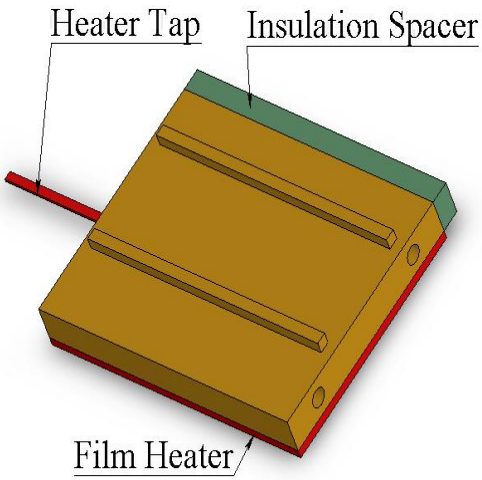

(b) 45-deg Ribbed

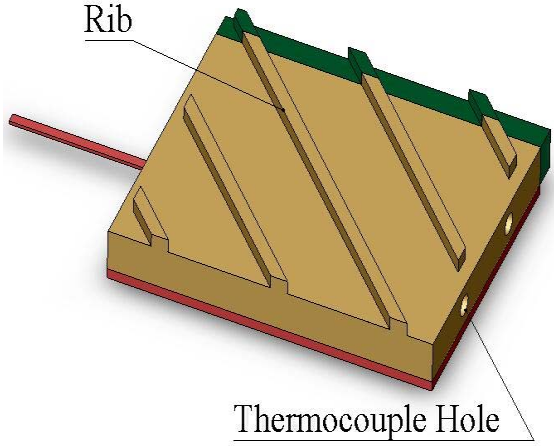

(c) 90-deg Ribbed

Figure 2.3: Copper elements

T_{in}, different density ratios are obtained. The local heat transfer coefficient h_i at the i-th copper plate is calculated from the net heat flux, $q''_{net,i}$, from the heated plate to the cooling air, the surface temperature of the plate, T_w, and the local bulk mean air temperature, $T_{b,i}$ at the mid-point of the plate, as follows:

$$h_i = q''_{net,i} \Big/ (T_w - T_{b,i}) \quad \text{where} \quad q''_{net,i} = (q_i - q_{loss,i}) \Big/ A_i \ \text{ and } \ q_i = I_i^{\,2} \cdot R_i \qquad (1)$$

In the above equation, I_i and R_i are the current and the resistance of the i-th copper plate, respectively, $q'_{loss,i}$ is the heat loss from the i-th plate, and A_i is the projected area of the copper plate. The maximum temperature reached by the plates over the range of test conditions is 386 ^{0}K, and the resistance of the heaters are constant in this temperature range as per data sheets provided by Minco inc.

The heat loss for each copper plate is determined by a series of stationary tests, without flow, where under equilibrium conditions, the heat input is balanced by the heat loss, and the heat loss can be calibrated to the wall temperature. The total heat loss is double checked by an energy balance. It is found that the total heat losses calculated by energy balance and the stationary heat loss tests are very close to each other. For example, at Re=25,000 and DR=0.15, the ratio of the total heat loss to the total heat power is about 7%, and the ratio of the maximum difference of the total heat losses calculated by the two methods to the total heat power is only 1.15%.

The local bulk mean air temperature, $T_{b,i}$, is given by:

$$T_{b,i} = T_{in} + \left(\sum_{j=1}^{i-1} (q_j - q_{loss,j})_{leading} + \frac{1}{2}(q_i - q_{loss,i})_{leading} \right) \Big/ (\dot{m} \cdot C_p)$$

$$+\left(\sum_{j=1}^{i-1}\left(q_j - q_{loss,j}\right)_{trailing} + \frac{1}{2}\left(q_i - q_{loss,i}\right)_{trailing}\right) \Big/ \left(\dot{m} \cdot C_p\right) \qquad (2)$$

where $\dot{m}$ is the mass-flow rate, and c_p is the specific heat. The Nusselt number, Nu_i, is then obtained from

$$Nu_i = h_i \cdot D_h / k \qquad (3)$$

where d_h is the hydraulic diameter of the test channel (0.4 inches), and k is the air conductivity. Then Nu_i is normalized by the Dittus-Boelter correlation:

$$Nu_{ref} = 0.023 \cdot Re^{0.8} \cdot Pr^{0.4}.$$

Thus,

$$Nu_i / Nu_{ref} = h_i \cdot D_h / \left(k \cdot 0.023 \cdot Re^{0.8} \cdot Pr^{0.4}\right) \quad (4)$$

For convenience of direct comparison with the square channel, Nu is normalized by Nu_0, where Nu_0 is the Nusselt number in the fully developed region in the corresponding smooth channel with the same aspect ratio AR at Ro=0. The frictional factor, f, is calculated by:

$$f = \left(\Delta P \cdot D_h\right) / \left(4L \cdot \tfrac{1}{2} \cdot \rho \cdot V^2\right) \qquad (5)$$

where L is the distance between the two pressure taps, Δp is the pressure drop, ρ is the flow density, and V is the mean velocity of the flow. Then f is normalized by the Karman-Nikuradse equation [15], $f_0 = 0.046 \cdot Re^{-0.2}$:

$$f / f_0 = \left(\Delta P \cdot D_h\right) / \left(4L \cdot \tfrac{1}{2} \cdot \rho \cdot V^2 \cdot 0.046\, Re^{-0.2}\right) \quad (6)$$

and the thermal performance factor is:

$$TPF = (Nu/Nu_{ref}) / (f/f_0)^{1/3} \qquad (7)$$

2.4 Uncertainty

Using the method of Kline and Mcclintock [16] method, the maximum relative uncertainty in the calculated heat transfer coefficient is estimated to be approximately 7% in the inlet and 15% in the outlet for current test conditions based on the maximum potential error of thermocouple readings of 0.5^{o}C.

CHAPTER 3

SMOOTH PASSAGES

During the experiments, the pressure in the test section was maintained at 1034 kPa (150 psia). The inlet air temperature varied from 25 ^{o}C (stationary) to 35 ^{o}C (at high rotational speeds), while the wall temperature was varied between 58 ^{o}C to 112 ^{o}C to achieve different density ratios. As noted earlier, the experimental test matrix covered Reynolds number, Re, from 10,000 to 150,000, Rotation number, Ro, from 0 to 0.6, and density ratio, DR, from 0.1 to 0.2.

3.1 Stationary Tests

A series of stationary tests were initially performed in order to validate the experimental procedures and to serve as a basis for comparison. For each Re number, the stationary tests were repeated three to six times. The repetition showed that the results for a given Re number were very consistent. Typically, the variations in results were no more than 2% in the fully developed region.

Figure 3.1 shows the streamwise Nu/Nu_0 distributions in the two-pass channel for Re = 10,000 and 40,000. Stationary results are identified as Ro=0. The bend is located between $10.5 < X/D_h < 14.5$. The inlet channel (radially-outward flow) is upstream of the bend ($X/D_h < 10.5$), and the outlet channel (radially-inward flow) is downstream of the bend ($X/D_h > 14.5$).

The results show almost no Reynolds number effects in the fully developed regions of the inlet or outlet channel, and the heat transfer ratio, Nu/Nu_0, is approximately

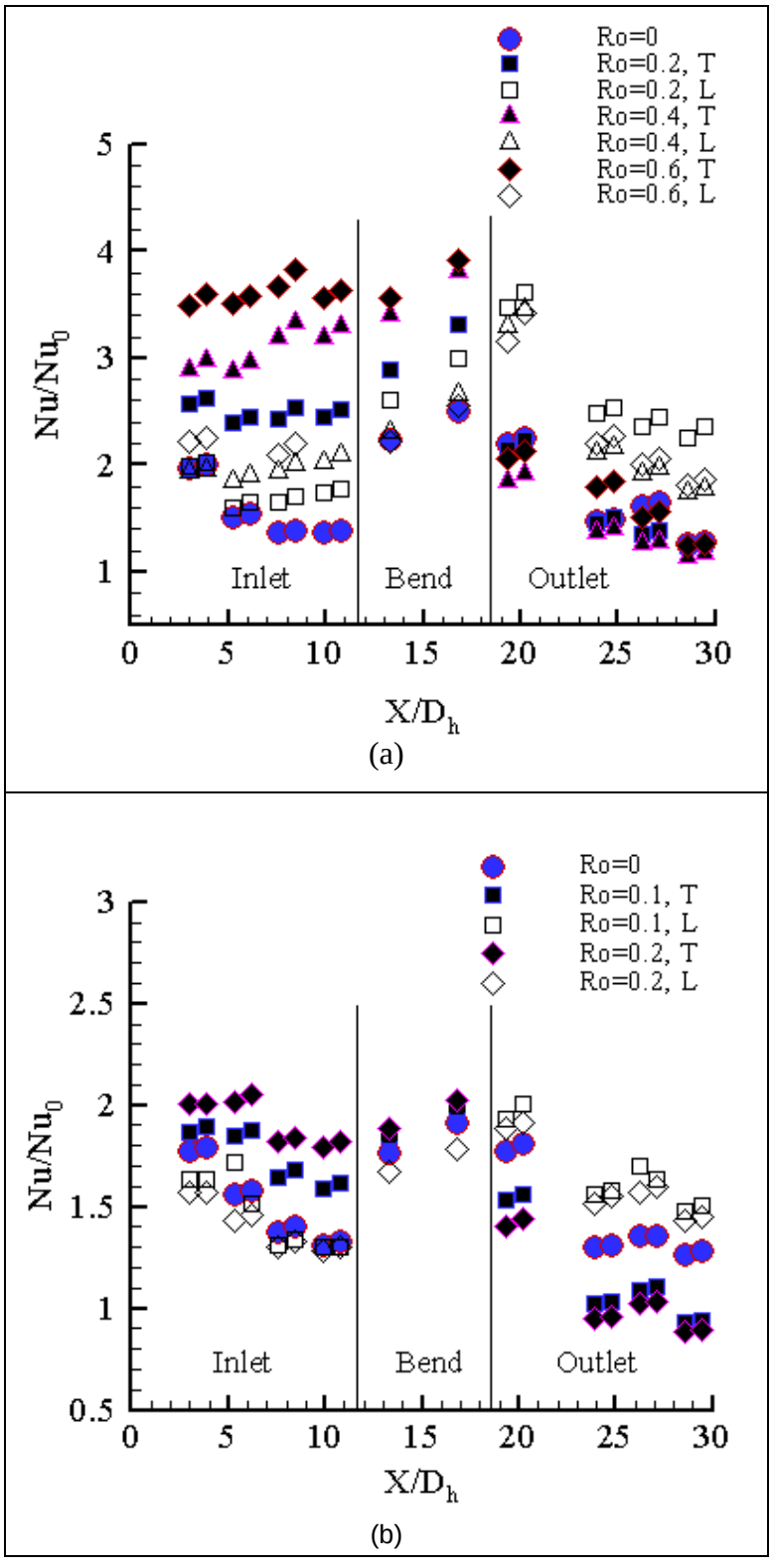

Figure 3.1: Rotation effects in the two-pass channel for DR=0.1 at (a) Re=10,000 and (b) Re=40,000

1.25-1.3 in the fully developed regions. The 25% enhancement of Nu/Nu_0 with respect to the smooth circular tube value is due to the 4:1 aspect ratio of the coolant passage, and probably due to the two unheated sidewalls. The bend has the highest N_u/N_{u0} (1.8 to 2.0) due to the secondary flows and turbulence induced in the 180^o bend. The two copper elements immediately downstream of the bend also have a higher N_u/N_{u0} due to the bend-induced secondary flows. Close to the entrance of the inlet channel, due to the thermal development of the boundary layers, higher heat transfer ratios (1.8 to 2.0) are observed.

3.2 Rotation Effects

Rotation effects for square (AR of 1:1) cross-section passages have been well documented in the literature. Coriolis-driven secondary flows, in the form of a two-roll eddy, are directed from the middle of the leading surface to the trailing surface in the inlet duct while the flow direction is reversed in the outlet duct. Based on this understanding of the secondary flow motion, heat transfer is expected to be enhanced on the inlet-trailing and outlet-leading walls (called destabilized surfaces), while they are expected to be reduced along the stabilized inlet-leading and outlet-trailing surfaces. Recent numerical calculations in 4:1 AR passages have however shown that the flow field has a complex multi-cellular flow pattern, and that both the trailing and leading surfaces experience a downwash of the core fluid [13].

Figure 3.1 shows the streamwise Nu/Nu_0 distribution at Re=10,000 for Ro up to 0.6, and at Re=40,000 for Ro values up to 0.2. At the lower Re, the stabilized surfaces do not exhibit any significant degradation in heat transfer with rotation; rather, in the inlet duct, all surfaces experience an increase in heat transfer with Ro. Such a behavior is consistent with the experimental results in [13] and the numerical study in [35]. In [35] it

was shown that a multi-cellular flow pattern exists in the coolant passage, and that even the leading surface experiences a downwash over certain regions of the surface leading to enhanced heat transfer on the surface. However, the enhancements along the trailing surface are higher than the leading surface in the inlet channel. At a Ro=0.6, Nu/Nu_0 reaches values of 3.6 on the trailing surface of the inlet duct, and 4 in the bend regions, while the corresponding enhancement along the leading surface in the inlet duct is in the range of 2.2-2.4. In the outlet duct, similar trends are observed with three notable exceptions. First, the enhancement levels are lower with a maximum Nu/Nu_0 value of about 2.4 along the leading surface. Second, along the trailing surface no enhancement is observed in the fully developed region, and the Nu/Nu_0 values remain relatively unchanged. Third, the leading surface enhancement does not exhibit a monotonic dependence with Ro; rather the maximum Nu/Nu_0 value is attained at Ro=0.2, beyond which the Nu/Nu_0 values decrease with Ro. This non-monotonic behavior will be discussed further later. The lower enhancements obtained in the outlet duct are linked to the bend-induced flows that delay or mitigate the establishment of the Coriolis-induced secondary flows.

At Re=40,000 and at higher Re, the Nusselt number distributions and their dependence on Ro, is different than that described above for lower Re, and conforms more to the expected trends of enhancement along the destabilized surface and degradation along the stabilized surface. In the inlet region, the degradation levels are however rather low. For example at $X/D_h = 8.0$ (the fully developed region in the inlet) and at Ro = 0.2, the Nu/Nu_0 on the trailing wall increases to 1.8 from the stationary passage value of 1.25, while the corresponding decrease in Nu/Nu_0 on the leading wall is

negligible. In the bend region, the effect of rotation is similar to that in the inlet although degradation effects are more significant. In the outlet, the Nu/Nu_0 on the leading wall increases with Ro, and correspondingly decreases on the trailing wall; however, the degradation effect on the stabilized trailing wall is more pronounced in the outlet channel compared to that observed on the stabilized wall in the inlet channel.

The rotation effects can be seen more clearly in Figure 3.2 (for destabilized surfaces, i.e, inlet-trailing and outlet leading) and Figure 3.3 (for stabilized surfaces, i.e., inlet-leading and outlet-trailing) which focus attention on a fixed X/D_h location in the fully developed inlet and outlet regions. For each surface, the figures are plotted separately for the lower Re ($\leq 40{,}000$) and higher Re ($\geq 70{,}000$) ranges for clarity.

Figure 3.2 shows the Nu/Nu_0 values along the destabilized surfaces where an increase with Ro is expected. Along the outlet-leading surface (Figure 3.2(c), 3.2(d)), an increase in Nu/Nu_0 is observed with Ro until a critical Ro is reached beyond which Nu/Nu_0 decreases or plateaus. This non-monotonic behavior was earlier noted in Figure 3.1. The AR 1:1 data reported by Wagner et al. [5] at Re=25,000 is also shown in Figure 3.2(c), and also displays a similar behavior with an increase in the Nu ratio up to a Ro of about 0.1. The critical Ro appears to be lower for higher Re, and is 0.25 for Re=10,000 and 0.05 for Re=100,000. Along the inlet-trailing surface (Figure 4(a), 4(b)), evidence of a similar behavior can also be seen, except that, the critical Ro is considerably higher. For Re=10,000, 20,000, and 40,000 this critical Ro does not appear to be reached in our measurements, but at Re=70,000 and 100,000 a plateau in the profile develops around Ro=0.05. At Re=150,000, the plateau in the profile is essentially observed at all Ro, with little or no change in the Nu ratio with Ro. The 1:1 AR data [5] at Re=25,000 shows a

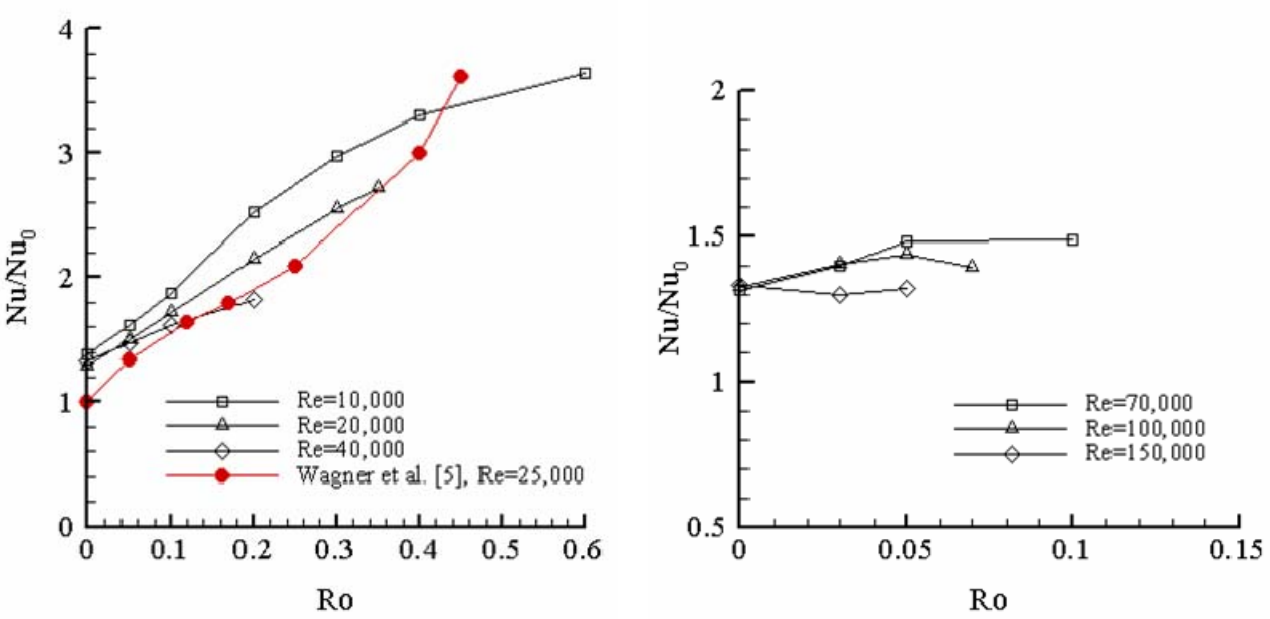

(a) Inlet-trailing wall (b) Inlet-trailing wall

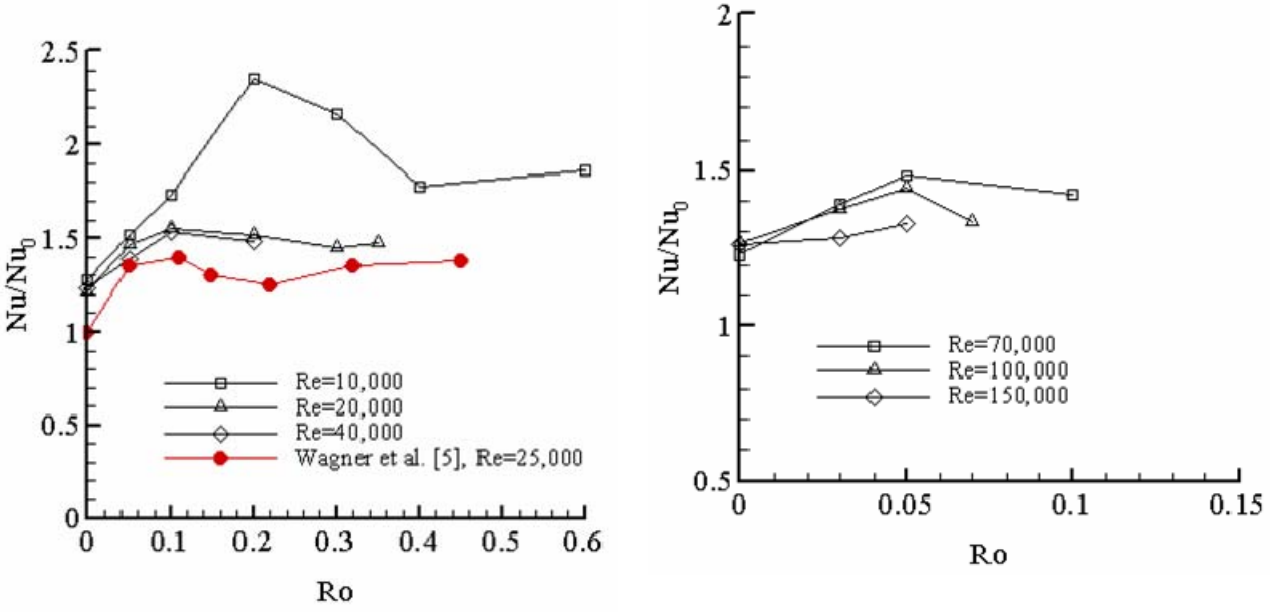

(c) Outlet-leading wall (d) Outlet-leading wall

Figure 3.2: Rotation effects on destabilized surfaces at DR=0.1. (a)-(b) inlet-trailing wall at X/D_h =8.0; (c)-(d) outlet-leading wall at X/D_h =26.7.

monotonic increase with Ro along the inlet-trailing wall. For Ro<0.3, the Nu ratio for the 1:1 AR is less than the Nu ratio for the 4:1 AR (at Re=20,000), as expected based on previously reported measurements [13] and computations [35]. However, at higher Ro it appears that the 1:1 AR values of the Nu ratio exceed those of the 4:1 AR implying a greater rotational effect for the 1:1 AR case.

For the stabilized surface (Figure 3.3), the inlet-leading wall shows enhancement with Ro at low Re ($\leq$20,000), consistent with the experimental observation in [13], while the outlet-trailing wall shows reduction in Nu/Nu_0 until a critical Ro, beyond which, Nu/Nu_0 increases again. The increase in Nu/Nu_0 along the stabilized surface is linked to the multi-cellular flow patterns obtained in rotating 4:1 AR ducts [35] which produce a downwash of core fluid even along the stabilized surface. However, this effect is limited to low Re, since as observed in Figure 3.3, for Re$\geq$70,000, Nu/Nu_0 along the stabilized surfaces decrease with Ro, in contrast to the low Re experimental observations in [13]. This strong Re-dependence of the effect of rotation on the Nu/Nu_0 ratio has not been previously reported, and should clearly be taken into consideration by the turbine heat-transfer designer.

Along the inlet-leading stabilized surface, the present data for 4:1 AR shows enhancement with Ro at low Re, while the 1:1 AR data shows degradation till Ro=0.25 (Figure 3.3 (a)). This difference in behavior in the present data, with enhancement along the stabilized surface at low Re, was explained earlier, and attributed to strong multi-cellular secondary flow patterns that enhance the heat transfer on the inlet-leading surface. In 1:1 AR data, enhancement along the stabilized surface is also observed but only at high Ro (Ro$\geq$0.25). Saha and Acharya [35] also reported enhancements of the

inlet-leading wall heat transfer for 1:1 AR at $Ro \geq 0.25$, and linked these to the development of large-wavelength unsteadiness in the flow, and the development of two additional counter-rotating vortex pairs which increased the recirculation. Iacovides et al. [10] have also performed a numerical study, and noted the important role of Ro. Their results show that at lower Ro numbers, Coriolis forces produce a single vortex-pair. As Ro increases the vortex-pair becomes unstable and breaks into two pairs of vortices. This change in flow pattern was seen to alter the heat transfer characteristics.

Figure 3.4 presents the averaged Nu/Nu_0 value in the bend region as a function of the rotation number. Data is presented for the leading and trailing surfaces of the bend, and the low and high-Re plots are separated out for clarity. Rotation number effects in the bend are significant only at the lower Re (10,000 and 20,000), and behave as in the inlet (radially-outward flow) channel. Thus the trailing surfaces see significant enhancement (Nu/Nu_0=3.8 at Ro=0.6, Re=10,000), while the leading surfaces see moderate enhancements up to a Ro of about 0.2 (Nu/Nu_0=2.8 at Re=10,000) beyond which there is a small decrease in the Nu/Nu_0 value. At higher Re values ($\geq$40,000), Nu/Nu_0 values along the trailing and leading surfaces are in the range of 1.8-2, and it would appear that at these higher-Re, the bend-induced secondary flows begin to play a more important role, and the primary Coriolis forces that arise from the radial velocity diminish. Note that as the flow turns in the bend, the mean radial velocities (and the primary Coriolis-force component) decrease and reach zero at the 90^0 turn point, and then increase again as the flow turns radially inwards in the outlet.

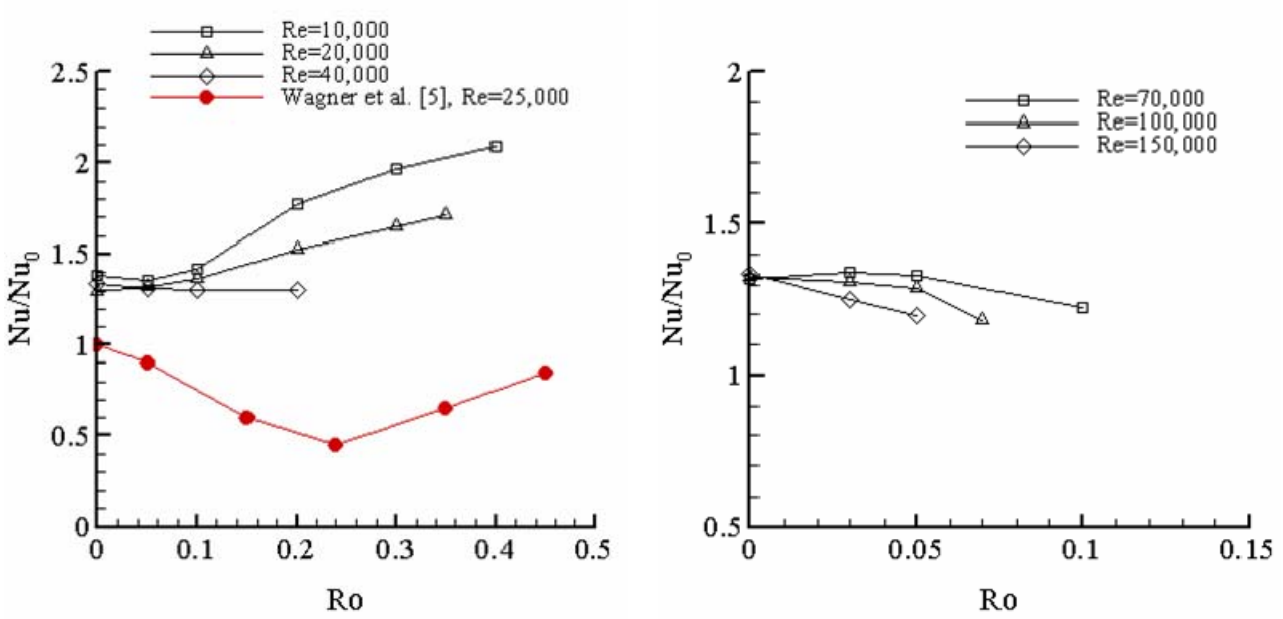

(a) Inlet-leading wall (b) Inlet-leading wall

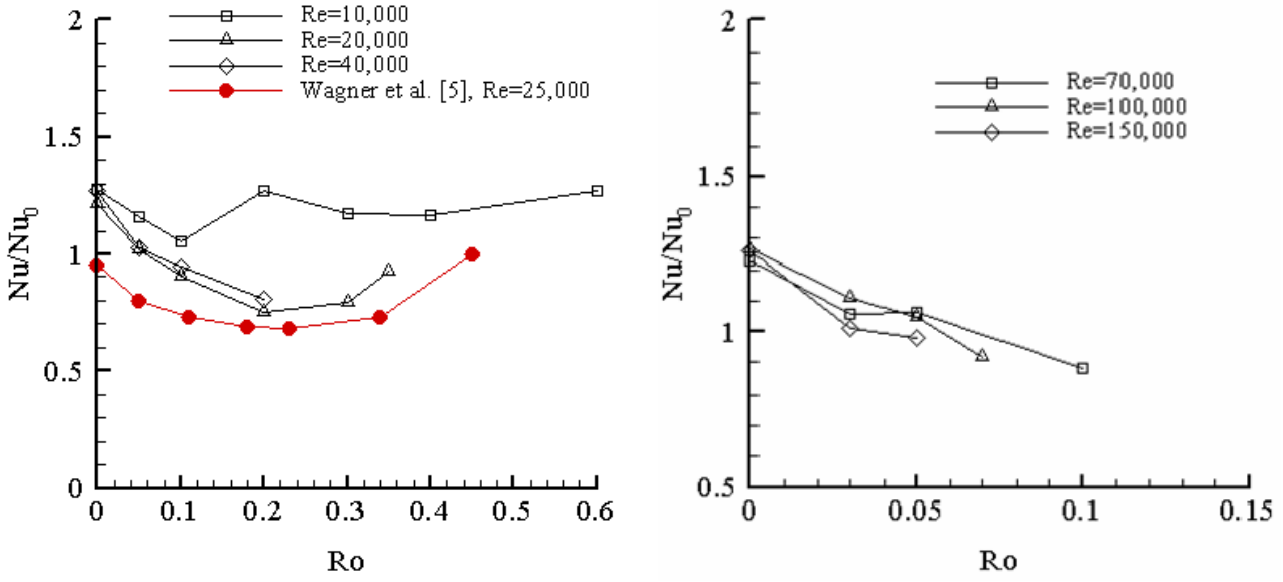

(c) Outlet-trailing wall (d) Outlet-trailing wall

Figure 3.3: Rotation effects on stabilized surfaces at DR=0.1. (a)-(b) inlet-leading wall at X/D_h =8.0; (c)-(d) outlet-trailing wall at X/D_h =26.7.

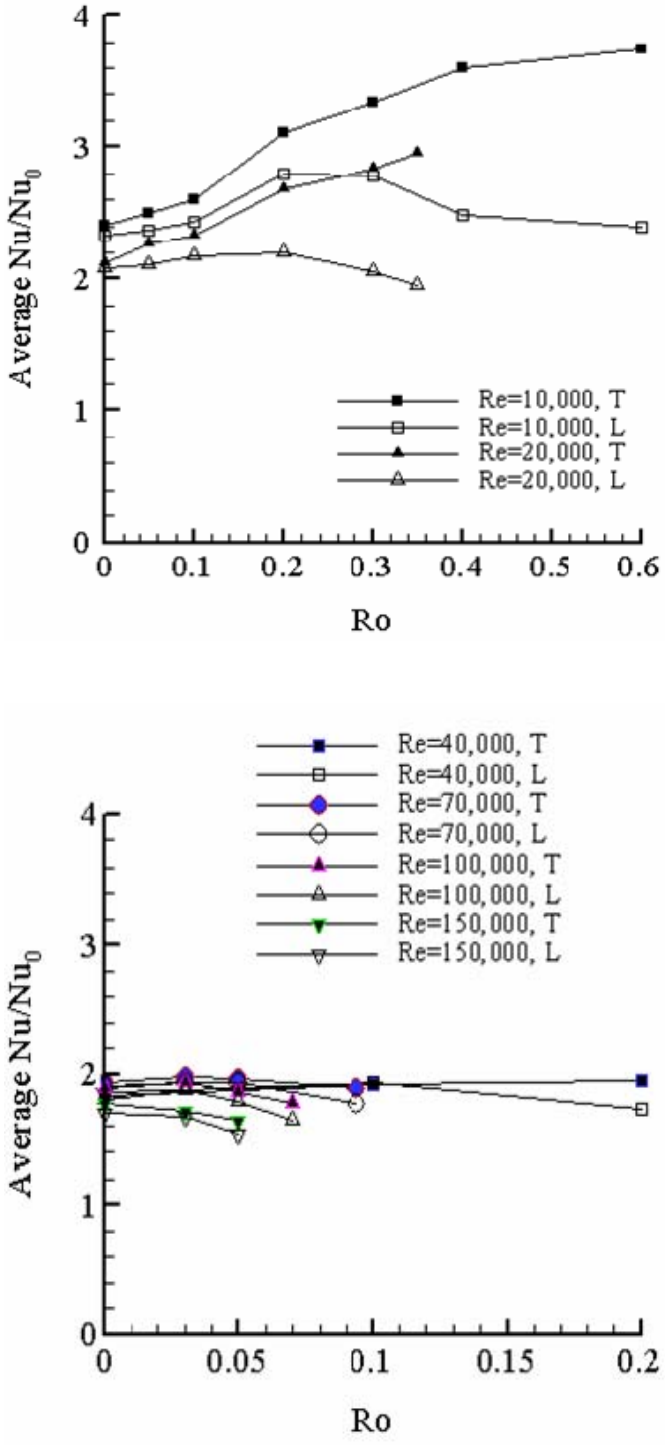

Figure 3.4: Rotational effects on the heat transfer in the bend at DR=0.1

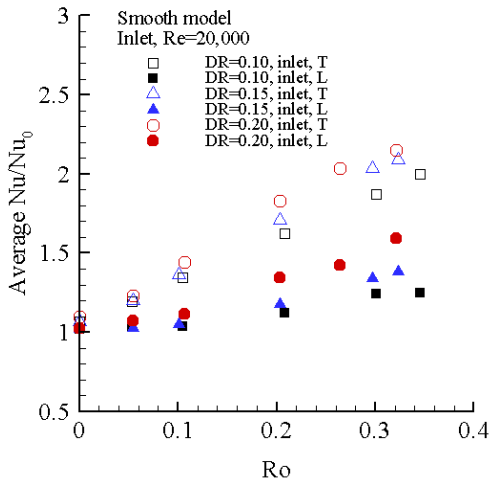

(a) Inlet

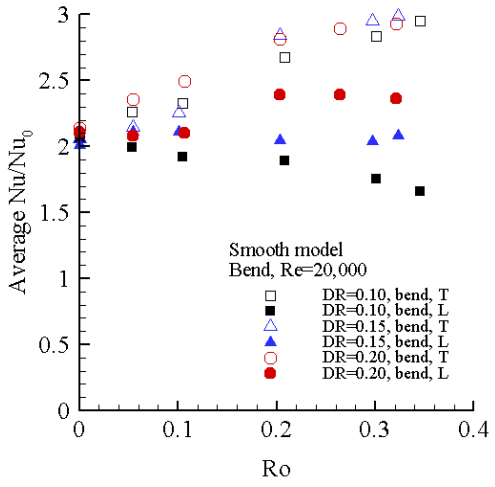

(b) Bend

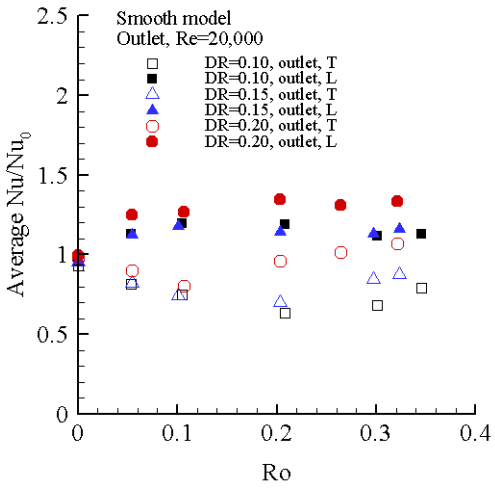

(c) Outlet

Figure 3.5: Density ratio effects at Re=20,000 (a) inlet; (b) bend (c) outlet

3.3 Density Ratio Effects

To investigate the effects of buoyancy on the Nu/Nu_0, a series of test were conducted varying the density ratio, DR, where DR is defined by $DR = (T_w - T_{in}) / T_w$. The wall temperature, T_w, of the copper plates was adjusted for a specific measured inlet air temperature, T_{in}, to achieve different density ratios DR at Re=10,000 and 20,000. The buoyancy parameter is proportional to both DR and Ro, and therefore higher DR or higher Ro imply higher buoyancy parameter values.

Figure 3.5 shows the average Nu/Nu_0 distribution at Re=20,000 for three different values of DR. As the DR increases, centrifugal-buoyancy forces are larger. In the inlet duct, the centrifugal-buoyancy opposes the radially-outward flow, while in the outlet duct, the centrifugal-buoyancy force aids the radially-inward flow. However, as seen from Figure 3.5, increasing DR enhances Nu/Nu_0 in both the inlet and outlet ducts. Centrifugal-buoyancy produces opposed/aiding flow effects in the inlet/outlet channel, and also influences turbulence through counter-shear enhancement (in opposed flow situations) or through boundary-layer modifications. Therefore, either through turbulence enhancement (inlet channel) or boundary layer thinning with aided flow (outlet channel) there is an increase in Nu/Nu_0 with DR.

As seen in Figure 3.5, DR does not alter any of the trends observed earlier in Figures 3.2 and 3.3; rather, with increasing DR, Nu/Nu_0 values are enhanced and the trends accentuated. For example, along the inlet-leading surface, the enhancement observed earlier in Figure 3.3 is increased further at the higher DR. Along the outlet duct, a critical Ro had been observed for DR=0.1 where the enhancement along the destabilized surface and the degradation along the stabilized surface was either reversed

or arrested (Figure 3.3). At a higher DR of 0.2, the critical Ro, where the change in trend takes place, is lower.

DR effects in the bend region are shown in Figure 3.5(b), which indicates that DR has a considerable effect on the leading surface of the bend. At a Ro=0.3, the leading-bend surface Nu/Nu_0 increases by nearly 40% when the density ratio increases from 0.1 to 0.2. The effect of DR on the trailing-bend surface is however considerably lower.

The centrifugal-buoyancy effects are often presented by plotting Nu/Nu_0 as a function of the buoyancy parameter, Bo ($=DR*Ro^2*R/D_h$). This parameter is equivalent to the ratio of Grashof number to the square of Re number used in the stationary mixed convectional heat transfer to evaluate the relative importance of inertial and buoyancy force. However, in the present case, the buoyancy is caused by rotational gravitation rather than the earth gravity. Apparently, buoyancy parameter Bo is affected by density ratio DR and rotation number Ro. The centrifugal-buoyancy effects at Re=20,000 are shown in Figure 3.6 for both the inlet and outlet channels. Figure 3.6 has the same data sets as in Figure 3.5(a) and 3.5(c).

In general, the data at different DR collapses quite well. In the inlet channel, the average Nu/Nu_0 along the leading and trailing walls increases monotonically, and becomes asymptotic with Bo on both walls. These are similar to the results of Wagner et al. [5] on the trailing wall in a square channel at Re=25,000, but are different on the leading wall, where Wagner et al. [5] observed decreasing in Nu/Nu_0 with Bo increasing when Bo was less than 0.2.

The author speculates that the difference is caused by two facts. First, the effects of Coriolis force and buoyancy force are coupled. Second, Coriolis force is stronger in

the square channel than in the AR 4:1 rectangular channel. In the inlet channel with radically outward flow, rotational buoyancy force aids the heat transfer on both leading and trailing walls, while Coriolis force enhances heat transfer on the trailing wall, but degrades the heat transfer on the leading wall. On the inlet trailing walls of square and AR 4:1 rectangular channels, heat transfer is enhanced by both rotational buoyancy force and Coriolis force, so Nu/Nu_0 on the inlet-trailing walls increases monotonically with Bo. However, on the inlet leading walls Coriolis force weakens the heat transfer, while rotational buoyancy force still facilitates the heat transfer. On the leading wall of square channel, the Coriolis effect is stronger and it takes on the rotational buoyancy effect at low Ro. So Nu/Nu_0 decreases as Bo increases, when Bo is less than 0.2. But as Bo reaches to 0.2, the rotational buoyancy effect becomes significant, and finally takes on the Coriolis effect. Thus, beyond this point, the heat transfer is enhanced on the inlet-leading wall, and Nu/Nu_0 begins to rise with Bo. On the wall of AR 4:1 channel, the Coriolis effect is weaker and it is taken on by the rotational buoyancy effect even at small Bo values, so the heat transfer is enhanced on the inlet-leading wall in the AR 4:1 channel by the coupled effects of Coriolis and rotational buoyancy force, and monotonic increase of Nu/Nu_0 with Bo is observed.

In the outlet channel, the interaction of Coriolis force and rotational buoyancy force is more complicated. The heat transfer on the outlet-leading wall of AR 4:1 channel increases with Bo as Bo is less than 0.05, then Nu/Nu_0 almost keeps constant. The square channel in Wagner et al. [5] saw the similar heat transfer behaviors. On the both outlet-trailing walls of AR 4:1 rectangular channel and square channel, the heat transfer first decreases, then heat transfer increases with Bo after Bo number passes a turning point.

This turning point is about 0.15 for the square channel, and about 0.2 for the AR 4:1 rectangular channel.

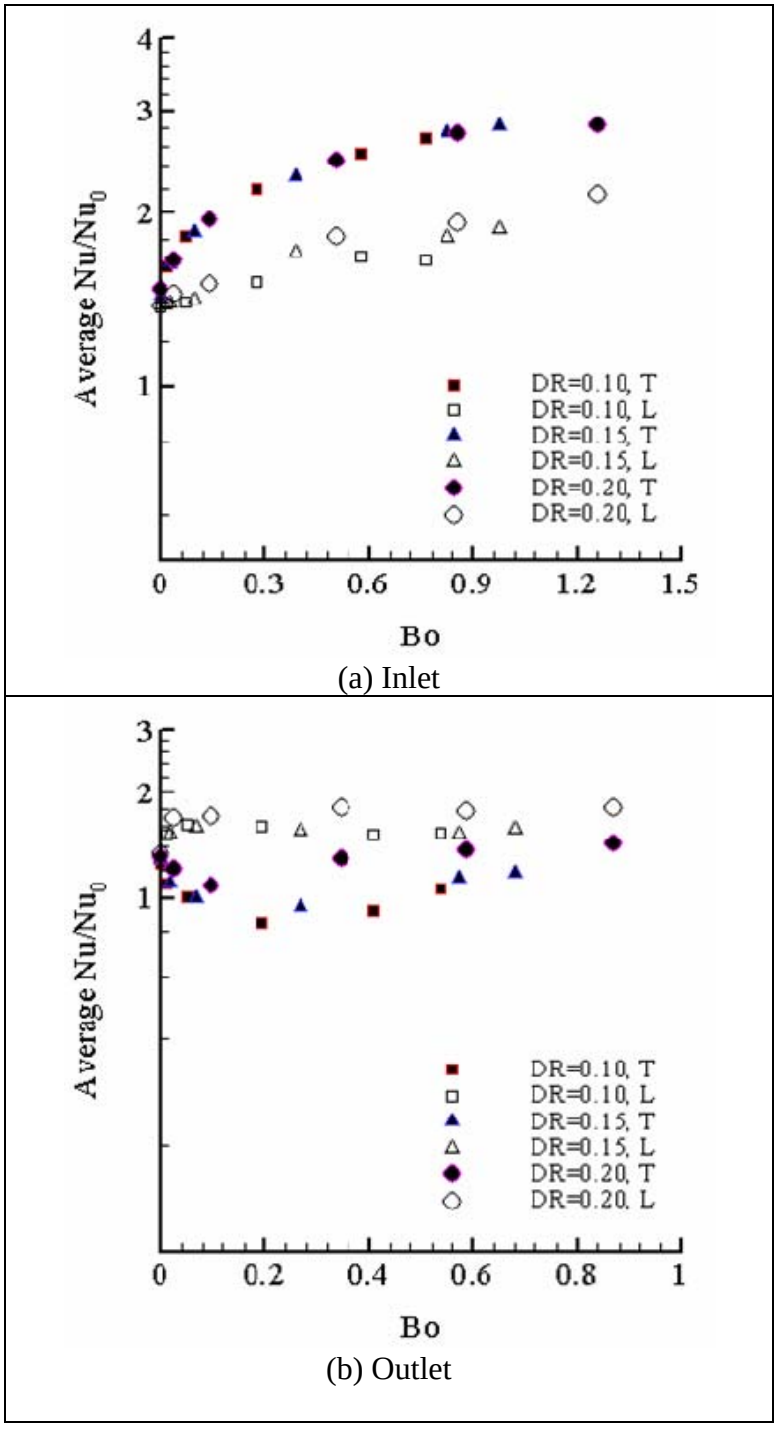

Figure 3.6: Average Nu/Nu_0 vs. Buoyancy parameter at Re=20,000 (a) inlet; (b) outlet

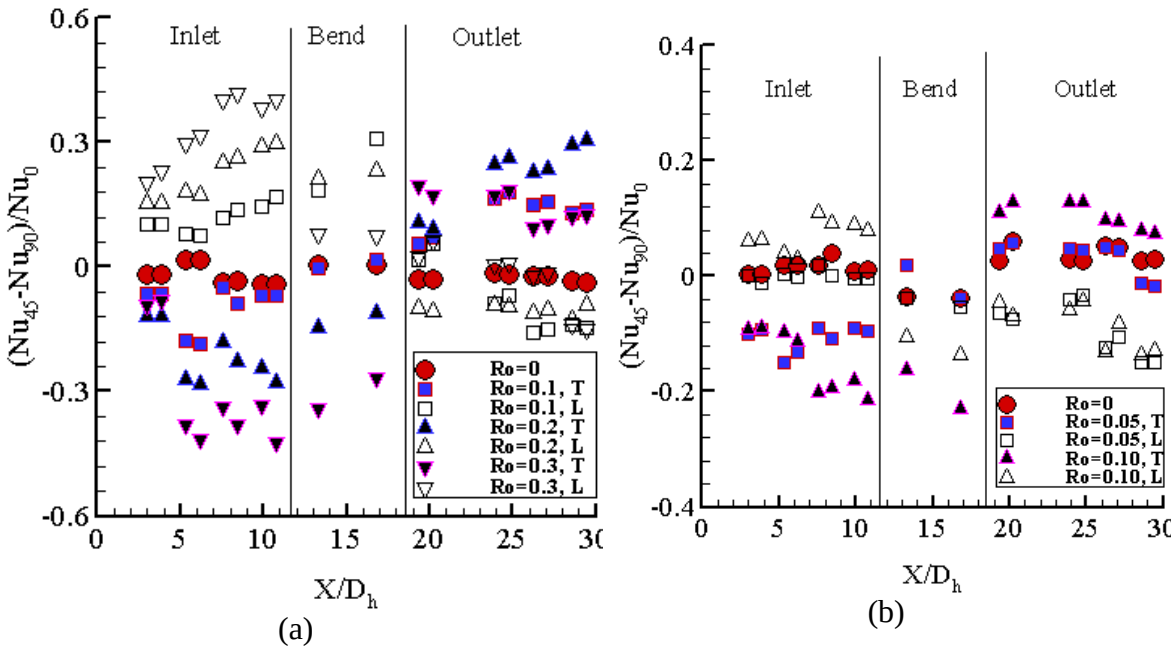

Figure 3.7: Orientation effects with orientation angle 90 and 45 degree, DR=0.1 and Re=20,000 (a) and (b) Re=70,000

3.4 Orientation Effects

Results shown previously were obtained for the 90^0 orientation angle, where the orientation angle is defined as the counter-clockwise angle between the plane parallel to the leading or trailing wall and the plane of rotation. To examine orientation effects, the test model was turned to an orientation angle of 45^0. Two Re values Re=20,000 and Re=70,000 were investigated at this orientation angle with DR=0.1.

With a 90^0 orientation, the Coriolis force is orthogonal to the flow direction, and as discussed earlier, the resulting secondary flows are directed from the leading (stabilized) to the trailing (destabilized) surface in the inlet duct, and in the opposite direction in the outlet duct. With a 45^0 orientation, the Coriolis-force is no longer orthogonal to the leading and trailing surface, and instead it is directed at a 45^0 angle to the leading/trailing surfaces. Thus the secondary flows are expected to be directed from

the outer-stabilized side to the inner-destabilized side where outer and inner refer to the position of the side walls. In view of the altered secondary flow pattern, the leading surface of the inlet duct and the trailing surface of the outlet duct can no longer be viewed as stabilized surfaces, since flow lifts off near one corner and impinges near the other corner (assuming a counter-rotating secondary vortex pair).

Figure 3.7 shows the orientation effects at Re=20,000 and 70,000. The results are presented in the form of Nu/Nu_0 change ($=(Nu_{45} - Nu_{90}) /Nu_0$) versus X/D_h at different Ro numbers. Thus a positive value for Nu/Nu_0 change implies enhancement in Nu in the 45^0 orientation, while a negative value implies a corresponding reduction in Nu.

The Nu/Nu_0 change is nearly zero for the stationary case (Ro=0) as expected. The orientation effects become more significant as Ro increases. In the inlet duct, as Ro is increased, the trailing surface is associated with negative Nu/Nu_0 change values implying a reduction in heat transfer relative to the 90^0 orientation. This reduction is directly linked to the fact that the secondary flows no longer impinge orthogonally on to the mid-span of the surface, but instead impinge at an angle closer to the inner-trailing surface corner. On the leading surface of the inlet duct, the positive values of the Nu/Nu_0 change obtained imply higher values of Nu/Nu_0 in the 45^0 orientation, and are again linked to the altered secondary flow patterns. In the outlet duct, with the 45^0 orientation, higher values of Nu/Nu_0 are again obtained on the stabilized-trailing surface while lower values are obtained on the destabilized-leading surface. The orientation-induced changes are seen to be quite significant Re=20,000 with a maximum change of about $\pm$ 30% at Ro=0.3, but decrease with Re, and at Re=70,000, the maximum Nu/Nu_0 change is $\pm$ 20%.

In the bend region, orientation effects are also seen to be important with degradation levels of the order of 30% on the leading side of the bend. Figure 10 shows that the 45^0 orientation reduces Nu/Nu_0 on the leading side and enhances it on the trailing side. At a lower Re (20,000), in the bend region degradation in Nu/Nu_0 is primarily observed with the 45^0 orientation.

Averaging $(Nu_{45} – Nu_{90}) /N_{u0}$ on both walls show that the orientation angle had almost no effect on the overall Nu/Nu_0 of the channel (Figure 3.8). This implies that orientation effects on the stabilized walls and on the destabilized walls nearly cancel each other out.

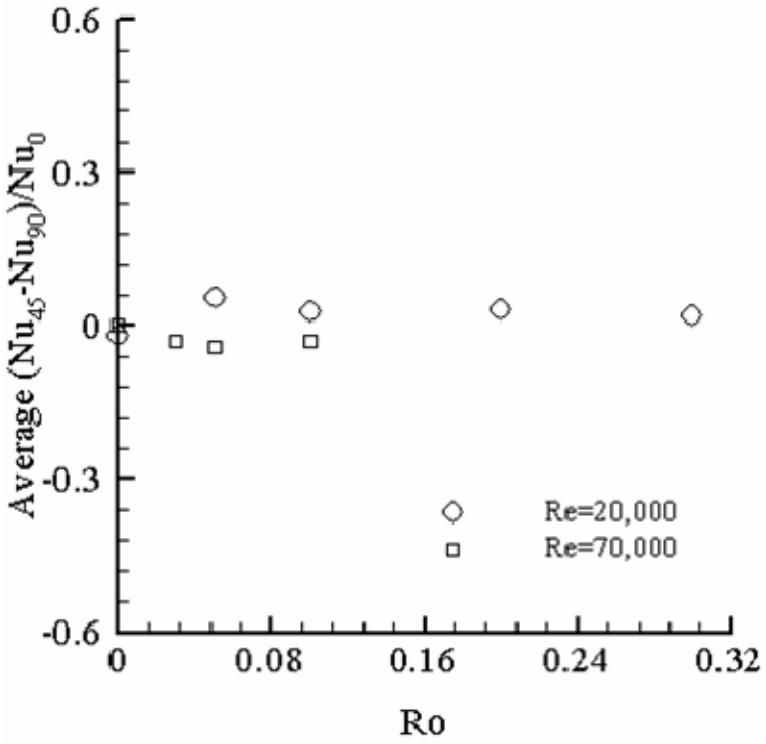

Figure 3.8: Total average of $(Nu_{45} – Nu_{90}) /Nu_0$ on the four walls (inlet leading and trailing and outlet leading and trailing)

3.5 Frictional Factors

During the experiments, the absolute pressure in the entrance of the test section and the pressure drop in the inlet were measured. Figure 11 shows the friction factor values in the range of 1.2-1.4 for Re=70,000, 100,000 and 150,000 with DR=0.1 and an orientation angle of 90 degrees, and shows that Ro does not produce significant changes in the friction factor. No significant changes in the friction factors were observed with a variation of density ratio or change of orientation, and are therefore not presented here.

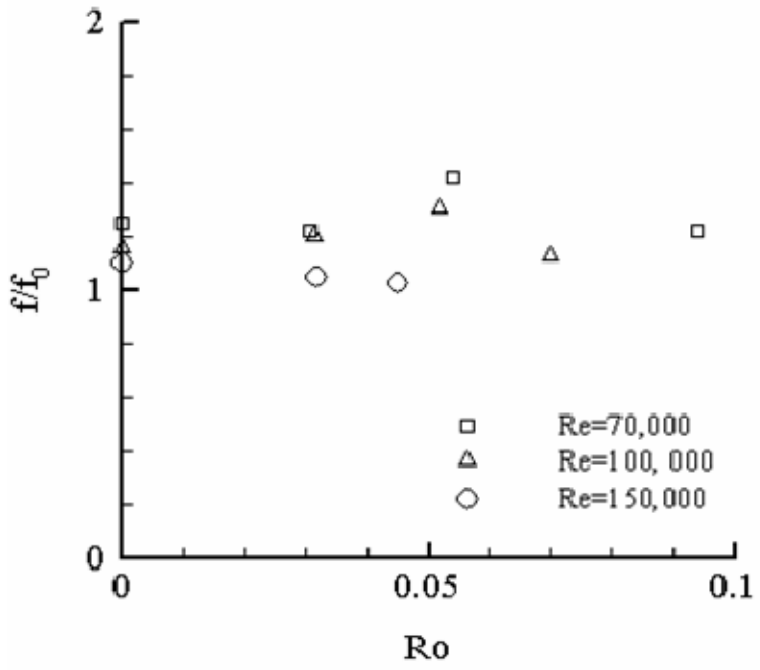

Figure 3.9: Frictional factors in the inlet at DR=0.1

3.6 Concluding Remarks

An experimental study has been undertaken in a rotating heat transfer rig to provide heat transfer measurements in a 4:1 AR smooth coolant passage for a wide range

of Reynolds number and rotation numbers. A maximum Reynolds number of 150,000 and a maximum rotation number of 0.6 are achieved in the study. These maximum parameter values are considerably higher than those previously reported for the 4:1 AR geometry, and provide data for parameter ranges that may be representative of certain modern engines. The following are the main conclusions reached:

1. On the destabilized surfaces of the inlet channel (trailing wall) and outlet channel (leading wall), rotation enhances the heat transfer up to a certain Ro, beyond which the enhancement is flat or reduced. This Ro where the expected trends alter are different in the outlet and inlet channels, and are higher at lower Re.

2. On the stabilized surface of the inlet channel (leading wall) rotation produces an enhancement of heat transfer at low Re, but exhibits degradation at high Re ($\geq$40,000). For the trailing wall of the outlet channel, rotation also enhances the heat transfer at low Re but only at higher Ro.

3. Rotational effects are important in the bend region at lower Re (Re $\leq$20,000) with significant enhancement along the bend-trailing surface.

4. Higher density ratio enhances heat transfer on both leading and trailing walls of the inlet, bend and outlet. In the bend region, the enhancement is more significant on the leading surface. The enhancement also becomes stronger as rotation number increases.

5. Orientation has an important effect on the heat transfer from the leading and trailing surfaces with peak changes of the order of 30% between the 90^0 and 45^0 orientations. In the 45^0 orientation, the heat transfer from the destabilized surfaces reduces while the heat transfer from the stabilized surface increases relative to the 90^0 orientation. The channel-averaged heat transfer is however insensitive to orientation.

CHAPTER 4

PASSAGES WITH 90 DEG RIBS

During the experiments, the pressure in the test section was maintained at 1034 kpa (150 psia). The inlet air temperature varied from 22^{o}c for stationary tests to 35^{o}c for tests at the highest rotational speeds. The wall temperature varied between 55^{o}c to 113^{o}c to achieve the density ratio DR value from 0.10 to 0.20. In the present study, the sidewalls are not heated and not instrumented, so the discussions will focus on the leading walls and trailing walls in the inlet and outlet channels.

4.1 Comparisons with Previous Studies at Stationary Conditions

To validate the experimental procedure, a series of stationary tests at different Reynolds numbers are carried out, and the results are compared to those from previous studies. Figure 4.1(a) shows the Nu/Nu_0 streamwise distributions in the first passage and the comparisons with the 1:1 AR results of Johnson et al. [17] and the 4:1 AR results from Han et al. [12]. Note that the ratio of pitch to rib height (P/e) is 10 for all of the three cases, while e/D_h is 0.10 for the current study and that of [17], and is 0.078 in [12]. Also note that the sidewalls in [17] and [12] are heated, but the sidewalls in the present model are not heated. To minimize any effects caused by the differences of channel aspect ratio, thermal boundary conditions and rib geometry, the Nusselt number Nu is normalized by Nu_0, the value in the fully developed region of the corresponding smooth model without rotation. Nu/Nu_0 in the present study shows a flat distribution along the streamwise direction, and the measured values are generally consistent with those in [12,

17]. The flat streamwise distributions observed in the present study are in contrast to the smooth model results [13] where Nu/Nu_0 decreases with increasing X/D_h, and there is a strong effect of flow development. Further, the average values of Nu/Nu_0 along both leading and trailing surfaces combined is found to be 2.82 in the present study, while it is 2.4 in [17], and 2.6 in [12]. Note that the differences between the various AR cases have been rationalized by normalizing with respect to the corresponding smooth channel value. Therefore the observed differences (17.5%) between the 4:1 AR results of the present study with the 1:1 AR results in [17] arise, in part, to differences in the blockage ratio (e/H) since maintaining the same e/D_h does not ensure the same blockage ratio e/H.

Figure 4.1(b) shows the Nu/Nu_0 distributions along the streamwise direction at Re=25,000 in the inlet, in the bend ($11.5 < X/D_h < 18.4$), and in the outlet, and the results are compared with those of Johnson et al. [17]. For the present study, Nu/Nu_0 is about 2.36 in the bend region, and the bend effects are significant with a drop in the Nu/Nu_0 value going into the bend and a substantial increase immediately downstream of the end. Because of the bend effect, the Nu/Nu_0 in the outlet has a higher average Nu/Nu_0 (~3.08) than in the inlet (~2.82). For the 1:1 AR case [17], Nu/Nu_0 is about 1.8 in the bend region ($14 < X/D_h < 20$), and bend effects are weaker. In the second passage, Nu/Nu_0 is slightly lower (2.20) than in the first passage (2.4). The average value in the outlet in the present 4:1 AR channel is nearly 40% higher than in the 1:1 AR case of Johnson et al. [17].

Figure 4.1(c) presents the Nu/Nu_0 distribution as a function of the Re number in the inlet duct at Ro=0 (stationary case) for the three test models. For the present 4:1 AR model, the average Nu/Nu_0 decreases with increasing Re till about 50,000, beyond which Nu/Nu_0 tends to approach a constant value of about 2.5. Han et al [12] also shows a

decreasing trend in Nu/Nu_0 with increasing Re for the 4:1 channel, but their Nu/Nu_0 values are about 15% lower than those in the present study (presumably due to their lower e/D_h of 0.078). However, for the 1:1 AR case, Johnson et al [17] show a lower sensitivity to the Reynolds number.

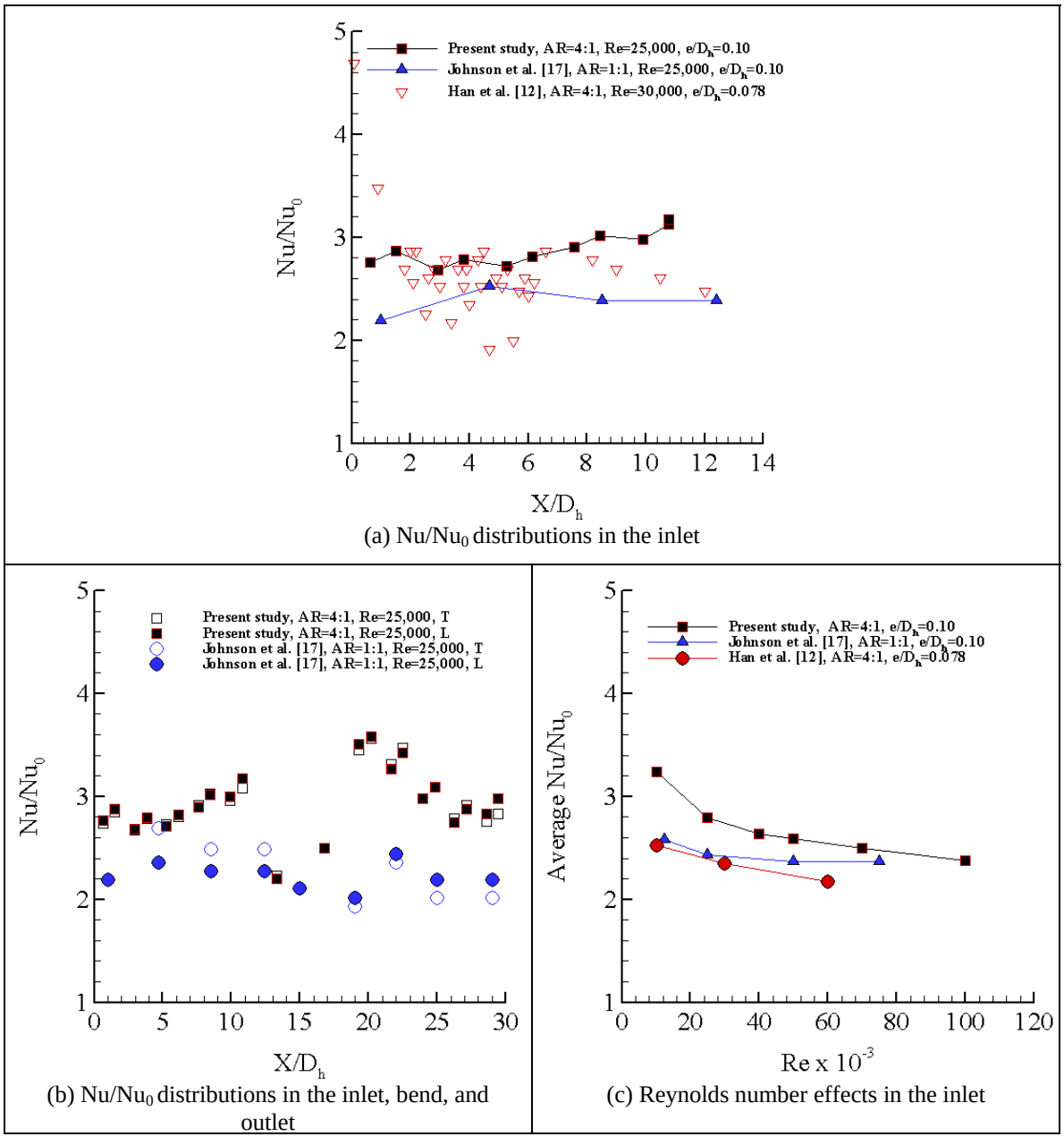

(a) Nu/Nu_0 distributions in the inlet

(b) Nu/Nu_0 distributions in the inlet, bend, and outlet

(c) Reynolds number effects in the inlet

Figure 4.1: Comparisons with previous studies at stationary, P/e=10

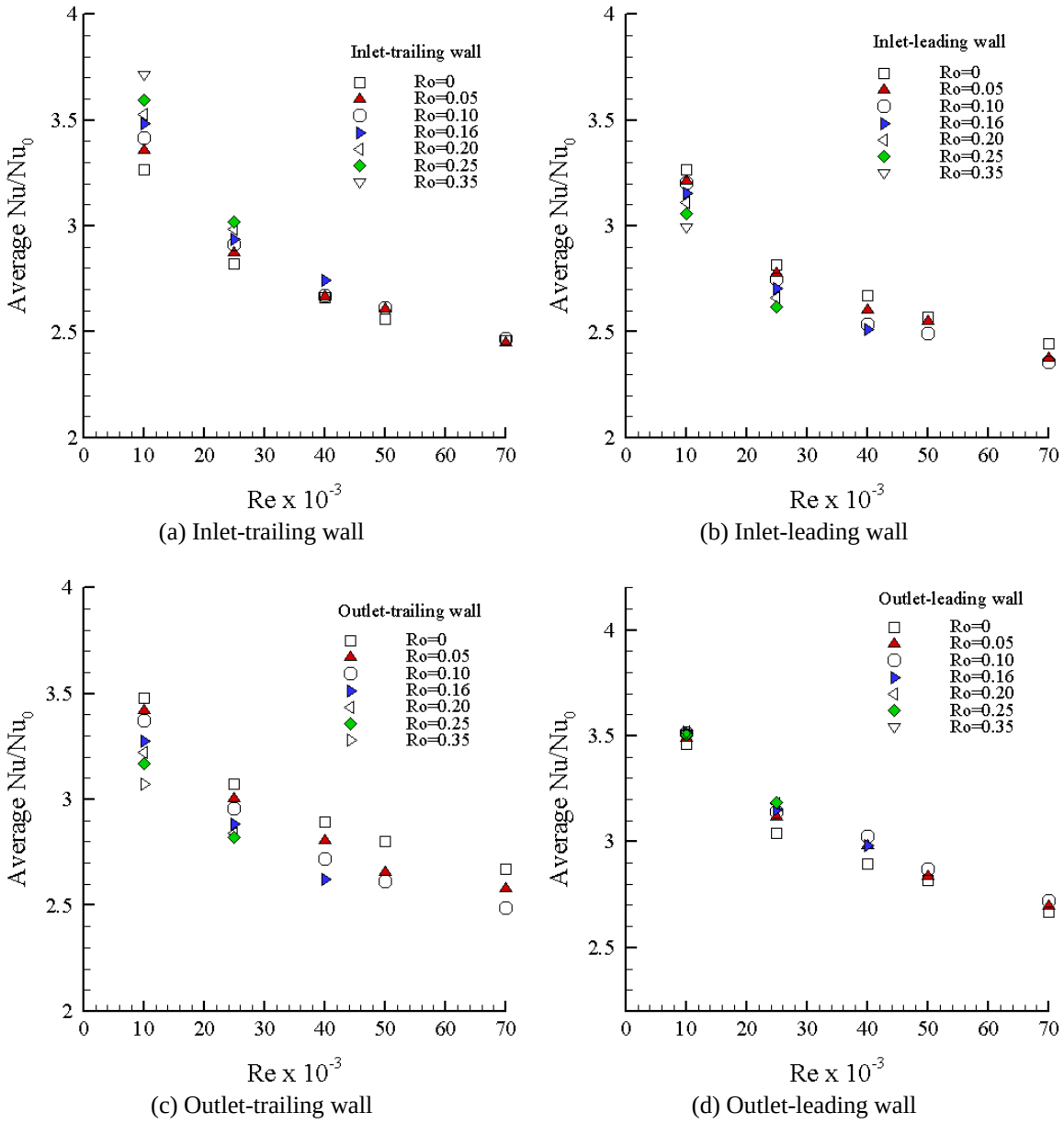

(a) Inlet-trailing wall (b) Inlet-leading wall

(c) Outlet-trailing wall (d) Outlet-leading wall

Figure 4.2: Re number effects with variation of rotation number at DR=0.13

4.2 Reynolds Number Effects

Figure 4.2 shows the Re number effects under rotational conditions for both the leading and trailing walls in the inlet and outlet channels. A maximum Reynolds number of 70,000 is shown for Ro up to 0.1. At higher rotation numbers, the maximum achievable Re is lower. It is clear that on all of the four walls, a distinct Re effect exists,

and for a fixed Ro number, Nu/Nu_0 decreases as Re increases. As for the stationary case, and asymptotic behaviour is noted at high Re with Nu/Nu_0 approaching a value in the range of 2.4 to 2.7.

4.3 Rotation Effects

Figure 4.3 shows the rotation effects on heat transfer ratios in the inlet (Figure 4.3(a)), in the bend (Figure 4.3(b)), and in the outlet (Figure 4.3(c)). The corresponding results for a 1:1 AR channel [6] are also shown for comparison. Note that for both cases, the middle copper plates in the inlet and in the outlet are selected for presentation at a representative Re of 25,000 and DR of 0.13. It should however be noted that the effects of centrifugal buoyancy force cannot be separated from the effects of the Coriolis force by simply keeping density ratio DR as constant. As the rotation speed changes, the centrifugal acceleration also changes, and thus the centrifugal buoyancy force varies even if the DR is kept constant. However, by holding DR constant, and changing the rotation number, the effects of rotational speed (which effects bot the Coriolis and centrifugal-buoyancy forces) can be highlighted.

(a) Destabilized Surfaces (Inlet-Trailing and Outlet-Leading Walls)

For the present 4:1 AR case, the heat transfer ratio increases steadily with increasing Ro on the trailing wall in the inlet passage (Figure 4.3(a)) and along the leading wall in the outlet passage. The increase in Nu/Nu_0 is relatively modest. At a Ro=0.24, there is only a 8% increase over the stationary value in the Nu/Nu_0 along the inlet passage and a 6% increase along the outlet passage. The heat transfer augmentation in Nu/Nu_0 on the destabilized walls is attributed to two major factors in the rotating ribbed channels. First it is well known that the cross-stream secondary flows generated by

the Coriolis forces due to rotation enhance the heat transfer on the destabilized walls. Secondly, the higher rotation speed decreases the reattachment length behind the rib-

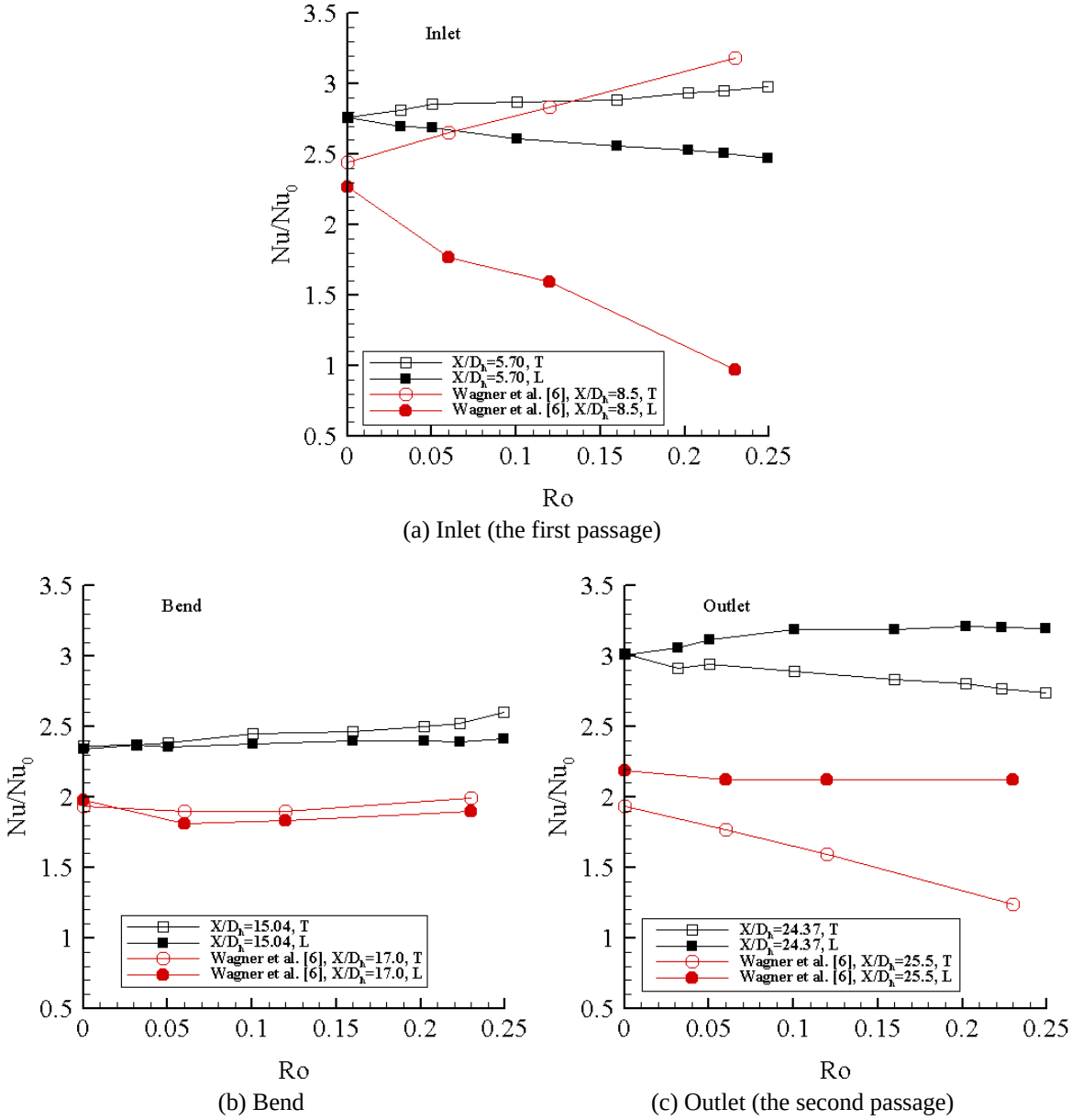

(a) Inlet (the first passage)

(b) Bend

(c) Outlet (the second passage)

Figure 4.3: Rotation effects in comparisons with Wagner et al. [6] at Re=25,000 and DR=0.13

turbulator, as observed by Roche et al. [19]. The reduced reattachment length between a pair of adjacent ribs leads to a larger effective heat transfer coefficient.

While rotation also increases the heat transfer ratio along the destabilized walls in the 1:1 AR channel [6], the enhancement levels in the inlet channel are substantially greater. The increase in Nu/Nu_0 is 45% at Ro=0.23 from the stationary value in the 1:1 inlet leg. On the leading wall in the outlet passage, the increase in Nu/Nu_0 with Ro is only 8% at Ro=0.23. It is therefore clear that while rotational effects for the square and rectangular channels show similar behaviour along the destabilized walls in the range of Ro numbers covered by the current study, the rotation effects are smaller in the present rectangular channels. In a recent computational study performed by Saha and Acharya [35] for 4:1 and 1:1 AR ducts with 90-degree ribs, it was shown that the 4:1 AR ducts produce more complex multi-cellular secondary flow patterns, and as a consequence the differences in the Nu ratio between the trailing and leading walls are smaller for the 4:1 compared to the 1:1 case.

For the 4:1 case, the enhancement levels on the destabilized surface were only slightly higher in the inlet channel compared to the outlet channel while these differences were significant for the 1:1 AR case. As discussed in [6], the centrifugal-buoyancy driven flow opposes the radially-outward coolant flow direction in the inlet passage, leading to enhanced turbulence due to counter-shear effects. In the outlet duct, the flow is directed radially-inwards, and the centrifugal-buoyancy directed flow is in the same direction leading to higher velocities and thinning of the boundary layers. While both the above-noted effects produce an enhancement in the heat transfer levels, it appears that the turbulence enhancement in the inlet duct is the stronger effect particularly for the 1:1 AR channel. Further , the lower enhancement levels in the outlet passage are possibly linked

to the bend effects which delay the re-establishment of the Coriolis-induced secondary flows in the outlet.

(b) Stabilized Surfaces (Inlet-Leading and Outlet-Trailing Walls)

Figure 4.3(a) shows that the heat transfer ratio decreases monotonically with increasing Ro on the leading wall in the inlet, and the same trend also occurs on the trailing wall in the outlet (Figure 4.3(c)). On both walls the largest decreases in Nu/Nu_0 are almost the same (about 10%) at Ro=0.24 from the stationary value. On the leading wall in the bend (Figure 4.3(b)), Nu/Nu_0 almost maintains constant.

The decreases in Nu/Nu_0 on the low pressure walls are also caused by the two major factors as discussed above: the Coriolis force-induced secondary flow patterns and the change of reattachment length between the ribs. In contrast to the case on the high pressure walls, however, the cross-stream secondary flows drive heated, near-wall fluid from the high pressure walls to accumulate near the low pressure walls, thus reduce the heat transfer. In addition, on the low pressure walls, the separated flow over a rib travels a longer distance from the rib with increasing rotation speed, then re-attach to the wall. Such a change of reattachment length, due to the stabilizing effects of corioils force on the low pressure wall, decreases the effective area of heat transfer; thereby further reduce the heat transfer ratio.

In square channels, the heat transfer ratio decreases with Ro increasing on the leading wall in the first passage (Figure 4.3(a)). The largest decreases in Nu/Nu_0 is 52% at Ro=0.23 from the stationary value. On the trailing wall in the second passage (Figure 5(c)), Nu/Nu_0 also decreases with Ro increasing. The maximum decrease in Nu/Nu_0 is

40% at Ro=0.23. But it must be pointed out that, after Ro passes 0.23, the heat transfer ratio increases on the low pressure walls in the square channels as Ro reaches up to 0.35.

Again it is evident that, the rectangular channels and the square channels demonstrate similar behaviors of rotation effects on the low pressure walls, but the rotation effects are much profound in the square channels than in the rectangular channels. As discussed above, this is caused by the larger aspect ratio. And based on the observations of monotonic decrease in Nu/Nu_0 with increasing ro, it suggests that, on the low pressure walls in the ribbed rectangular channels, the heat transfer behaviors are dominated by the Coriolis force-driven secondary flows. The buoyancy-induced effects and the buoyancy force/Coriolis force interactions seem to diminish.

It is interesting to indicate that, on inlet-leading wall in the smooth rectangular channel with AR=4:1, the Nu/Nu_0 was found monotonically increasing with Ro increasing at Re=25,000 and Re=10,000 (Zhou et al. [62]), completely different from the current ribbed walls. Explanations in detail on this phenomenon will be presented in a separate paper.

Figure 4.3(b) shows the rotation effects in the bend region. The trends of the rotation effects on the bend walls are similar to that in the inlet for both rectangular and square channels. That is, the heat transfer on the trailing wall is higher than on the leading wall, and it increases with Ro increasing. The heat transfer on the leading wall doesn't decrease with Ro increasing; however, it almost keeps constant as Ro increases. In general, the rotation effects in both cases are very modest. It is reasonable by considering the following facts: in the bend region, the flow does not move straightly along the radial

direction. So the Coriolis effects in the bend are not as strong as in the straight sections of inlet and outlet. In the current study the flow moves outward along a changing angle relative to the radial direction from 0 deg at entrance of bend to 90 deg at the top of the bend, then travels inward back along the half downstream passage of the bend region. At the exit of the bend, the angle becomes 180 deg, and the flow moves opposite to the radial direction. The Coriolis force changes its direction from pointing to the trailing wall at the entrance of the bend to pointing to the leading wall at the exit of the bend. It can be expected that this change of the direction of Coriolis force further reduce the rotation effects between the bend-leading wall and the bend-trailing wall.

The rotation effects for variable Re numbers from Re=10,000 to 70,000, and Ro=0 to 0.6 are shown in Figure 4.4. The density ratio DR is 0.13 for Re=10,000 to 50,000, and DR=0.10 for Re=70,000. Note that Figure 6 presents the average rotation effects in the inlet and in the outlet. For all of the Re number covered, the rotation effects are consistent. In summary, rotation causes monotonic increase in heat transfer on the high pressure walls, especially on the inlet-trailing walls. On the outlet-leading walls, the enhancements on heat transfer are observed too, but much less than on the inlet-trailing walls. On the other hand, rotation results in monotonic decreases in heat transfer on the low pressure walls. The trend of monotonic decrease in Nu/Nu_0 on the low pressure walls maintains true up to the highest rotation number Ro=0.6 at Re=10,000. No increase in Nu/Nu_0 is observed in the scope of the current experimental parameters.

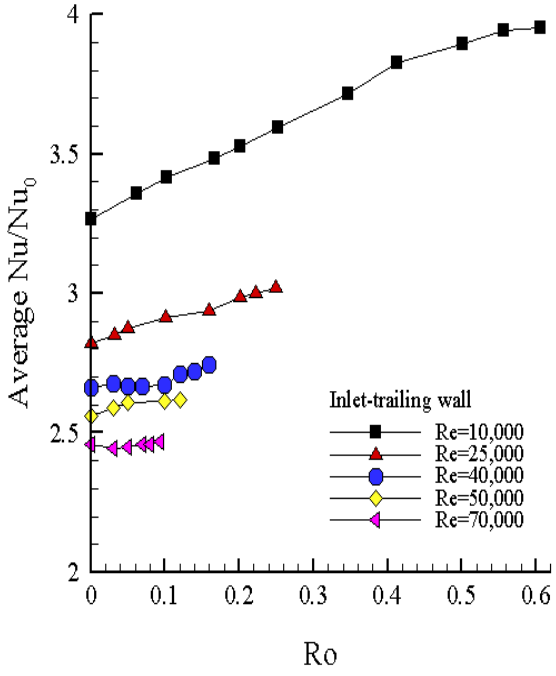

(a) Inlet-trailing wall

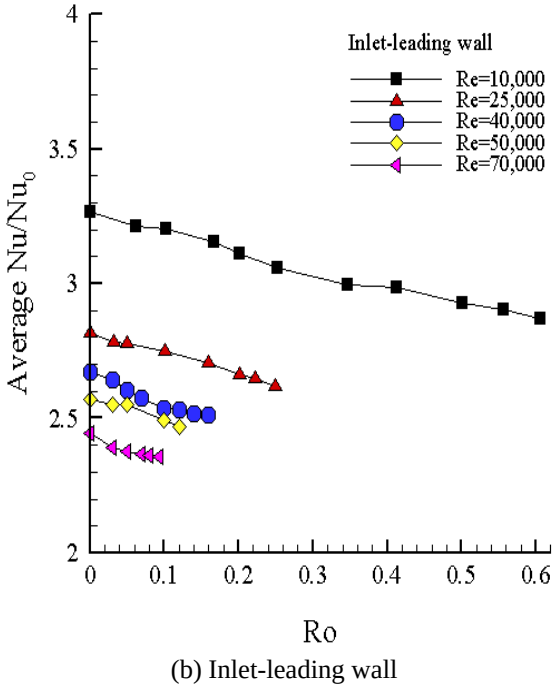

(b) Inlet-leading wall

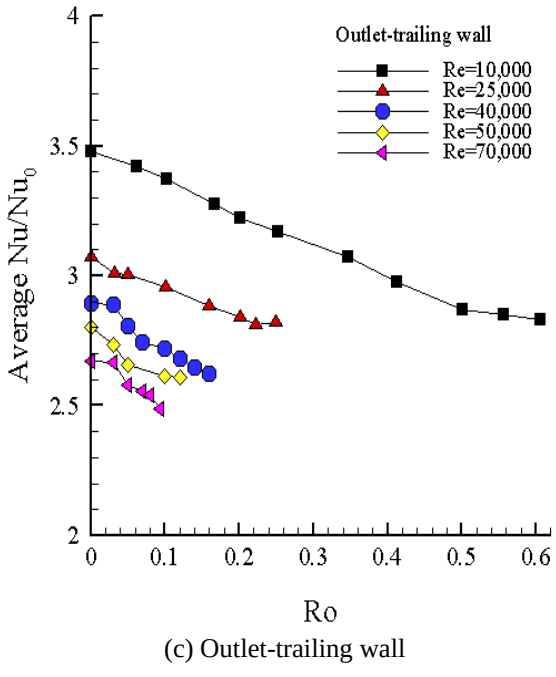

(c) Outlet-trailing wall

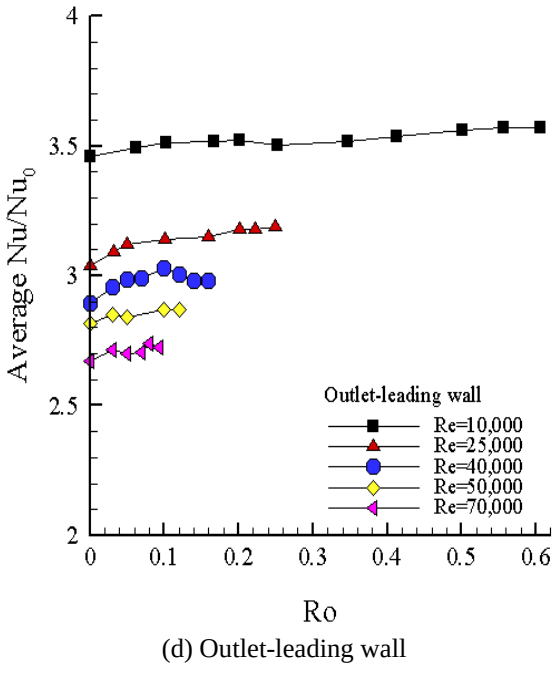

(d) Outlet-leading wall

Figure 4.4: Rotation effects with variable Re numbers at DR=0.13 (DR=0.10 for Re=70,000)

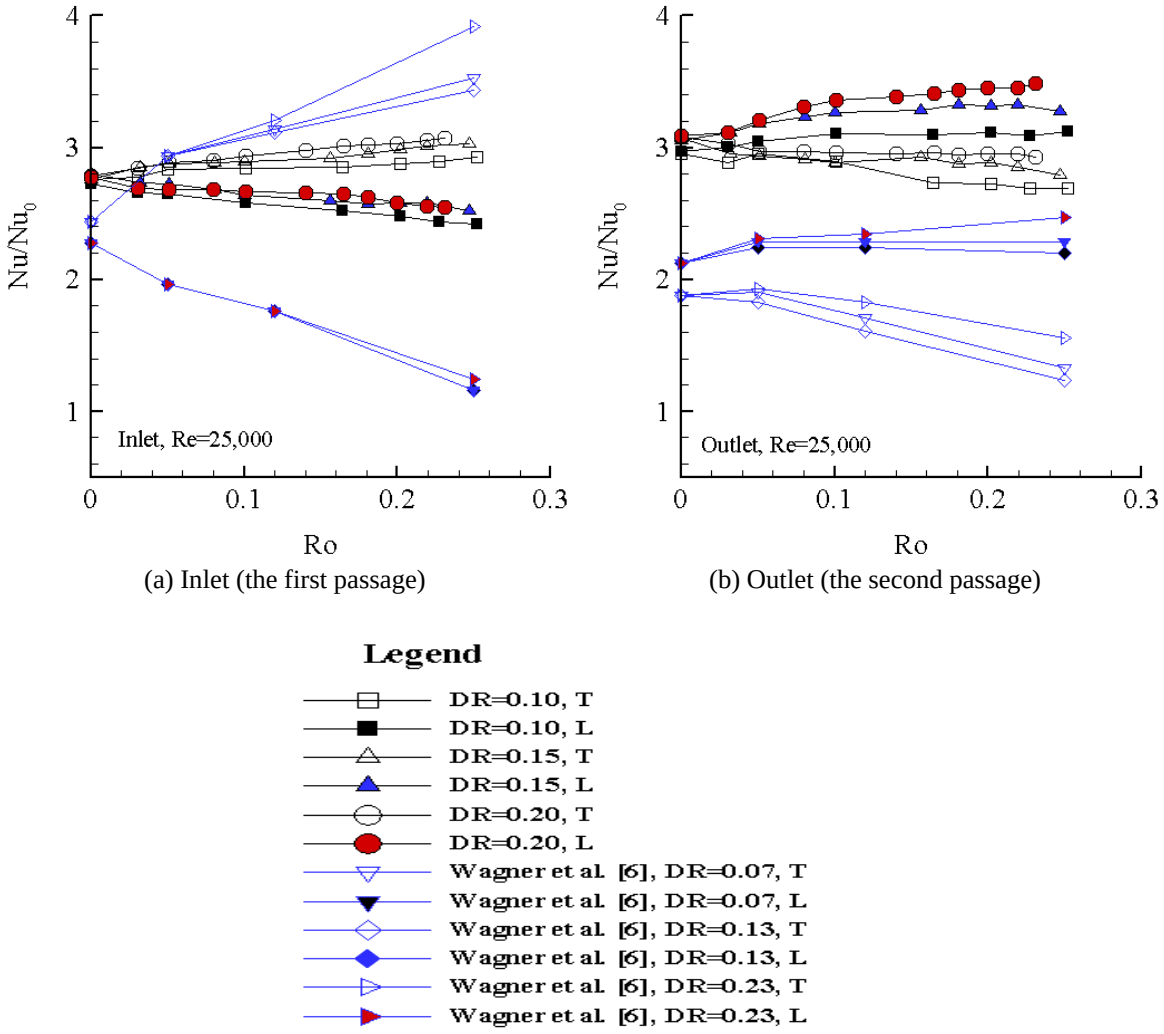

Figure 4.5: DR effects on the middle copper plates at Re=25,000, (a) inlet, (b) outlet

4.4 Density Ratio Effects

The local density ratio is defined as $DR = (\rho_b - \rho_w)/\rho_b = (T_w - T_b)/T_w$. The nominal density ratio for the whole passage is represented by DR at the entrance. Keep in mind that the present study employed uniform wall temperature conditions, and the bulk temperature increases as X increases, so the local density ratio is not uniform along the passage. It decreases as traveling from the entrance of the inlet channel to the exit of the

outlet channel. But for convenience, the nominal density ratio is used in the plots and discussions, if not indicated otherwise.

The density ratio, caused by the temperature gradient normal to the wall, induces the centrifugal buoyancy force on the flow under rotating. This force is expected to become more significant as either DR or Ro number increases. By holding Ro as constant, the contribution of density ratio to the centrifugal buoyancy force can be separated from the contribution of centrifugal acceleration due to rotating.

The two middle copper plates, one on the leading wall and the other on the trailing wall, in the first (inlet, with outward flow) passage, and the two middle copper plates in the second (outlet, with inward flow) passage, are selected to discuss the DR effects. In the present study, X/D_h is 5.7 for the two middle copper plates in the inlet, and X/D_h is 24.4 for the two in the outlet. If R is defined as the local radius (the distance between the center of the copper and the rotation center) of the copper plate, then R/D_h is 65.7 for all of the four plates. Similarly, in Wagner et al [6], X/D_h is 8.5 for the middle copper plates in the first passage, and 25.5 for the two in the second passage. And R/D_h is 49 for all of the four middle copper plates.

Figure 4.5 shows the density effects on the middle copper plates in the inlet and outlet for both rectangular and square channels at Re=25,000 with variation of rotation number. For the rectangular channels, higher density ratio enhances heat transfer on all of the four walls (the inlet-leading wall and inlet-trailing wall in Figure 4.5(a), and the outlet-leading wall and the outlet-trailing wall in Figure 4.5(b)). At Ro=0.23 and as DR increases from 0.10 to 0.20, Nu/Nu_0 increases 5% on the inlet-trailing wall, 3% on the inlet-leading wall, 7% on the outlet-trailing wall, and 9% on the outlet-leading wall.

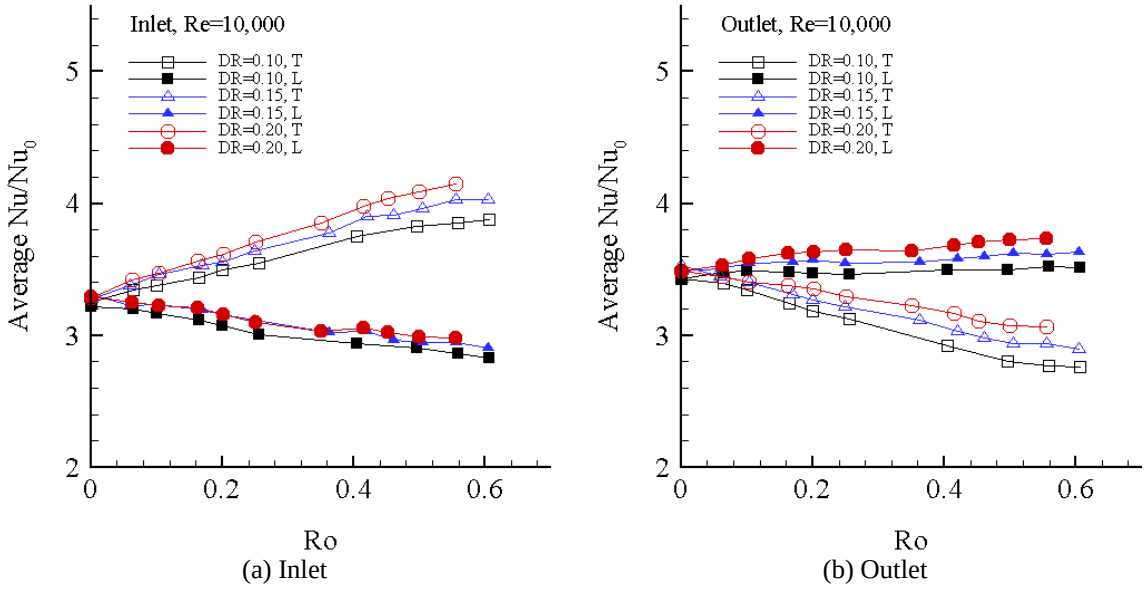

Figure 4.6: Average DR effects at Re=10,000, (a) inlet, and (b) outlet

For the square channel, higher density ratio also enhances heat transfer on all of the four walls. At Ro=0.24 as DR increases from 0.07 to 0.23, Nu/Nu_0 increases 14% on the inlet-trailing wall, 11% on the inlet-leading wall, 26% on the outlet-trailing wall, and 15% on the outlet-leading wall. Larger heat transfer augment at Ro=0.35 was reported in Wagner et al. [6], but not shown in Figure 4.5.

From Figure 4.5, two statements can be drawn. First, at a fixed Ro number higher density ratio intensifies heat transfer on each of the four walls in the first passage and in the second passage for both rectangular and square channels. This is consistently true for each of the Ro numbers covered in the study. Secondly, the DR effects are stronger in the second passage with inward flow than in the first passage with outward flow. This is more evident when considering the fact that the local DR in the outlet is just half of the value in the inlet for both rectangular and square channels. These observations suggest

that, unlike the buoyancy effects caused by increasing centrifugal acceleration, the density effects (or the buoyancy effects caused by increasing density ratio) are stronger in the occasion where the directions of the mean coolant flow and the buoyancy-driven near-wall motion are coincident. And regardless of directions of the mean coolant flow and the Coriolis force, this part of buoyancy effects is always favorable for enhancing the heat transfer on all of the four walls.

Similarly, Figure 4.6 shows the density ratio effects at Re=10,000 with Ro up to 0.6. Again the DR effects discussed above are repeatedly observed. In addition, the rotation effects are also apparent and consistent in Figure 4.5 and Figure 4.6 for both Re=10,000 and 25,000 with each of the three DR values.

4.5 Buoyancy Effects

The combination of the rotation effects and density ratio effects are expected to be represented by buoyancy parameter, which is defined as

$$Bo = [(\rho_w - \rho_b)/\rho_w][\Omega R/V][\Omega D_h/V]$$

where R is the rotation radius. Or in another form:

$$Bo = (DR)Ro^2\ R/D_h$$

Figure 4.7 shows the buoyancy effects on the middle copper plates for both rectangular and square channels the inlets (Figure 4.7(a)) and in the outlets (Figure 4.7(b)) at Re=25,000, R/D_h is 65.7 for the present study and 49 for the square channels employed by Wagner et al [6]. Similarly Figure 4.8 shows the buoyancy effects in the rectangular channels at Re=10,000.

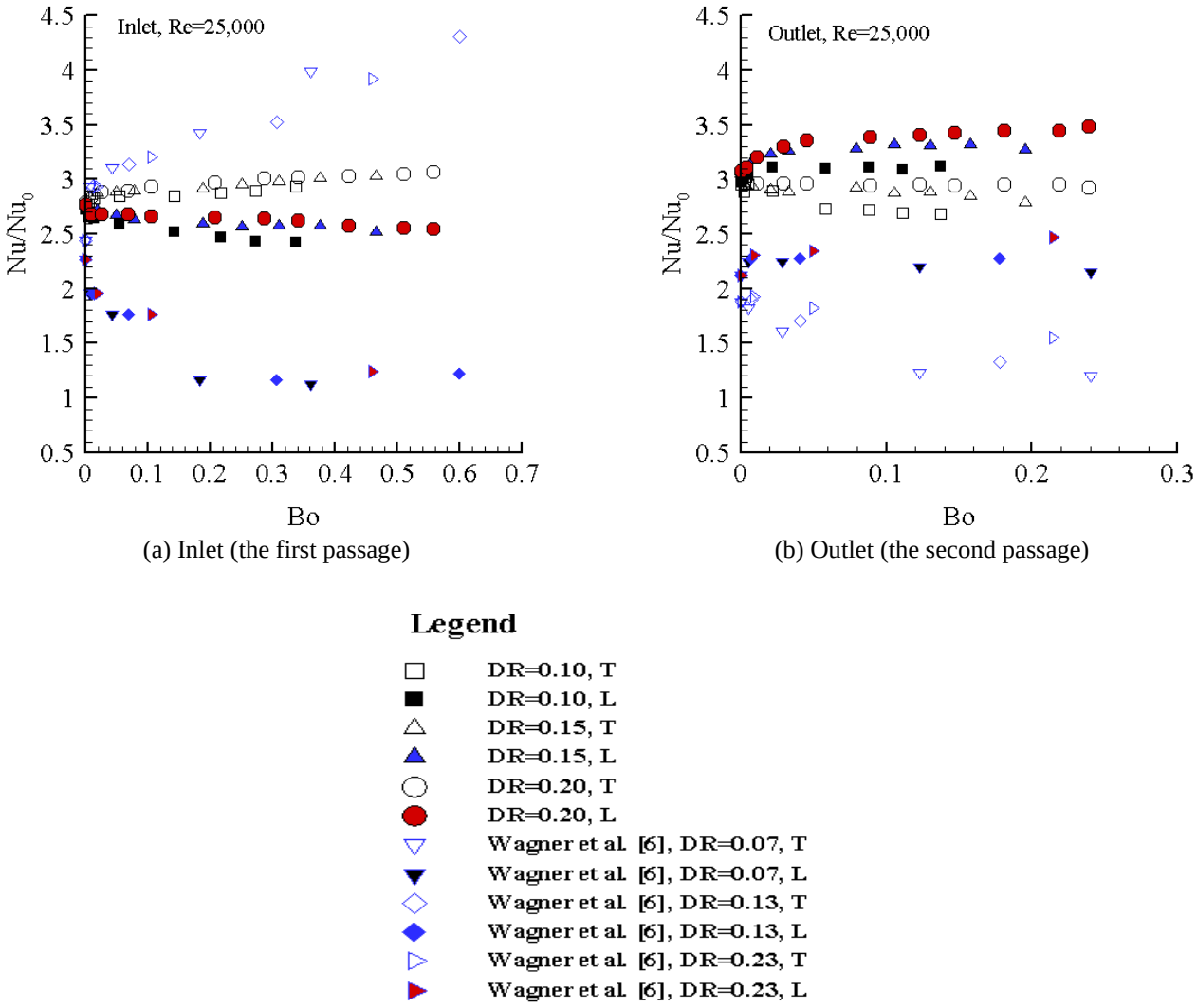

Figure 4.7: Buoyancy effects on the middle copper plates at Re=25,000, (a) inlet, (b) outlet

The buoyancy parameter Bo correlates the buoyancy effects the best for both rectangular and square channels at Re=25,000 (Figure 4.7(a)) on the inlet-trailing walls, where Nu/Nu_0 increases monotonically with Bo increasing. On the leading wall in the second passage, Nu/Nu_0 also increases with Bo increasing (Figure 4.7(b)), but the slope is gentle. Nu/Nu_0 almost keeps constant at lower DR values. On the inlet-leading wall and on the outlet-trailing wall, Nu/Nu_0 decreases monotonically with Bo increasing for the present study. And at higher DR values, Nu/Nu_0 intends to maintain constant as Bo

increases. However, for the square channels Nu/Nu_0 decreases initially from Bo=0 to 0.15, then Nu/Nu_0 increases with Bo increasing.

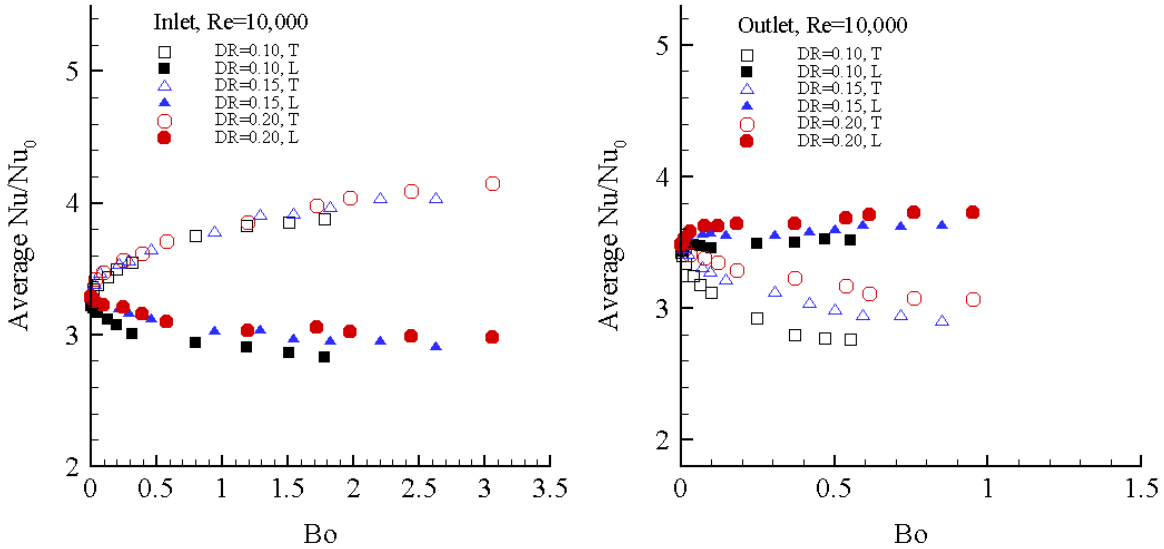

(a) Inlet (b) Outlet

Figure 4.8: Average buoyancy effects at Re=10,000, (a) inlet, (b) outlet

Figure 4.8 shows almost the identical buoyancy effects for Re=10,000 as in Figure 4.7 for Re=25,000. The only difference is that in Figure 4.8 the Bo number is five times as in Figure 4.7, so the margin in Nu/Nu_0 between the leading wall and the trailing wall is much profound. It is obvious in Figure 4.7 and Figure 4.8 that rotation number somehow mainly dominates buoyancy effects in both rectangular and square channels. Recall that two parts cause the buoyancy effects in the rotating coolant passages. One part is contributed by the centrifugal acceleration (rotational gravitation) due to rotating; the other part is contributed by the density ratio dr. And note that in current study and in the study of Wagner et al. [6], DR values only vary from 0 up to 0.23, but the centrifugal acceleration term Ω^2 R increases from 0 to hundreds of g (gravity). This fact explains why buoyancy effects are similar to the rotation effects in both rectangular and square

channels. It also reveals the fundamental difference between the rotational-buoyancy effects in the heated rotating coolant passages and the gravity-driven buoyancy effects on the heated stationary vertical surfaces: in the rotating passages the rotational gravity (the centrifugal acceleration) can be increased substantially as rotation speed increases, then becomes the dominated factor in the rotational buoyancy effects. The change of the rotational gravity along with the variation of density ratio causes the rotational buoyancy effects. While on the heated stationary vertical surfaces, the gravity is fixed; only the change of the density ratio (the temperature gradient normal to the wall) causes the variation of the heat transfer behaviors.

4.6 Thermal Performance Factors

During the tests, the pressure drops in the inlet are recorded. When rotating, the pressure drops are measured with a ScaniValve ZOC14 pressure transducer. The uncertainty is 0.5 psi, which is not good enough for lower Re numbers in the smooth channels. For the ribbed channels, the pressure drops are much higher than in smooth channels, so reliable pressure readings are possible. At each stationary test, the pressure drop is measured with a 100-inch tall U-type anemometer, which provides an uncertainty of 1/8 inch of water.

Figure 4.9 shows the thermal performance factors (TPF) at Ro = 0 based on the pressure drops measured with the U-type anemometer. The thermal performance factors are also compared to the results from Han et al [12]. The TPF in the channel with normal ribs is lower, but close to the results reported by Han et al [12]. Note that $Nu/Nu_{ref,}$ rather than $Nu/Nu_{0,}$ is used to calculate TPF.

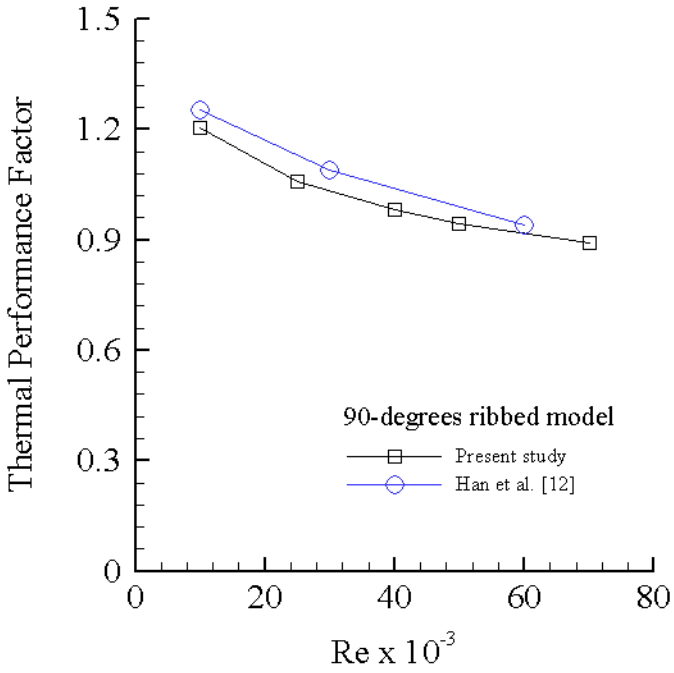

Figure 4.9: Thermal performance factors at Ro=0

4.7 Concluding Remarks

The present experiments examine the effects of rotation number, density ratio, and the buoyancy parameter on heat transfer characteristics in AR=4:1 two-legs internal coolant passages with normal ribs. The results are compared to the data obtained on square rotating channels with same dimensionless rib geometry by Wagner et al. [6]. The following major conclusions are drawn:

1. Rotation effects enhance the heat transfer on the high pressure walls. This enhancement is stronger on the inlet-trailing wall than on the outlet-leading wall. Rotation effects degrade heat transfer on the low pressure walls, and cause monotonic decrease in Nu/Nu_0 on the inlet-leading and outlet-trailing walls. No increase in Nu/Nu_0

is observed on the low pressure walls, even at the highest Ro number of 0.6 at Re=10,000.

2. In the range of Ro number covered in the present study, the present rectangular channels demonstrate similar rotation effects as observed on square channels by Wagner et al. [6]. But the rotation effects are much weaker in the present rectangular channels than in the square channels.

3. Higher density ratio enhances heat transfer on all of the four walls in the inlet and in the outlet. And the enhancement due to density ratio is higher in the outlet considering the fact that density ratio in the outlet is just 50% of that in the inlet.

4. Buoyancy effects in the present rectangular channels demonstrate similar behaviors as rotation effects show. It suggests that the buoyancy effects in the present study are dominated by the centrifugal acceleration due to rotation.

5. The thermal performance factors are calculated for stationary cases. The present results are slightly lower than that obtained in Han et al. [12]

CHAPTER 5

PASSAGES WITH 45 DEG RIBS

During the experiments, the pressure in the test section was maintained at 1034 kPa (150 psia). The inlet air temperature varied from 22^{o}C for stationary tests to 35^{o}C for tests at the highest rotational speeds. The wall temperature varied between 55^{o}C to 113^{o}C to achieve the density ratio DR value from 0.10 to 0.20.

In the present study, the sidewalls are not heated and not instrumented, so the discussion below will focus on the leading walls and trailing walls in the inlet and outlet channels. It should also be noted that the flow coming into the test section is not fully developed as is the case for most real turbine inflow conditions.

5.1 Comparisons with Previous Studies under Stationary Conditions

To validate the experimental procedure, a series of tests under stationary conditions are carried out, and the results are compared with those from previous studies. Figure 5.1 (a) shows the Nu/Nu_0 streamwise distributions in the first passage. The results of Johnson et al. [7], Han et al. [12] and Griffith et al. [13] are also shown for comparison. Note that the ratio of pitch to rib height (P/e) is 10 for all of the three cases, e/D_h is 0.10 for the current study and Johnson et al [7], and 0.078 for Han et al. [12]. Also note that the sidewalls in Johnson et al. [7] and Han et al. [12] are heated, but the sidewalls in the present model are not heated. To minimize any effects caused by the differences of channel aspect ratio, entrance conditions and thermal boundary conditions, the Nusselt number Nu is normalized by Nu_0, the value in the fully developed region of

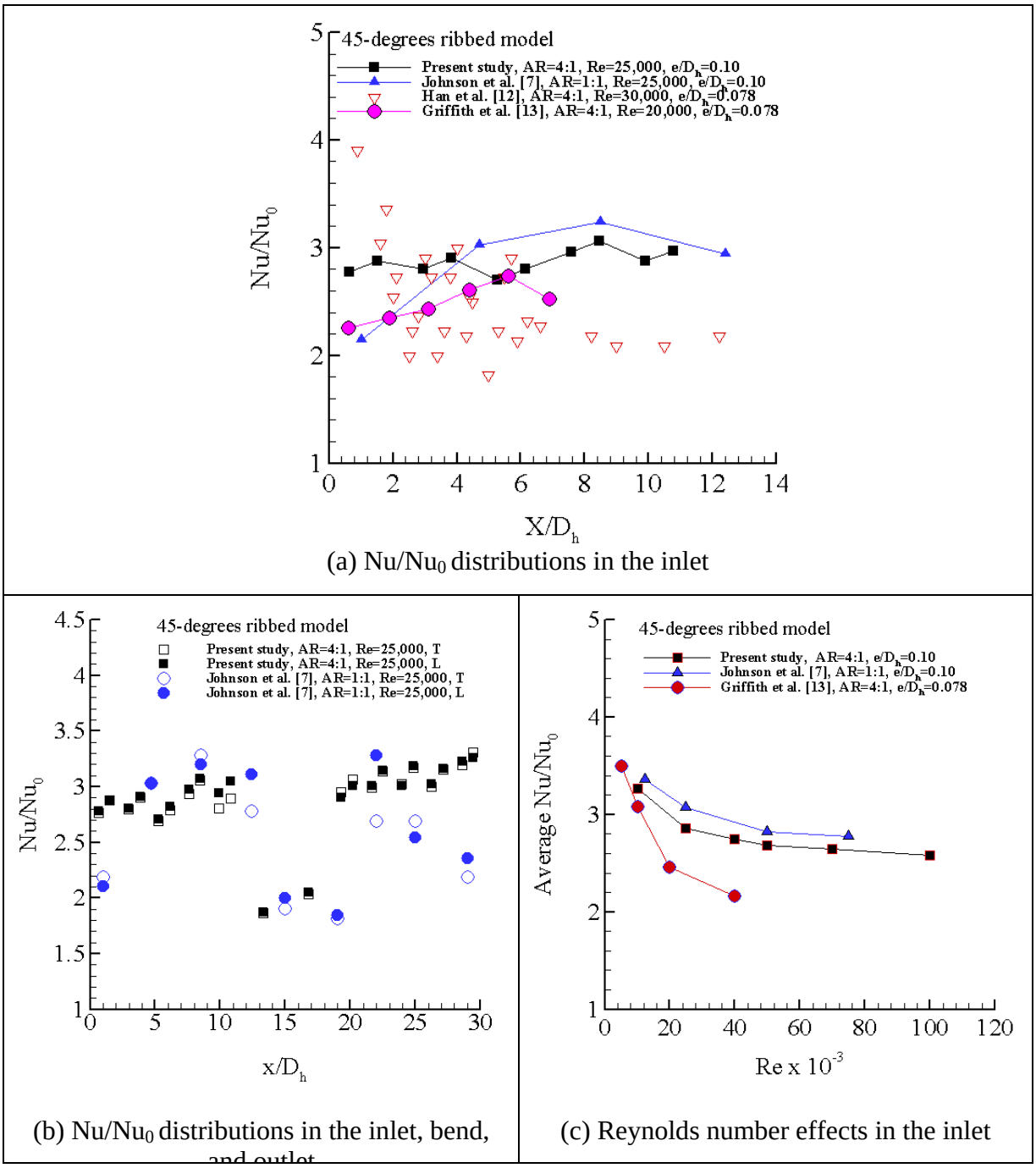

(a) Nu/Nu_0 distributions in the inlet

(b) Nu/Nu_0 distributions in the inlet, bend, and outlet

(c) Reynolds number effects in the inlet

Figure 5.1: Comparisons with previous studies at stationary, P/e=10

the corresponding smooth model under stationary conditions. The Nu_0 value for the 4:1 AR case in the present study is obtained from measurements [62]. The Nu/Nu_0 in the present study shows a relatively flat distribution along the streamwise direction unlike

that of a smooth model where Nu/Nu_0 decreases with increasing X/D_h [62]. Beyond X/D_h of 4, similar behavior is observed by Johnson et al [7] and Han et al. [12]. For $X/D_h < 4$, the observed differences are likely a consequence of differing entrance effects. While there is intrinsic scatter in the data from the different sources, by taking the streamwise-average for the three cases shown in Figure 3(a), it is found that the present study has an average Nu/Nu_0 of 2.87, while it is 3.07 for Johnson et al [7], 2.47 (at Re=30,000) for Han et al. [12], and 2.53 (at Re=20,000) for Griffith et al. [13]. The maximum difference between the present study and the three previous studies is 13%.

Figure 5.1(b) shows the Nu/Nu_0 distributions along the streamwise direction at Re=25,000 in the inlet ($X/D_h \leq 11.5$), in the bend region ($11.5 < X/D_h < 18.4$), and in the outlet ($X/D_h \geq 18.4$), and comparisons are made with Johnson et al. [7]. As in Fig. 3(a), Nu_0 represents the smooth fully developed value for the corresponding AR case, and is different for the 1:1 and 4:1 AR cases. The key difference in trend between the two AR cases is downstream of the bend, where the 1:1 AR case shows a bend effect with a high Nu/Nu_0 on the leading wall immediately downstream of the bend. The 4:1 AR case shows no bend effect, and further, the Nu/Nu_0 values remain relatively flat in the outlet duct unlike the 1:1 AR case where there is a decrease in Nu/Nu_0 with X/D_h.

Figure 5.1(c) presents the variation of Nu/Nu_0 with Re in the inlet duct at Ro=0 for the present case and those reported in [7] and [13]. For all the three models, the average Nu/Nu_0 decreases with increasing Re. For the present model, there is a 23% variation in Nu/Nu_0 in the range of Re=10,000 to 100,000; however beyond a Re=25,000 Nu/Nu_0 values asymptote to around 2.6 with a subsequent decrease of less than 8.6% in

the Nusselt number ratio. Johnson et al [7] show the same trend as observed in the present study with the differences in Nu/Nu_0 between the present study and Johnson et al. [7] being around 5%. In Griffith et al. [13], significant Re effects are however observed. Nu/Nu_0 drops from 3.5 to 2.2, as Reynolds numbers changes from 5,000 to 40,000. The maximum difference between the Nu/Nu_0 in the present study and Griffith et al. [13] is 25%.

5.2 Reynolds Number Effects

In Figure 5.1(c), Re number effects are shown for Ro=0. Figure 5.2 shows the Reynolds number effects for the rotational cases along both the inlet and outlet ducts. It is clear from Figure 4 that there is a consistent Reynolds number effect for all cases with rotation, and that this effect is comparable in magnitude for the various Ro. As for the stationary case, there is an asymptotic behavior for $Re \geq 25{,}000$ beyond which the Re effects are weak.

5.3 Rotation Effects

Figure 5.3 shows the rotation effects on the heat transfer ratio in the inlet (Figure 5.3(a)), in the bend (Figure 5.3(b)), and in the outlet (Figure 5.3(c)) for Re=25,000 and DR= 0.13. The results for square channels from Johnson et al. [7] are also shown for comparison. Note that for both cases, the data presented is at the mid-point in the inlet and in the outlet. Rotation number is varied from 0 to 0.25. It should be noted however that the effects of centrifugal buoyancy cannot be separated from the effects of the Coriolis force by simply keeping density ratio DR as constant.

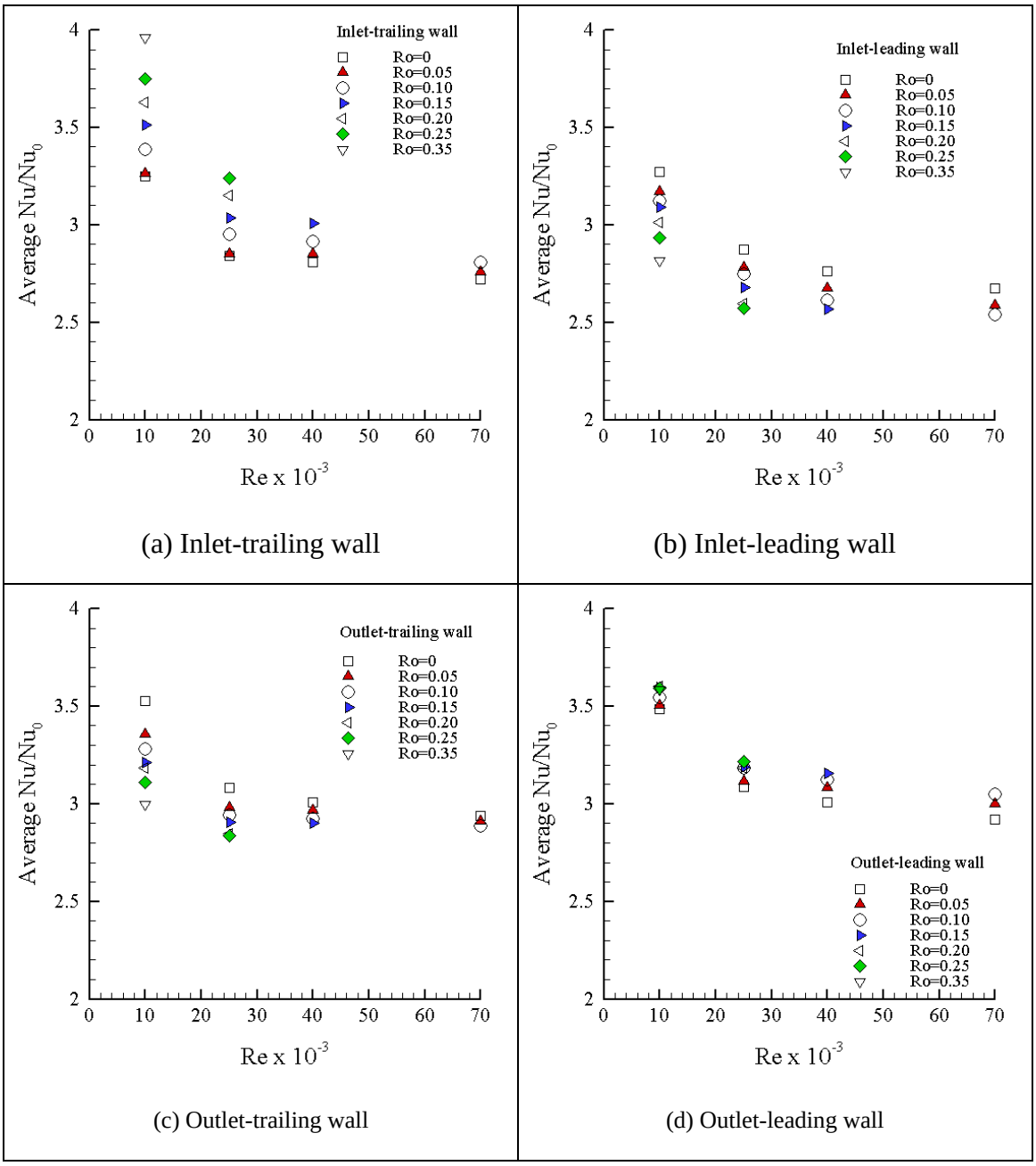

Figure 5.2: Re number effects with variation of rotation number at DR=0.13 (DR=0.10 for Re=70,000)

- **Destabilized Surfaces**

For the 4:1 AR channel, it can be seen that Nu/Nu_0 increases steadily with rotation number along the trailing wall in the inlet passage and the bend and along the leading

wall in the outlet passage. These surfaces that see enhancement, called destabilized surfaces, have Coriolis-induced secondary flows (proportional to the rotation number) directed toward them. These secondary flows that impinge on the destabilized surface enhance mixing and turbulence along the surface, and therefore also increase heat transfer. This behavior has been extensively documented and quantified for the 1:1 AR geometry [4-7]. In the inlet passage Nu/Nu_0 along the trailing surface increases by 14% at Ro=0.25 from its stationary value. In the outlet passage and along the bend, the corresponding increase in Nu/Nu_0 with rotation is only about 5% at a Ro=0.25. The comparison with square channel data [7] indicates that there is an increase of 21% in Nu/Nu_0 as Ro is increased to 0.23 from the stationary condition. On the trailing wall in the bend, Nu/Nu_0 shows only a slight increase as in the 4:1 rectangular channel. On the leading wall in the second passage, the increase in Nu/Nu_0 is only 9% at Ro=0.23.

It is clear that the rotation effects in the square and rectangular channels show similar behavior on the destabilized walls in the range of Ro numbers covered by the current study. The key difference appears to be that rotation-induced enhancements on the destabilized surface appear to be substantially smaller (by as much as 40%) for the 4:1 AR relative to the 1:1 AR geometry. The smaller rotation effects in the current rectangular channels relative to the square channels are attributed to the Coriolis force-induced secondary flow cells being weaker as the AR increases and the leading wall and the trailing wall get closer.

The larger increase in Nu/Nu_0 on trailing wall in the first passage relative to the second passage (observed for both 4:1AR and 1:1AR) is caused by the extra generation of near-wall turbulence due to the buoyancy-driven flow close to the wall, as discussed

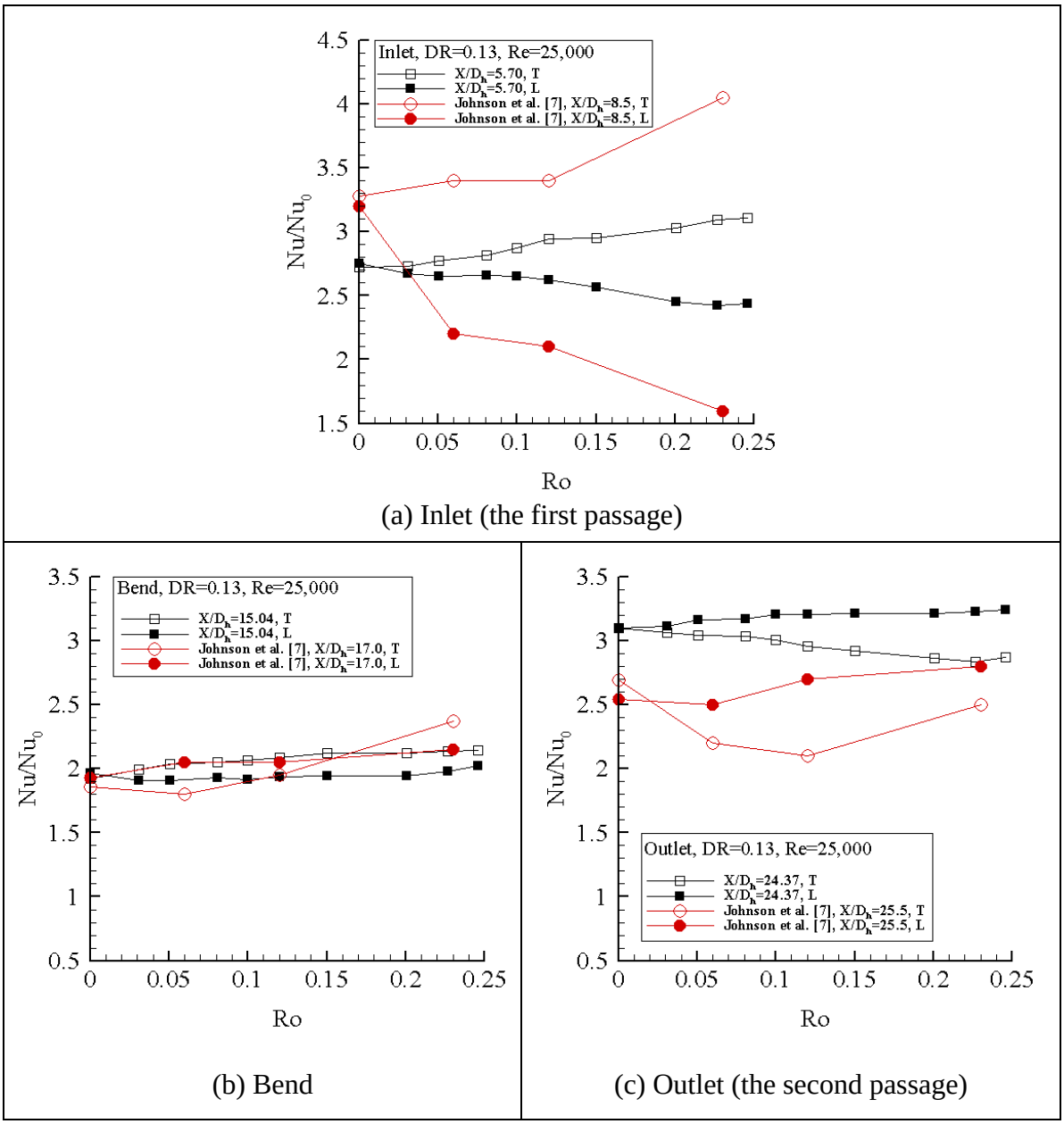

Figure 5.3: Rotation effects in comparisons with Johnson et al. [7] at Re=25,000 and DR=0.13

by Johnson et al. [7]. In the inlet, the near-wall centrifugal buoyancy-driven flow moves inward toward the axis of rotation, and the mean coolant flow is radially outward. This counter-flow pattern generates additional near-wall turbulence due to the strong shear or velocity gradient. In the second passage, the direction of the mean coolant flow and the

near-wall buoyancy-driven flow are coincident, and the generation of the near-wall turbulence is likely to be weaker.

- **Stabilized Surfaces**

In Figure 5.3(a), the behavior on the stabilized surface in the inlet-leading wall for the 4:1 AR is generally consistent with those of the 1:1 AR. In both cases, the heat transfer ratio decreases with Ro. A similar behavior is seen for the outlet-trailing wall except that for the 1:1 AR there is an initial decrease till Ro=0.12 followed by a small increase at Ro=0.23.

For the 4:1 AR the largest reduction in Nu/Nu_0 with Ro is almost the same on both walls (10% decrease on the inlet-leading wall and 8% on the outlet-trailing wall at Ro=0.25 relative to the stationary value). In square channels, along the leading-inlet wall there is a decrease in Nu/Nu_0 of 51% at Ro=0.23 from the stationary value (Figure 5.3(a)). On the trailing wall in the second passage (Figure 5.3(c)), Nu/Nu_0 initially decreases with Ro by 21% at Ro=0.12 beyond which there is a modest increase.

It is evident that the rotation effects are much greater in the 1:1 square channel than in the 4:1 rectangular channel. In the inlet-channel the reduction on the stabilized surface is nearly five-fold greater for the 4:1 AR, while in the outlet-channel the reductions in Nu/Nu_0 are two-fold greater for the square channel. It should be noted that the present results are in contrast to that of Griffith et al. [13] who, for a 4:1 AR 45-degree ribbed channel, reported a monotonic increase in heat transfer rate on the leading wall with radially-outward flow in the range of Re=5,000 to 40,000. However, their study at Re=40,000, the maximum rotation number was only Ro=0.038. In the present study, Ro numbers up to 0.25 at Re=25,000 have been studied, and a monotonic decrease is

observed over this range. It should be noted that Zhou et al. [62], for a 4:1 smooth channel, also observed an increase in the inlet-leading heat transfer with Ro. This behavior was rationalized through companion computational results which showed that for the 4:1 smooth channel, a multi-roll secondary flow pattern was observed, and that both the leading and trailing surfaces experienced downwash of the secondary flow resulting in enhanced heat transfer on both surfaces with rotation. However, with inclined ribs on the wall, the secondary flow pattern is likely to be different, and the present measurements support this expectation.

Figure 5.3(b) shows the rotation effects in the bend region. For the present 4:1 model, rotation effects in the bend are rather small as for the square channel. This is to be expected since the flow over a significant portion of the bend is oriented in the direction of rotation leading to reduced Coriolis forces.

To provide a better perspective of the rotational effects at all Reynolds number studied (10,000-70,000), the 4:1 AR data in the form of streamwise-averaged Nu/Nu_0 is plotted separately for each wall, and each Re, as a function of the Ro (Figure 5.4). At each Re, the rotational effects are consistent with that shown in Figure 5.3. Rotation causes a monotonic increase in the heat transfer on the destabilized walls, and this effect is clearly greater in the inlet channel. In the outlet channel, the enhancement appears to decrease somewhat with decreasing Re. In fact, at Re=10,000, Nu/Nu_0 along the outlet-leading wall almost remains constant over the full range of Ro values from 0 to 0.6. On the other hand, rotation results in a monotonic decrease in heat transfer on the stabilized walls. The only exception occurs again at Re=10,000 with Ro higher than 0.4, where the

Nu/Nu_0 on the inlet-leading wall increases as Ro increases, implying that at these conditions the buoyancy-driven effects overrides the Coriolis-force effects on this wall.

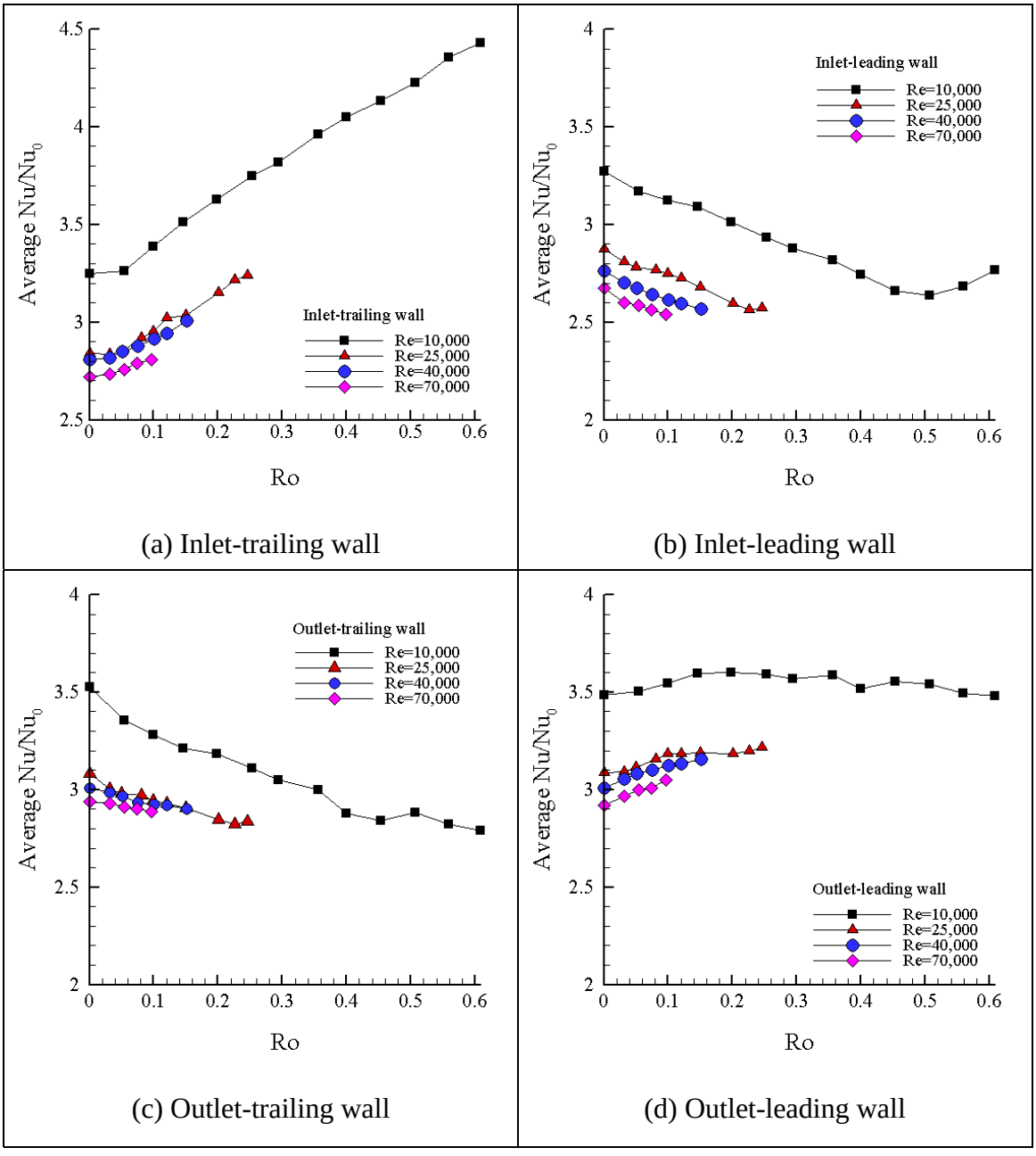

Figure 5.4: Rotation effects with variable Re numbers at DR=0.13 (DR=0.10 for Re=70,000)

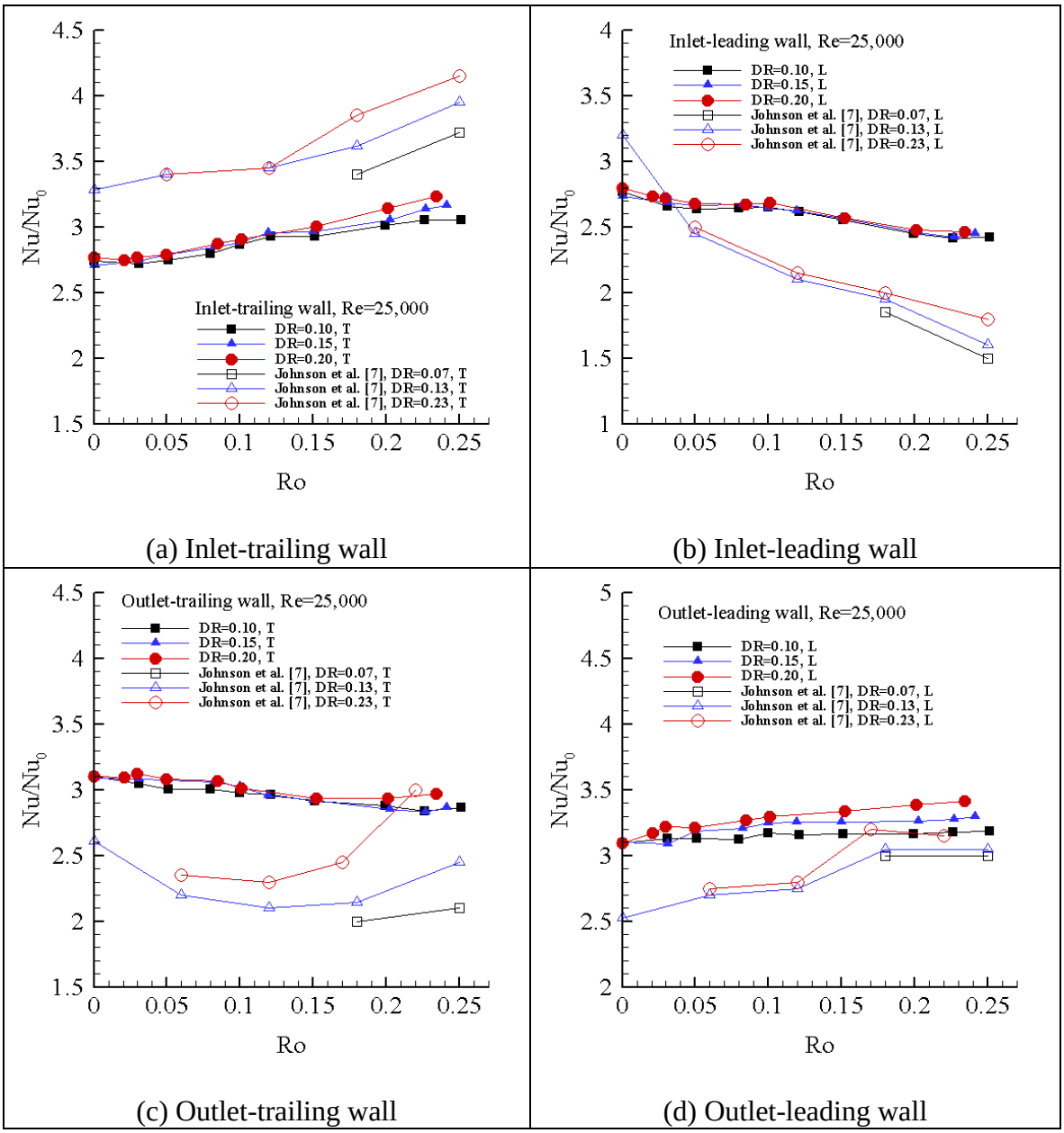

Figure 5.5: DR effects on the middle copper plates at Re=25,000

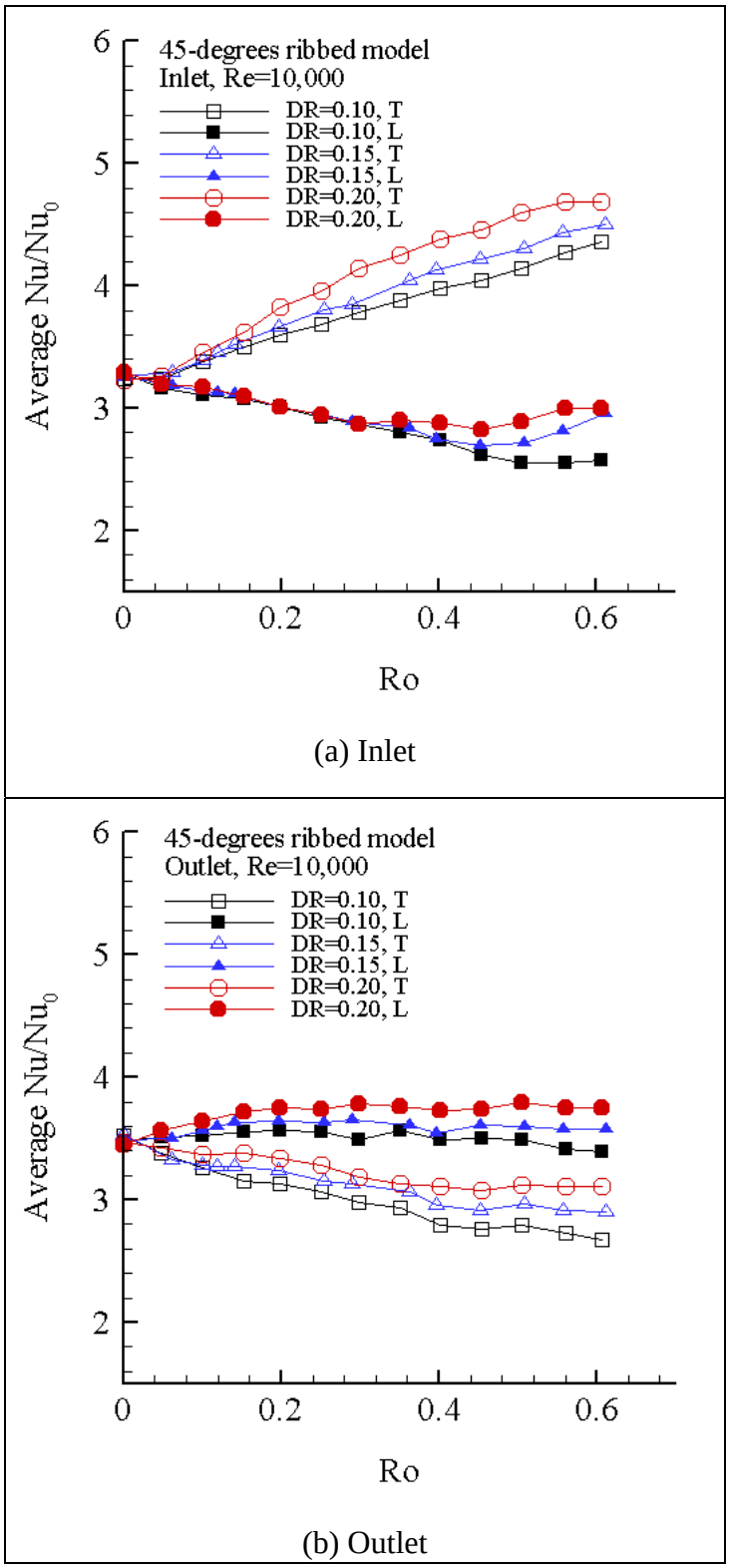

Figure 5.6: Average DR effects at Re=10,000, (a) inlet, and (b) outlet

5.4 Density Ratio Effects

The local density ratio is defined as $DR = (\rho_b - \rho_w)/\rho_b = (T_w - T_b)/T_w$. In the present study, the inlet bulk density is used implying that the nominal density ratio for the whole passage is represented by DR at the entrance. The density ratio, caused by the temperature gradient normal to the wall, induces the centrifugal buoyancy force on the flow under rotational conditions. This buoyancy force is expected to become more significant as either DR or Ro number increases. By holding Ro constant, the influence of DR can be examined.

Figure 5.5 presents the Nu/Nu_0 ratio for different DR at the mid-point of the channels: X/D_h =5.7 for the inlet, and X/D_h=24.4 for the outlet. At this mid-point location, R/D_h is 65.7, where R is defined as the local radius of the mid-point of the channel. Also shown are the results of Johnson et al. [7] for ribbed square channel at the mid-point of the inlet and outlet channels. These results are presented at Re=25,000.

In general, increasing DR increases Nu/Nu_0 for both the 1:1 AR and 4:1 AR ribbed channels, but the DR effects for the 4:1 AR channels are relatively small and of the order of the measurement uncertainty. However, these measurements are repeatable and repeated runs produced the same behavior. For the 4:1 AR, the effects of DR on the stabilized surfaces are marginal (~2-4%), while on the destabilized surfaces the Nu/Nu_0 increases by 6-7% at Ro=0.23 when DR is doubled from 0.1 to 0.2. For the square channel, the effects of DR are more evident. At Ro=0.24 as DR increases from 0.07 to 0.23, Nu/Nu_0 increases 15% on the inlet-trailing wall, 5% on the inlet-leading wall, 43% on the outlet-trailing wall, and 20% on the outlet-leading wall.

From these differences, it is clear that the DR effects are stronger in the second passage with radially-inward flow than in the first passage with radially-outward flow.

The density ratio effects are more clearly shown in Figure 5.6 for Re=10,000 with Ro up to 0.6. Again the heat transfer enhancement due to higher DR is observed. In Figure 5.6(a), the increase in Nu/Nu_0 on the inlet-leading wall is observed for each of the three DR values only after Ro passes a critical point and approaches higher values. Note that the critical Ro becomes smaller as DR increases. This fact clearly indicates that it is the centrifugal buoyancy force that causes this phenomenon.

5.5 Buoyancy Effects

The combination of rotation effects and density ratio effects can be represented by a buoyancy parameter, which is defined as

$$Bo = [(\rho_w - \rho_b)/\rho_w][\Omega R/V][\Omega D_h/V]$$

where R is the rotation radius. Expressed in another form, the Buoyancy parameter can be written as:

$$Bo = (DR)Ro^2\, R/D_h$$

The buoyancy parameter Bo correlates the buoyancy effects for both rectangular (4:1) and square (1:1) channels at Re=25,000 (Figure 5.7) reasonably well on the destabilized surfaces (inlet-trailing and outlet-leading). Nu/Nu_0 for the destabilized surface increases monotonically with increasing Bo. On the stabilized surfaces (inlet-leading and outlet-trailing), Nu/Nu_0 for the 4:1 AR initially decreases with increasing Bo, but at higher Bo values, Nu/Nu_0 plateaus (Figure 5.7(b)) or increases slightly (Figure 5.7(c)) with Bo. For the 1:1 AR a similar behavior is observed, but the correlation with

respect to the Bo is better for the rectangular channel than for the square channel. It was shown earlier that the effects of both the Ro and DR are weaker for the 4:1 AR channel, and the better correlation with Bo for the 4:1 AR may be a consequence of this fact.

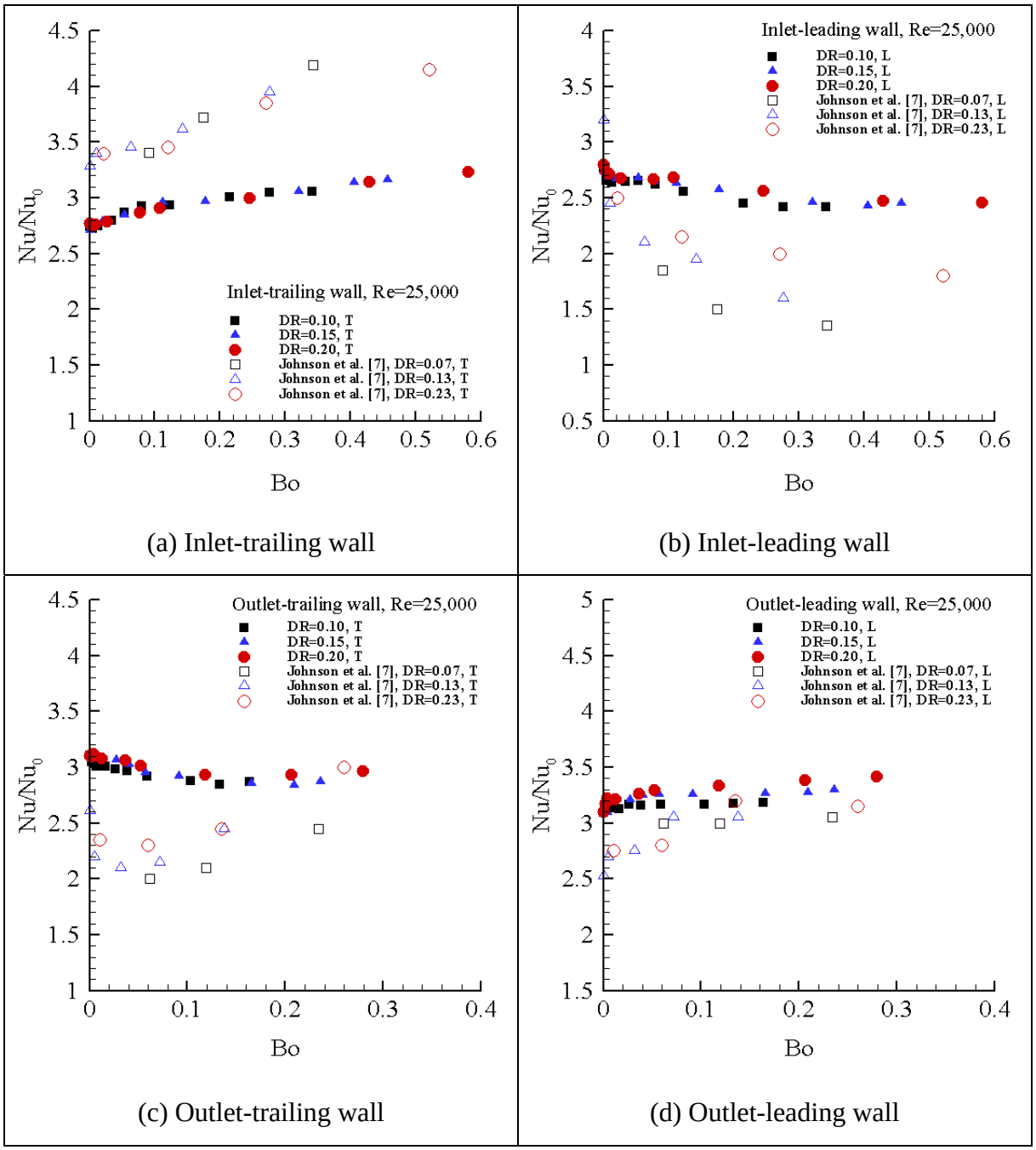

Figure 5.7: Buoyancy effects on the middle copper plates at Re=25,000

Figure 5.8 shows the buoyancy effects for Re=10,000 in the inlet duct with Bo parameters as high as 3. Once again, Bo appears to be a good correlating parameter.

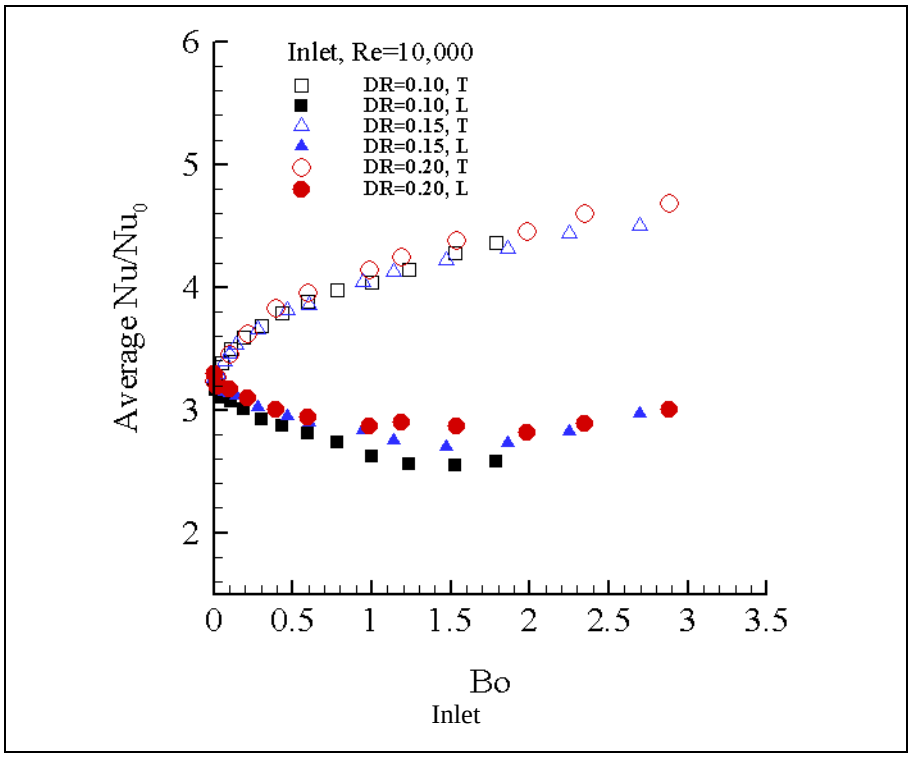

Figure 5.8: Average buoyancy effects at Re=10,000, inlet

5.6 Thermal Performance Factors

Figure 5.9 shows the thermal performance factors (TPF) at Ro = 0 based on the pressure drops measured with a Scanivalve ZOC-14 transducers. These pressure drops were normalized to yield friction factors (Eq. 6 in Chapter 2) that are then combined with the Nu/Nu_0 to yield thermal performance factors (Eq. 7 in Chapter 2). It should be noted that the TPF values reported in the present paper extend up to a Re of 100,000, and show that beyond a Re of 50,000, the TPF remain fairly flat at around 1.3.

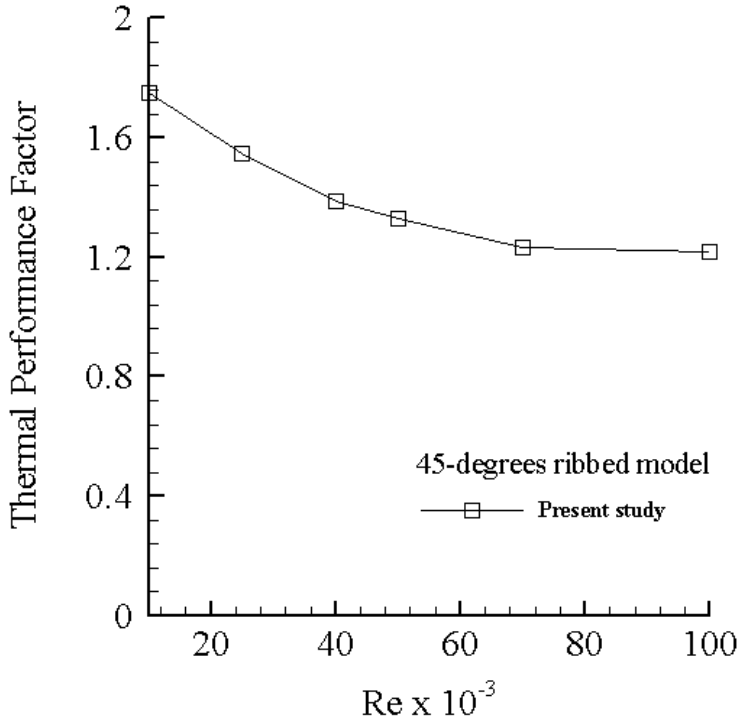

Figure 5.9: Thermal performance factors at Ro=0

5.7 Concluding Remarks

Heat transfer measurements are reported in a rotating rig to examine the effects of rotation number, density ratio, and the buoyancy parameter on the heat transfer characteristics in a two-pass 4:1 AR internal coolant passage with ribs skewed at 45 degrees to the main flow. The results are compared to the data obtained in a 1:1 AR square rotating channel with the same dimensionless rib geometry and reported by Johnson et al. [7]. The following major conclusions are drawn:

1. Rotation effects enhance the heat transfer on the destabilized surfaces of the 4:1 AR channel. This enhancement is stronger on the inlet-trailing wall than on the outlet-leading wall. Rotation effects degrade heat transfer on the stabilized walls, and cause a decrease in Nu/Nu_0 on the inlet-leading and outlet-trailing walls. However, for the lower

Re (Re=10,000), there is an increase in Nu/Nu_0 on the stabilized inlet-leading wall at higher Ro numbers (>0.4).

2. In the range of Ro number covered in the present study (at Re=25,000), the 4:1 AR rectangular channels exhibit similar but weaker rotation effects compared to the results reported by Johnson et al. [7] for a 1:1 AR channel.

3. Higher density ratio enhances heat transfer on all of the four walls in the inlet and in the outlet of the 4:1 AR channels. However the DR effect is considerably weaker compared to that observed for the 1:1 AR channel.

4. Buoyancy parameter (Bo) is observed to correlate the Nu/Nu_0 data reasonably well. This correlation is stronger for the 4:1 AR. The data suggests that the buoyancy effects in the present study are dominated by the centrifugal acceleration due to rotation.

5. The present data for the 45 deg 4:1 AR geometry shows a trend along the inlet leading wall that is in contrast with the 4:1 AR smooth channel where the leading wall heat transfer increased with Ro.

CHAPTER 6

COMPARISONS ON THE THREE MODELS

In Chapter three, Chapter four and Chapter five, the smooth model, 90-deg model and 45-deg model are discussed individually. In this chapter, the results on the three models are placed together and compared to each other.

6.1 Average Nu/Nu_0 in the Stationary Models

Figure 6.1 shows the variations of the channel average (averaged on both leading and trailing walls) Nu/Nu_0 for the three models along with the results of other researchers on the square and 4:1 rectangular channels at different Re numbers.

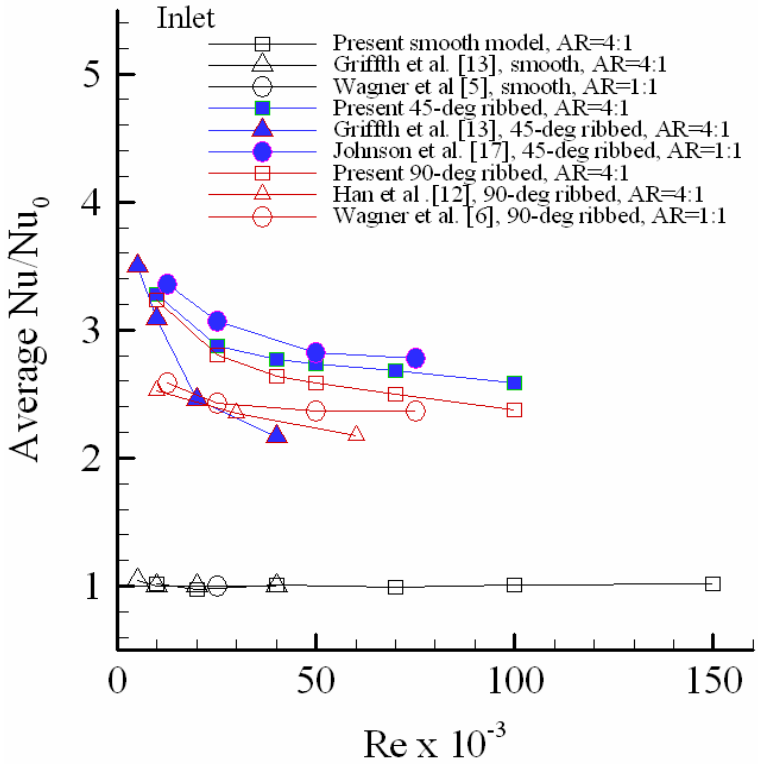

(a) Inlet

Fig. 6.1: Channel average Nu/Nu_0 vs. Re at Ro=0 (Figure continued)

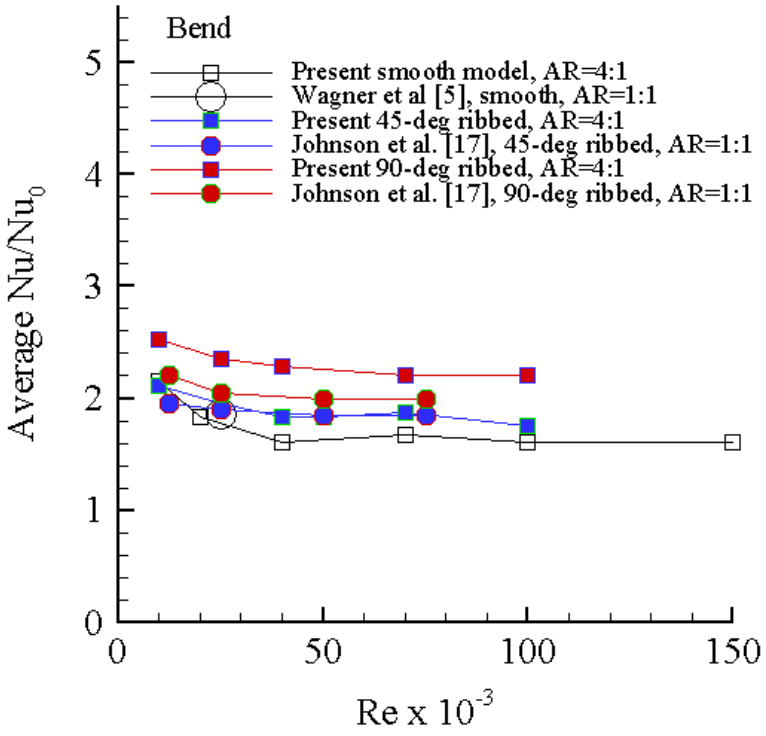

(b) Bend

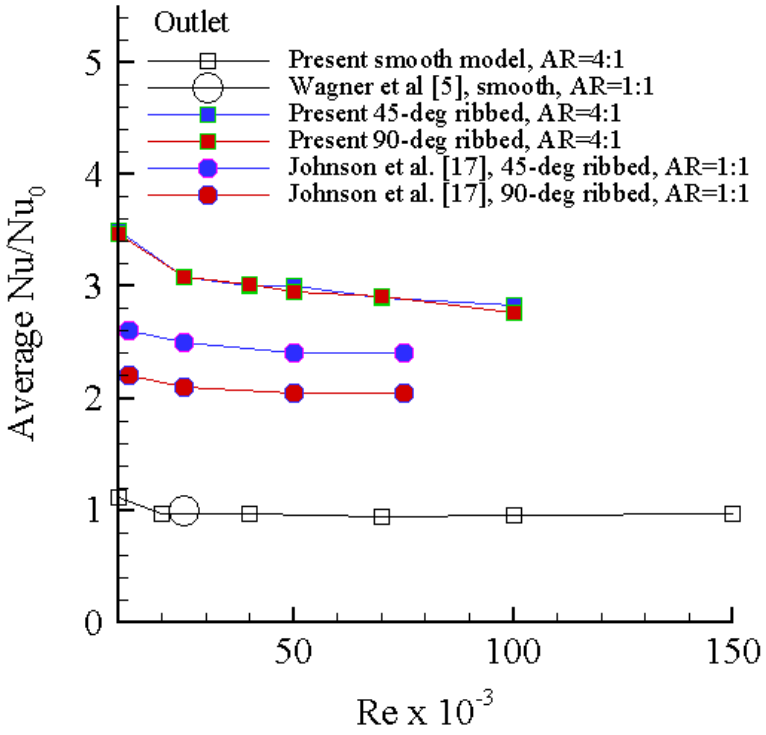

(c) Outlet

For the smooth model, the channel average Nu/Nu_0 is about 1 in the inlet and outlet from Re=10,000 to Re=150, 000, but in the bend area, the channel average Nu/Nu_0 is between 1.6 to 2.2 due to the bend effect.

For the 90-deg ribbed model at Re=10,000 to 100,000, the channel average Nu/Nu_0 decreases from 3.2 to 2.4 in the inlet channel, from 2.5 to 2.2 in the bend, and from 3.5 to 2.8 in the outlet.

For the 45-deg ribbed model, the channel average Nu/Nu_0 decreases from 3.1 to 2.6 in the inlet channel, from 2.1 to 1.7 in the bend, and from 3.5 to 2.9 in the outlet.

It is easy to see that in the ribbed inlet and outlet channels, the ribbed models show higher (2.4 to 3.5 times) heat transfer than the smooth model, and the 45-deg model shows higher heat transfer than the 90-deg model at most of Re numbers in the inlet and outlet. In the bend, the heat transfer in the ribbed models increases slightly than the smooth model, because the bends in the ribbed models are smooth, just like in the smooth model. The slight increase in the heat transfer is due to the higher turbulence generated by the ribbed inlets in the upstream.

6.2 Average Nu/Nu_0 in the Rotating Models

Figure 6.2 and Figure 6.3 show the wall average (averaged on the leading or trailing walls individually) Nu/Nu_0 for the three models when the models are rotating at Re=10,000 and Re=25,000 (Re=20,000 for the smooth model), respectively.

In Figure 6.2, density ratio DR is 0.15, Re number is 10,000, the models are rotating from Ro=0 to Ro=0.62.

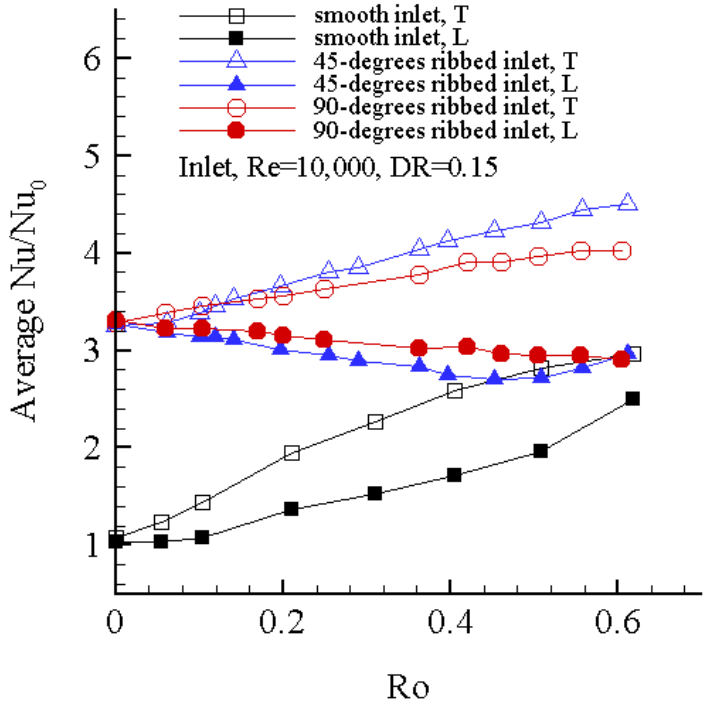

(a) Inlet

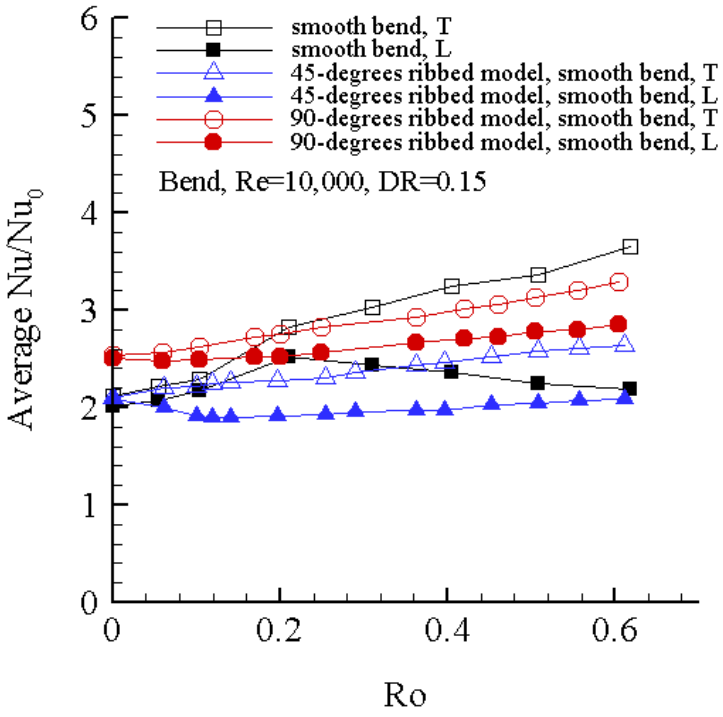

(b) Bend

Figure 6.2: Wall average Nu/Nu_0 vs. Ro at Re=10,000 and DR=0.15 (Figure continued)

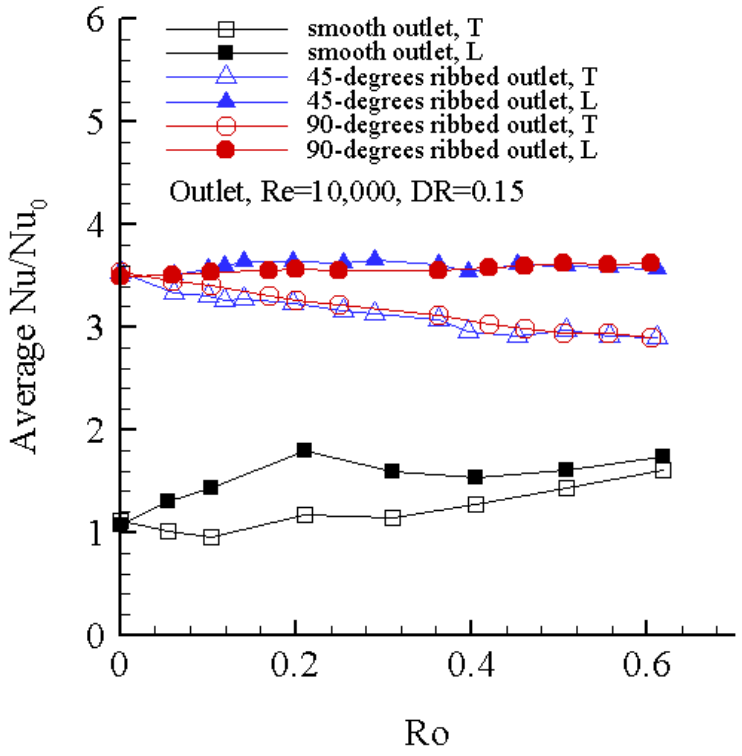

(c) Outlet

In the inlet channels, as shown in Figure 6.2(a), heat transfer on both leading and trailing walls in the smooth inlet increases monotonically from 1 to more than 2 when model rotates from Ro=0 to Ro=0.62. However, in the ribbed models, heat transfer increases with Ro number on the trailing walls, but decreases with Ro on the leading walls (note that Nu/Nu_0 on the 45-deg ribbed leading wall then increases when Ro becomes greater than 0.48). It is apparent in Figure 6.2(a) that the smooth model shows the strongest rotation effect, and the 45-deg model shows stronger rotation effect than the 90-deg model.

The different behaviors of heat transfer varying with Ro number on the inlet-leading walls in the three models seem to be caused by the alteration of near-wall flow

along the channel streamwise direction. On the smooth inlet-leading wall, the near-wall flow is not altered (no ribs on the wall), the wall demonstrates strongest rotation effect on heat transfer, while on inlet-leading wall in the 90-deg ribbed model, the near-wall flow is altered hardest along the streamwise direction by the transverse (90-deg) ribs, the wall displays the weakest rotation effect on heat transfer. But it is not clear how and to what extent the near-wall flow alteration changes the Coriolis force-induced and rotational buoyancy force-induced flow patterns.

In the bend areas, as shown in Figure 6.2(b), the average Nu/Nu_0 on the trailing walls increases with Ro numbers for the three numbers. On the leading walls, the average Nu/Nu_0 demonstrates different behaviors. Compared to the values at stationary (Ro=0), the variation of Nu/Nu_0 on the bend-leading wall with Ro is not significantly.

In the outlet channels, the Nu/Nu_0 behaviors are similar to the inlet. But the rotation effect is weaker for the three models. The two models show almost the same Nu/Nu_0 variations with Ro. On the outlet-leading walls, Nu/Nu_0 almost keeps constant with Ro increasing, while on the outlet-trailing wall, Nu/Nu_0 decreases with Ro for both ribbed models. The smooth model shows similar trends as in the inlet. On both leading and trailing walls, Nu/Nu_0 eventually increases with Ro. But the maximum Nu/Nu_0 is less than 2.

Figure 6.3 provides the wall average Nu/Nu_0 for Re=25,000 (Re=20,000 for the smooth model) with DR=0.15. The results in this group of plots repeat and validate the heat transfer trends with Ro in Fig. 5.2 for Re=10,000, in a smaller range of Ro number.

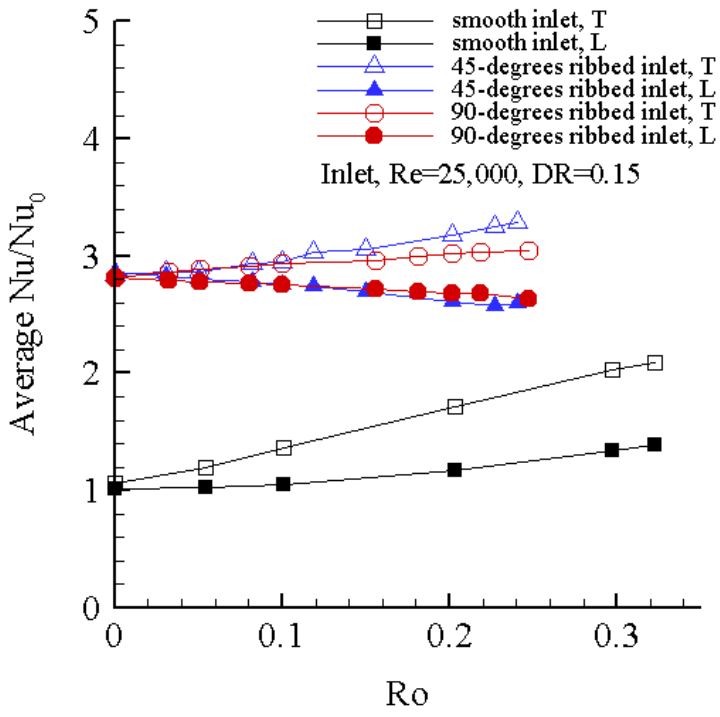

(a) Inlet

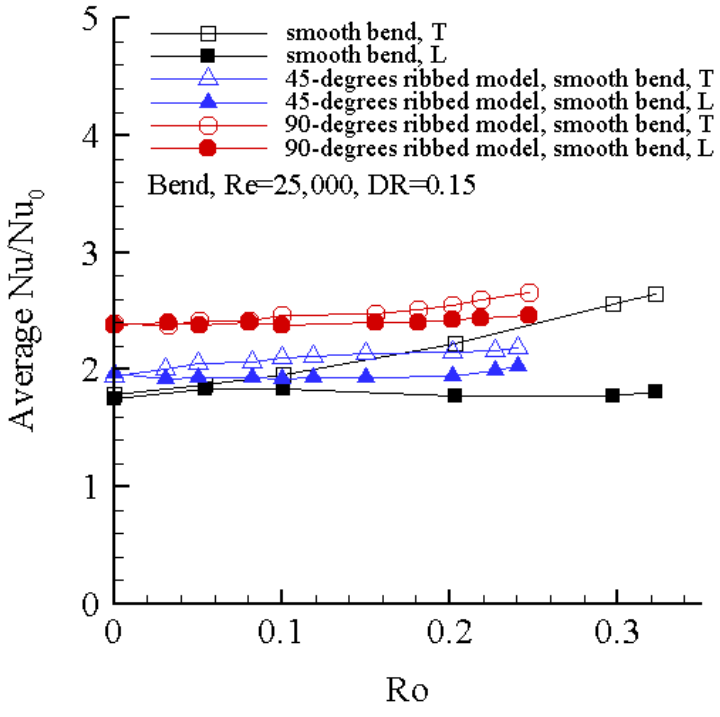

(b) Bend

Figure 6.3: Wall average Nu/Nu_0 vs. Ro at Re=25,000 (Re=20,000 for the smooth model), and DR=0.15 (Figure continued)

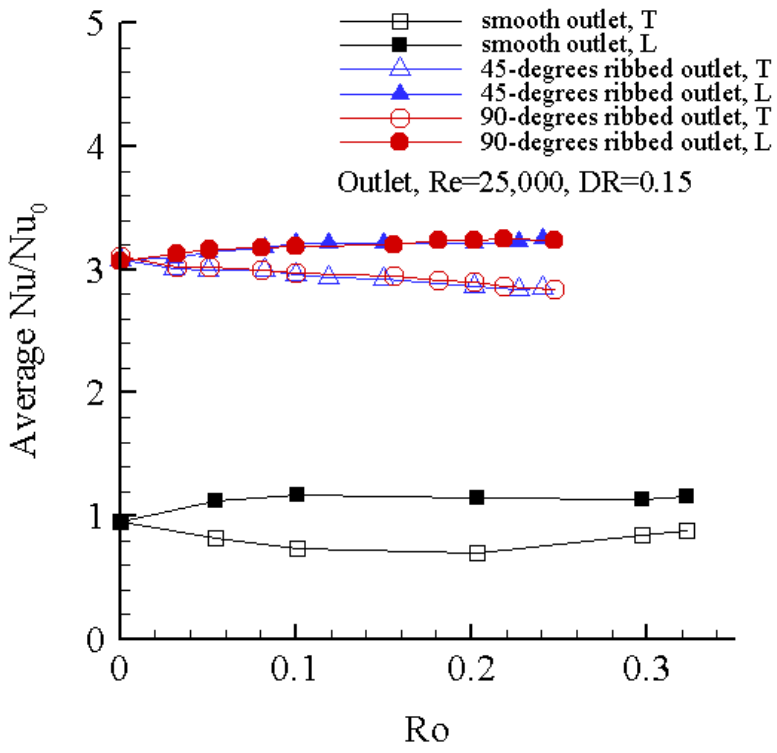

(c) Outlet

6.3 Local Nu/Nu_0 along Streamwise Direction

Figure 6.4 and Figure 6.5 show the local heat transfer distributions along the streamwise locations for Re=10,000 and Re=25,000 at DR=0.15. The results are shown with selected Ro numbers. Note that the bend is located between $11.6 < X/D_h < 18.4$. The inlet channel is in the upstream of the bend ($X/D_h < 11.6$), and the outlet channel is in the downstream of the bend ($X/D_h > 18.4$). In the two groups of plots, the trailing walls are shown at left-hand side, and the leading walls are shown at right-hand side.

In Figure 6.4 and Figure 6.5, the local Nu/Nu_0 value changes with X/D_h even in the same channel of the same model. But at each fixed X/D_h location, the variation of the local heat transfer Nu/Nu_0 with Ro number supports the trends of the wall average properties discussed in the previous section.

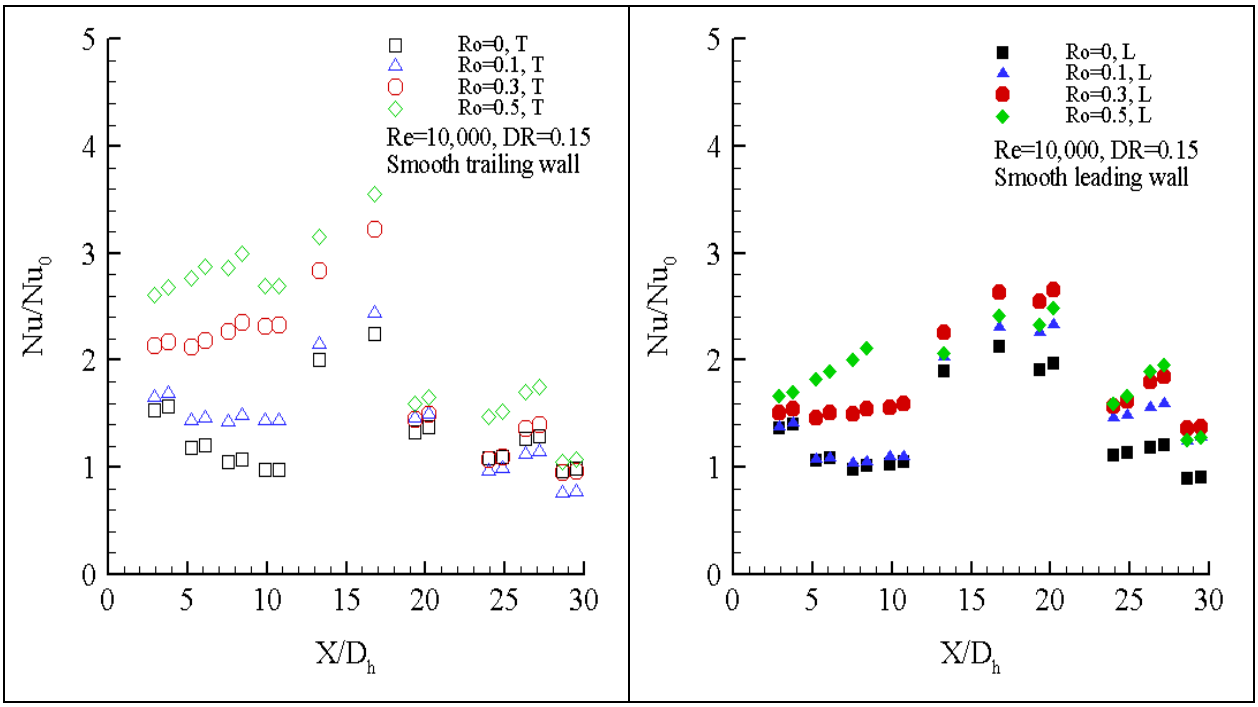

(a) Smooth model

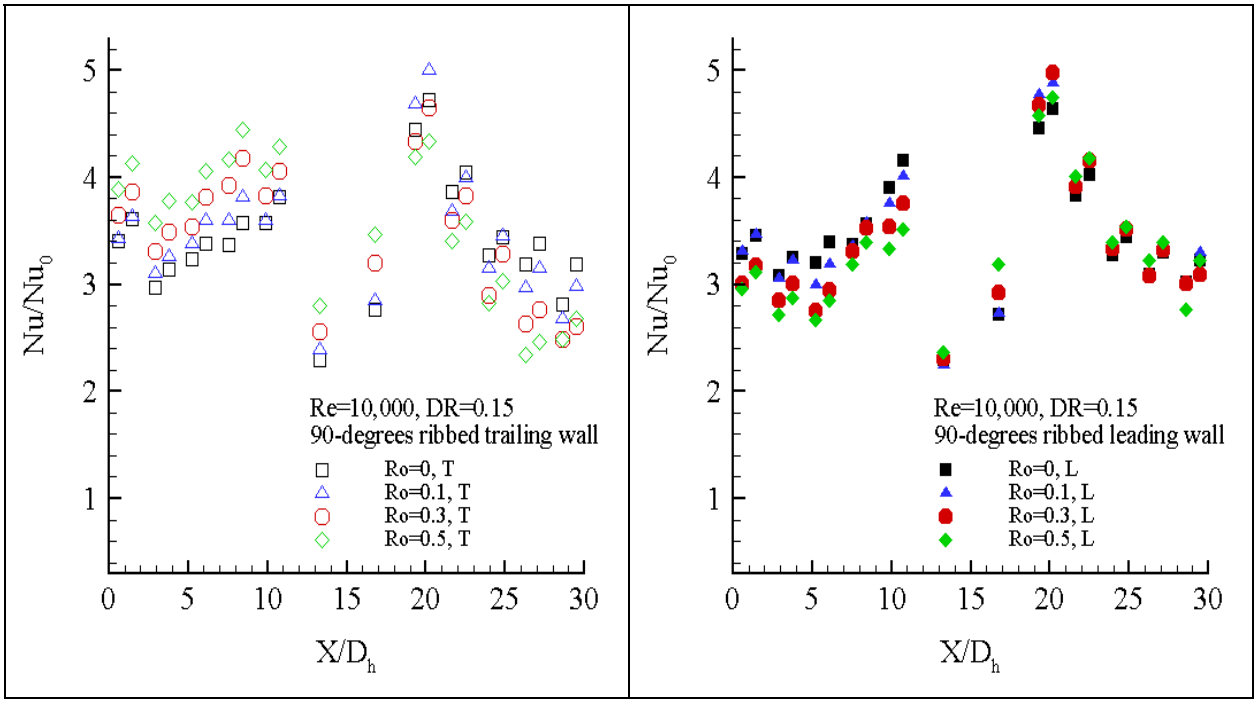

(b) 90-deg ribbed model

Figure 6.4: Nu/Nu0 vs. X/D_h, Re=10,000, DR=0.15 (Figure continued)

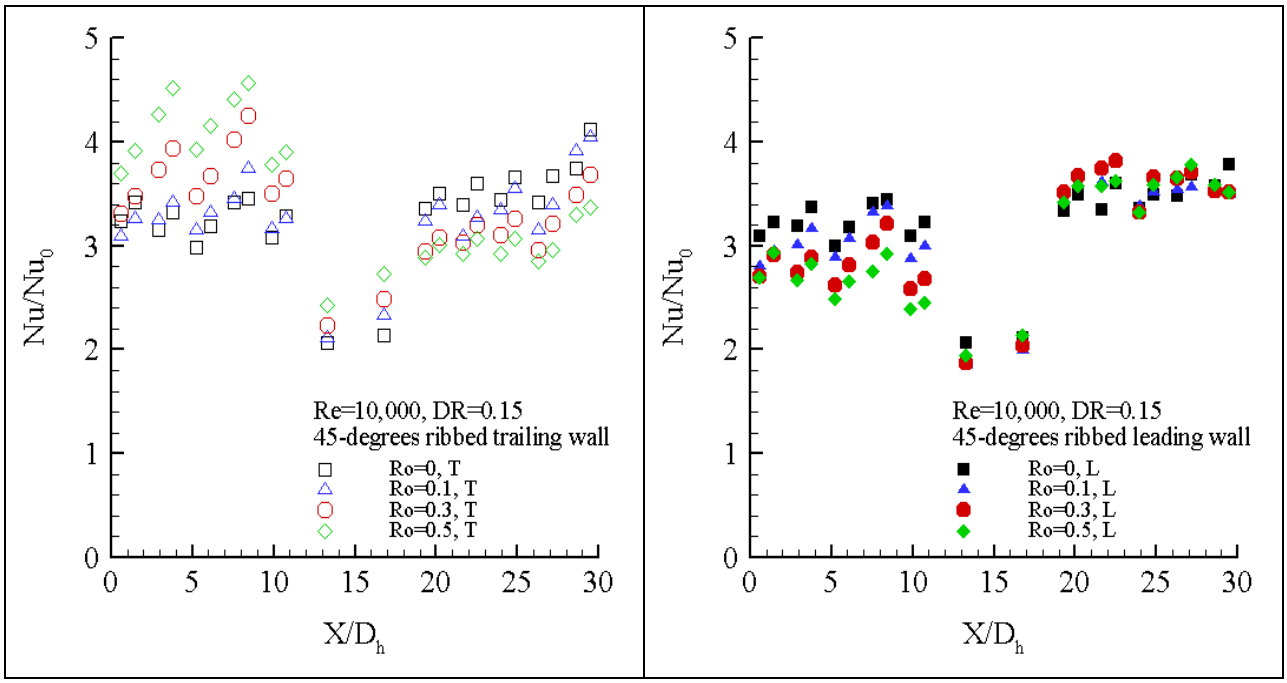

(c) 45-deg ribbed model

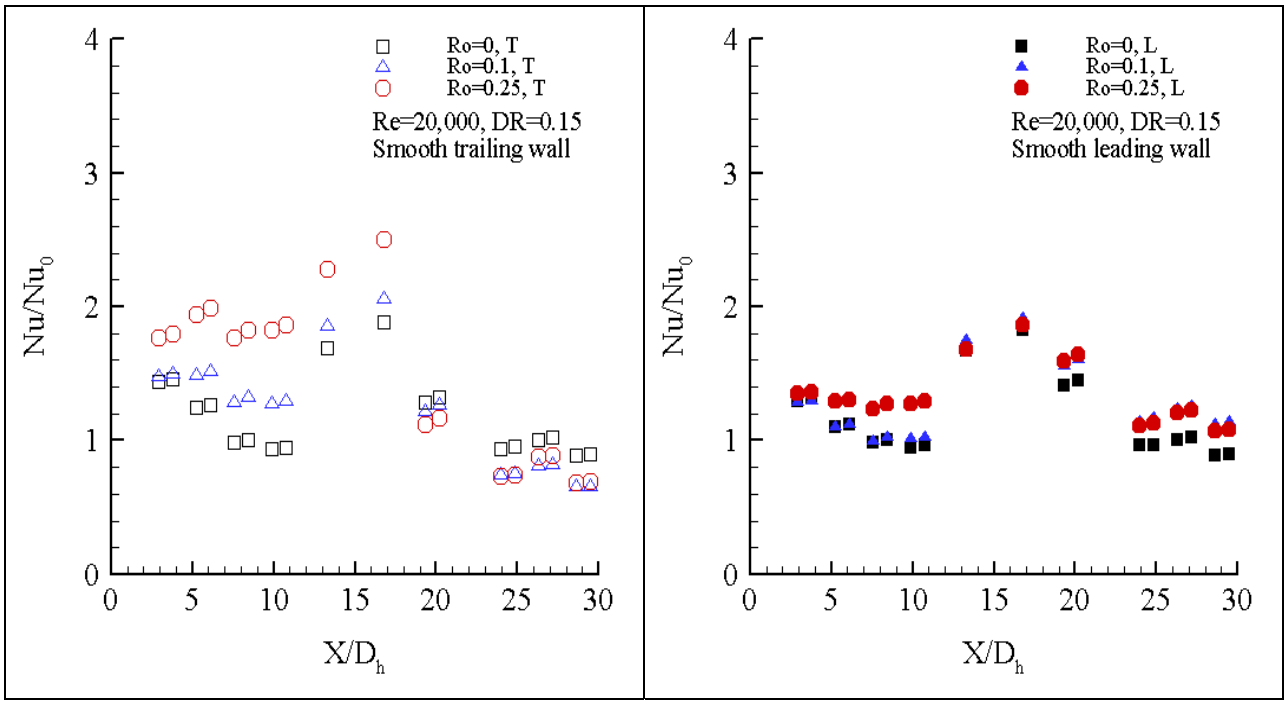

(a) Smooth model

Figure 6.5: Nu/Nu_0 vs. X/D_h, Re=20,000 or 25,000, DR=0.15 (Figure continued)

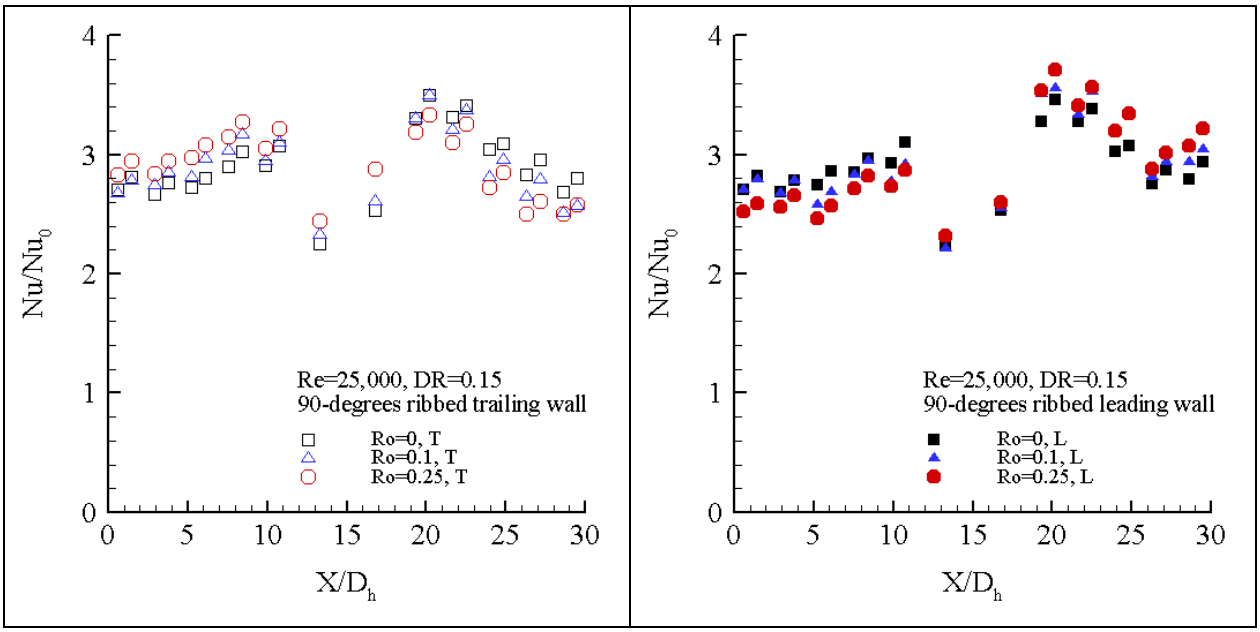

(b) 90-deg ribbed model

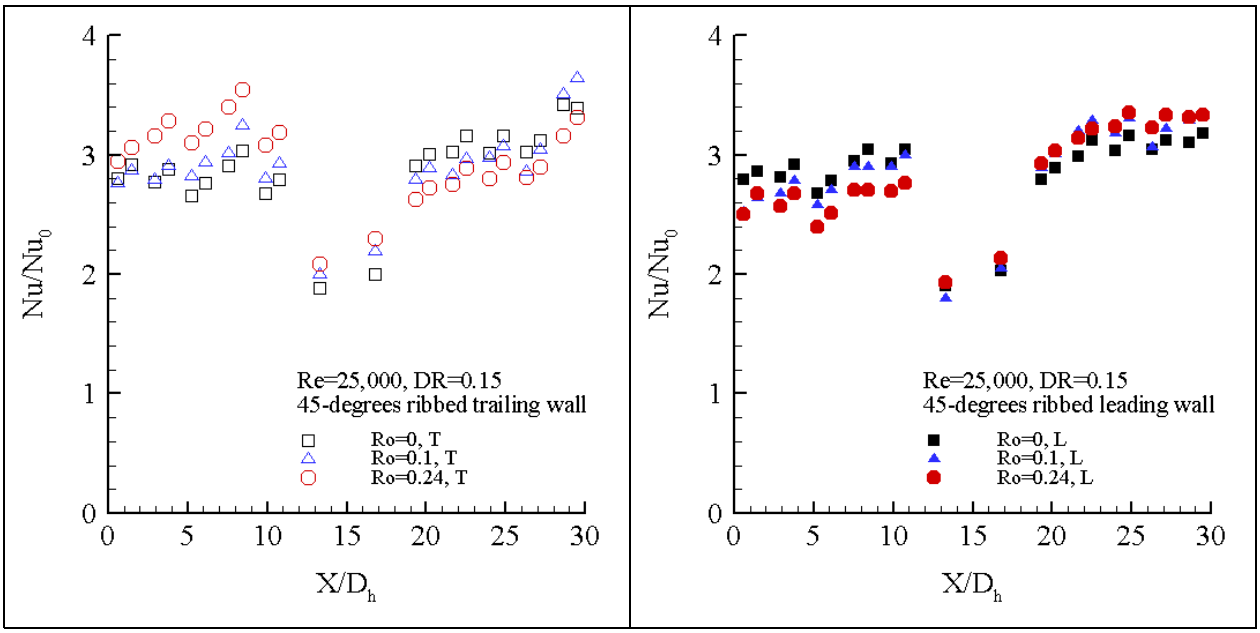

(c) 45-deg ribbed model

6.4 Density Ratio Effects

Figure 6.6 and Figure 6.7 show the variations of the wall average Nu/Nu_0 with Ro number for the three models at three density ratio values of DR=0.10, 0,15 and 0.20.

In Figure 6.6, which is for Re=10,000, the case of DR=0.15 is already discussed in section 6.2. Obviously, the higher density ratio enhances heat transfer for the three models on both leading and trailing walls. At any fixed Ro number, the wall average Nu/Nu_0 at DR=0.20 is greater than or at least equal to that at DR=0.10 and DR=0.15.

It is also evident that the wall average Nu/Nu_0 at DR=0.10 and DR=0.20 follow the same trends as those at DR=0.15 for all of the three models. The three important characteristics are repeatedly validated in Figure 6.6 for the smooth model, 90-deg ribbed model, and the 45-deg ribbed model:

1. The smooth model shows the greatest rotational effect in term of the variation of Nu/Nu_0 from the stationary case. The 45-deg ribbed model shows greater rotational effect than the 90-deg ribbed model

2. In the same model, the inlet channel show greater rotational effect than the outlet channel.

3. The Nu/Nu_0 on the smooth inlet-leading wall increases with Ro monotonically. While on the 90-deg ribbed inlet-leading wall, Nu/Nu_0 decreases monotonically with Ro; and on the 45-deg ribbed inlet-leading wall, Nu/Nu_0 decreases with Ro first, then increases as Ro increases beyond 0.4.

Figure 6.7 shows exactly the same behaviors mentioned above for the ribbed models at Re=25,000 and for the smooth model at Re=20,000.

6.5 Buoyancy Parameter

As discussed in the previous chapters, the rotational effect and density ratio effect can be integrated into a single parameter: buoyancy parameter Bo. Figure 6.8 and Figure 6.9 show the variations of the wall average Nu/Nu_0 with Bo numbers for Re=10,000 and Re=25,000 (Re=20,000 for the smooth model).

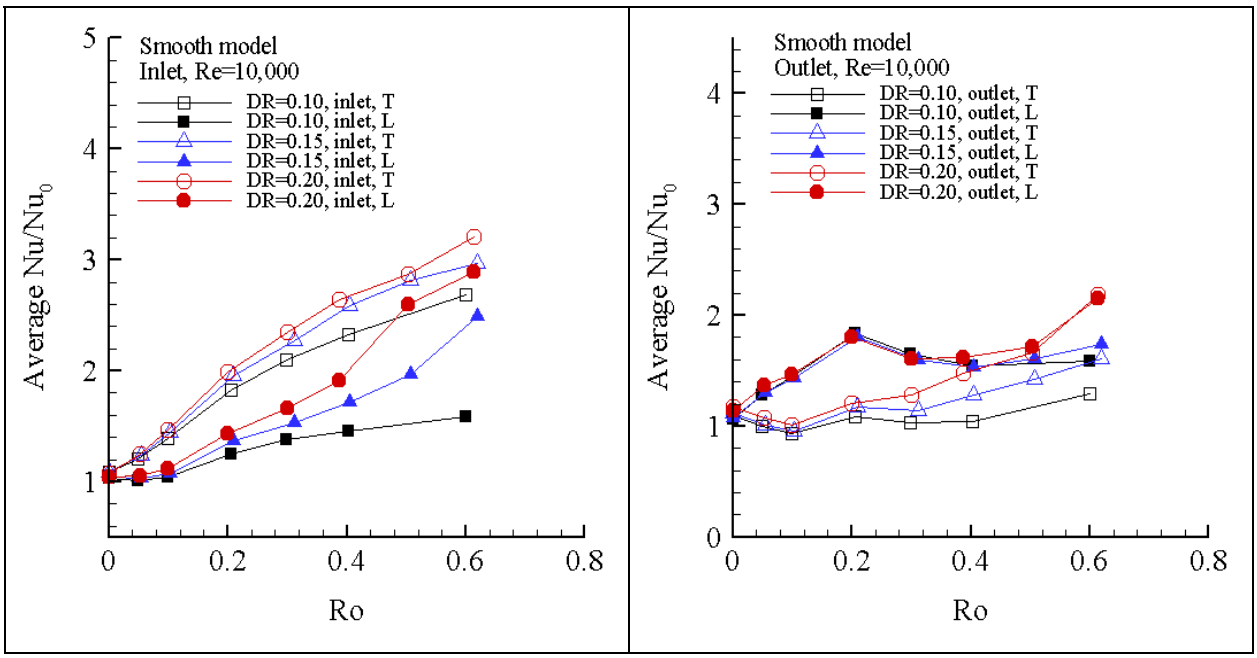

(a) Smooth model

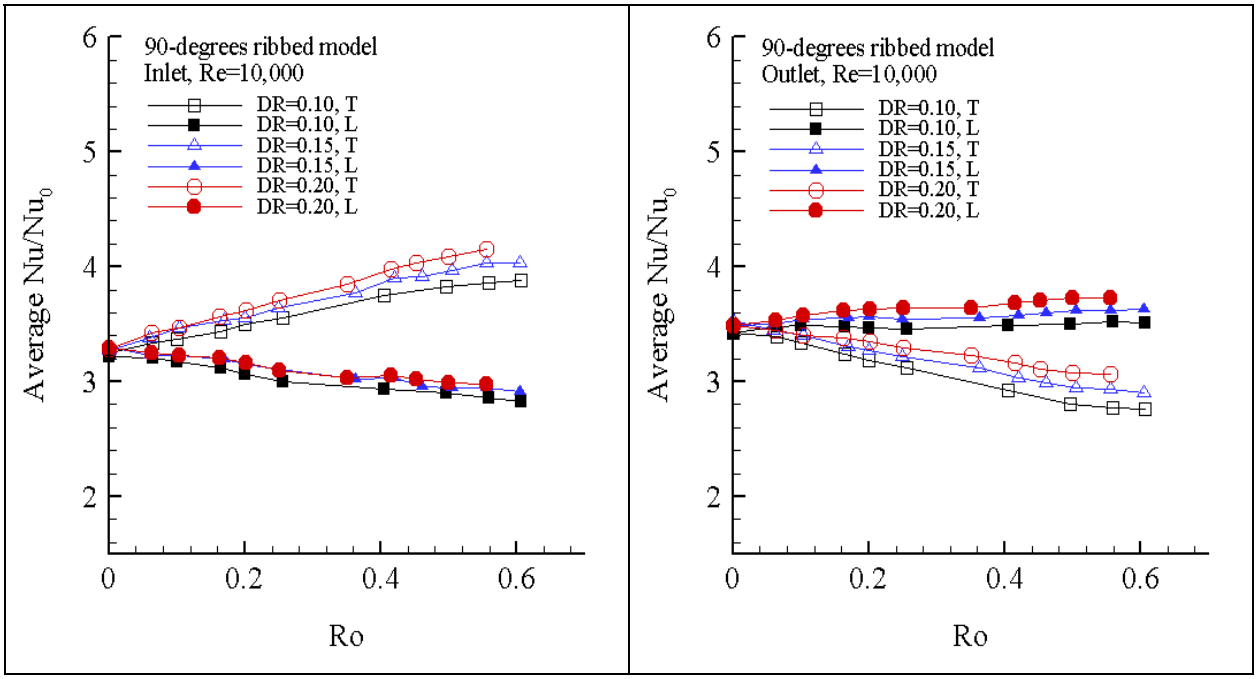

(b) 90-deg ribbed model

Figure 6.6: DR effects (wall average Nu/Nu_0) vs. Ro, Re=10,000 (Figure continued)

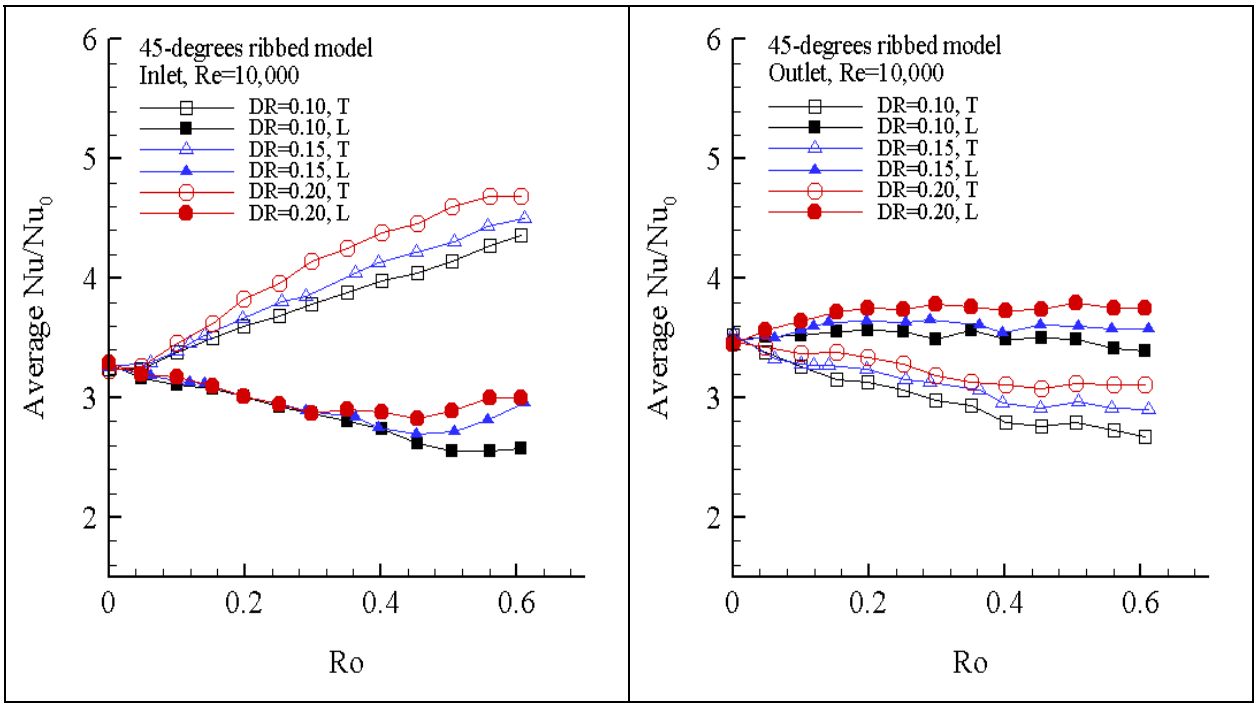

(c) 45-deg ribbed model

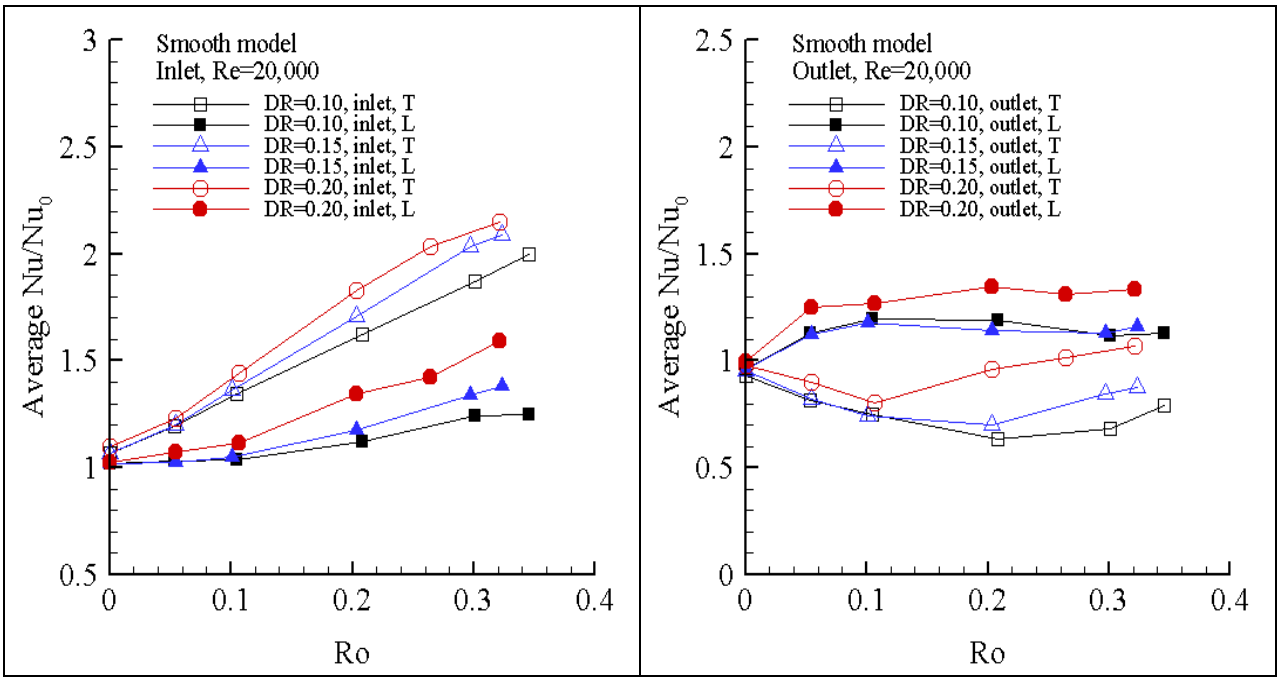

(a) Smooth model

Figure 6.7: DR effects (wall average Nu/Nu_0) vs. Ro, Re=25,000 or 20,000 (Figure continued)

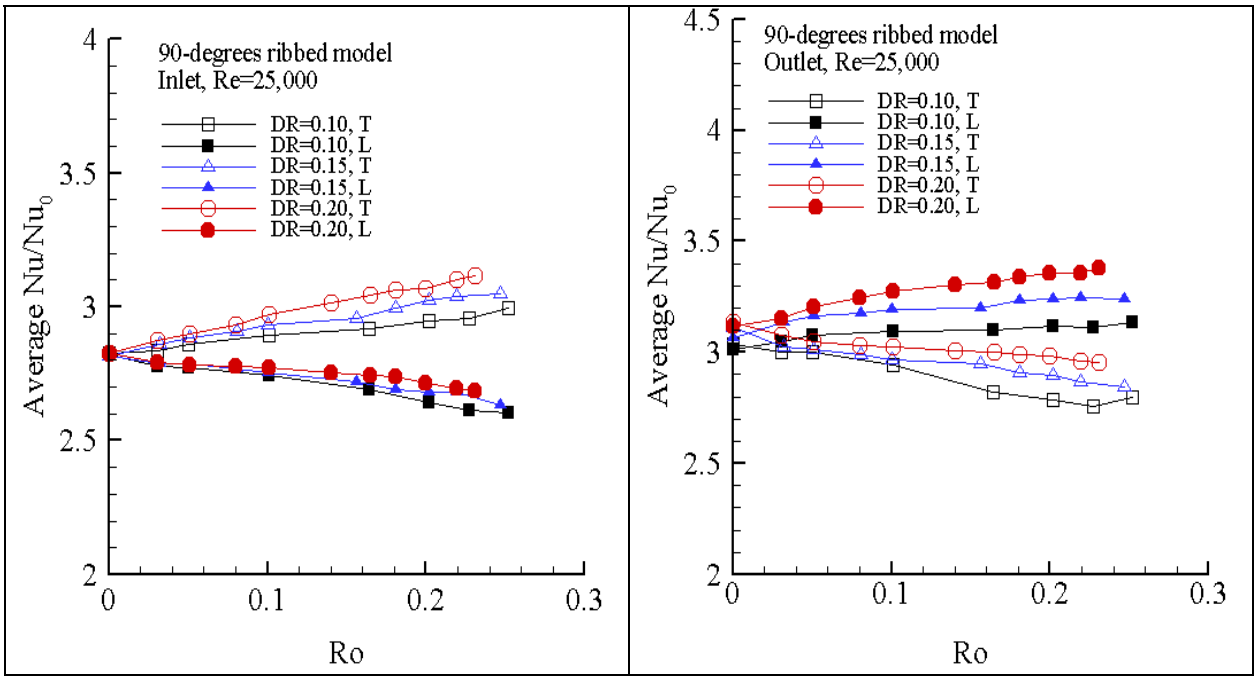

(b) 90-deg ribbed model

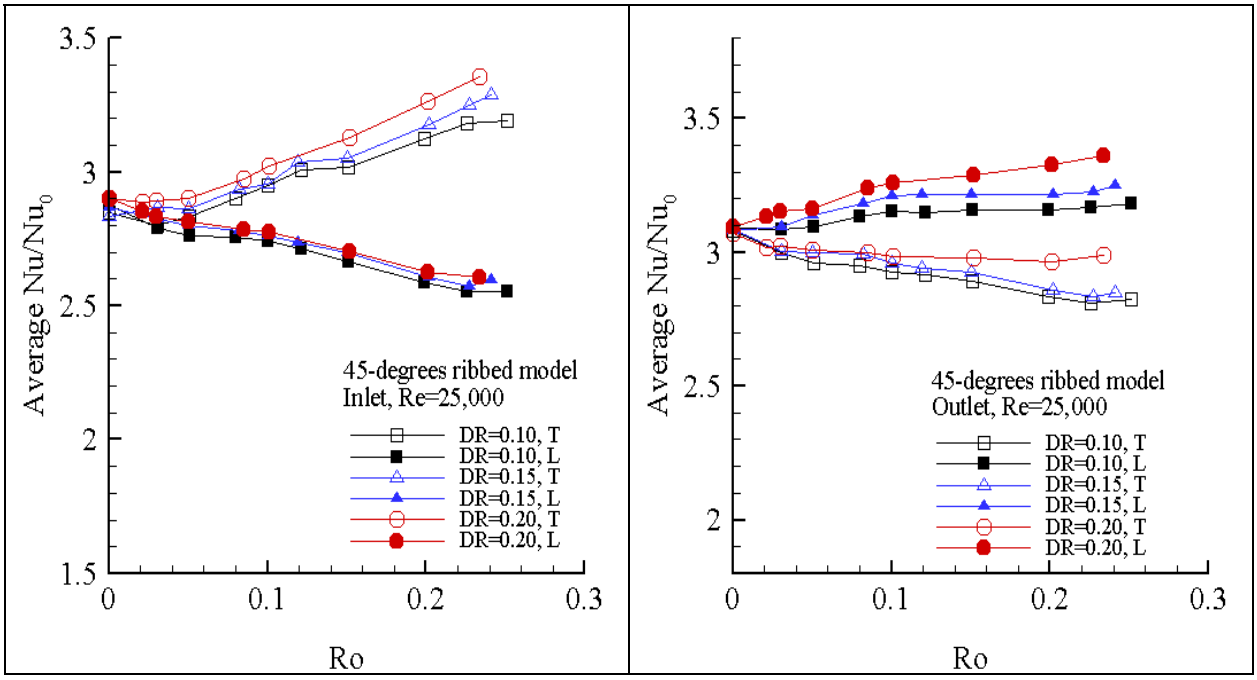

(c) 45-deg ribbed model

From Figure 6.8 and Figure 6.9, the following claims are observed:

The buoyancy parameter Bo collapses the data sets quite well. It works best in the inlet channels for the three models, especially on the inlet-trailing walls.

1. On each wall in all three models, the wall average Nu/Nu_0 eventually increases with Bo number, when Bo increases beyond certain values.

2. In the outlet and in the bend area Bo does not work as well as in the inlet. The bend effect may be the cause: bend alters the flow patterns and enhances the heat transfer, but these effects in nature are not attributed by centrifugal buoyancy.

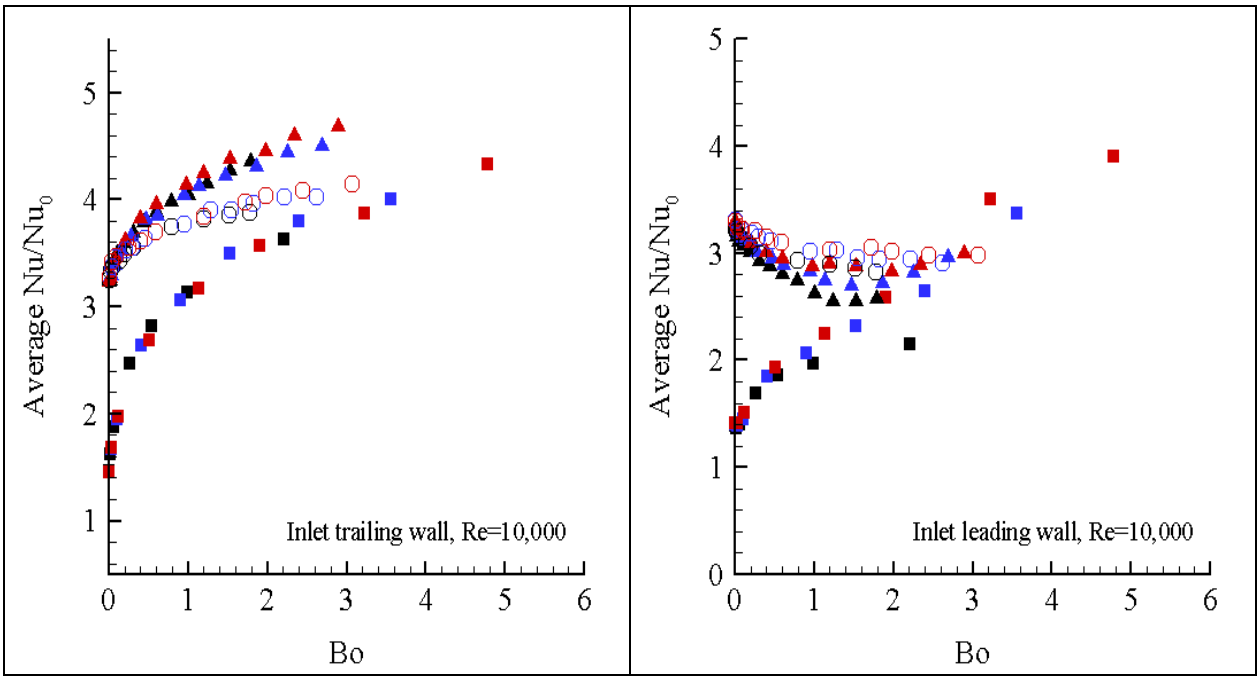

(a) Inlet

(Symbol legend: **square**-smooth model, **triangle**-45-deg ribbed model, **circle**-90-deg ribbed model, **black** color-DR=0.10, **blue** color-DR=0.15, **red** color-DR=0.20)

Figure 6.8: Wall average Nu/Nu0 vs. Bo, Re=10,000 (Figure continued)

6.6 Thermal Performance Factors

Thermal performance factors for the models at stationary are provided in Fig.6.10. Note that the data shown in the plot are only based on the leading and trailing walls. The two smooth side walls are not considered.

It is apparent that the 45-deg ribbed model has higher thermal performance factors than the 90-deg ribbed model. When Re is greater than 60,000, the smooth model shows

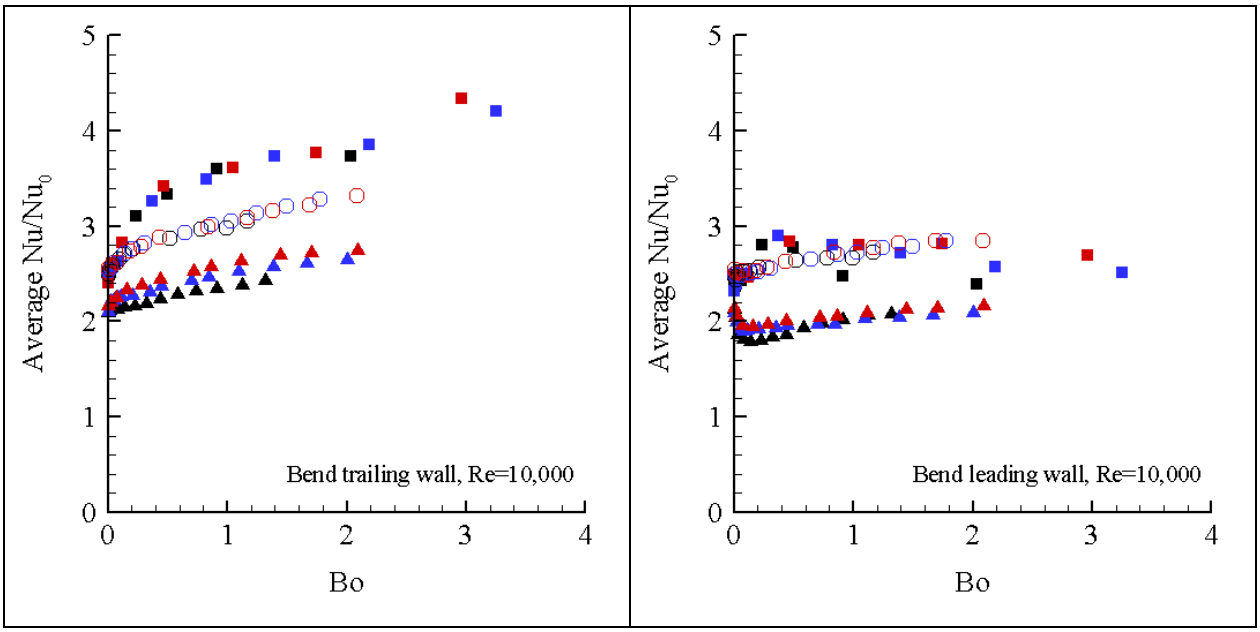

(b) Bend

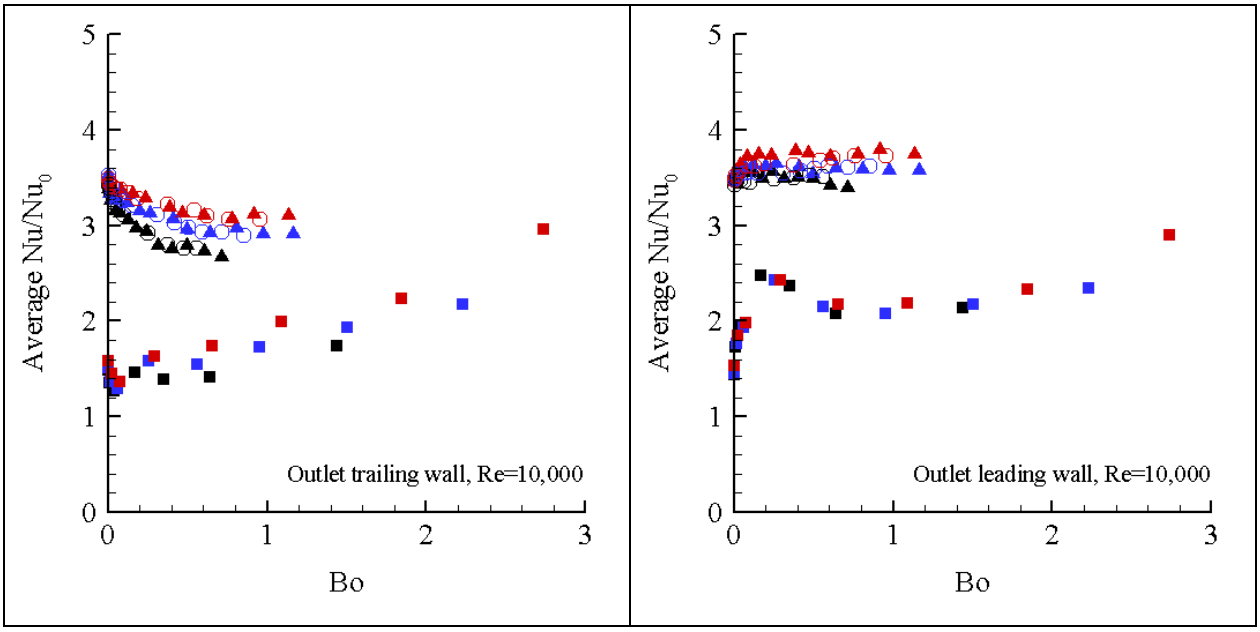

(c) Outlet

the same thermal performance factors as the 45-deg model. This is due to the much low pressure drop in the smooth channel, though the heat transfer in the smooth channel is less than 50% of that in the 45-deg ribbed channel. Thermal performance factors for the

smooth and the 45-deg ribbed models fall between 1.2 and 1.3 as Re number increases, while thermal performance factors for the 90-deg ribbed model can drop to below 1.0.

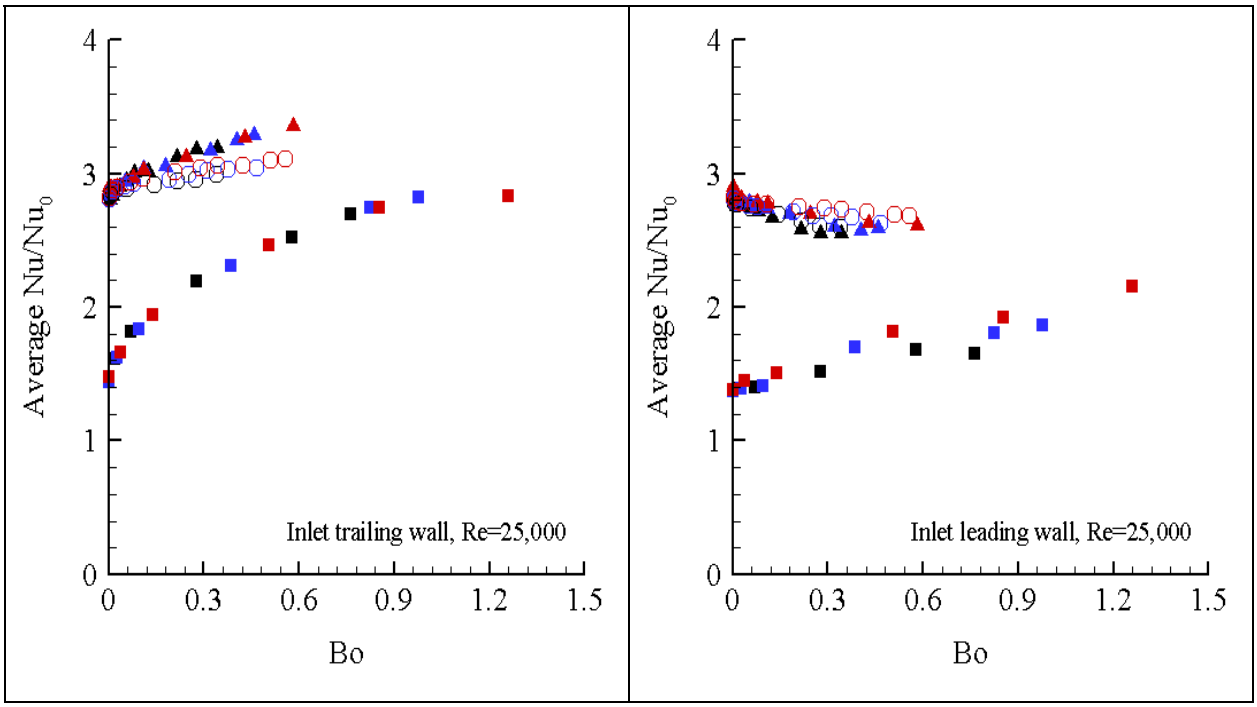

(a) Inlet

(Symbol legend: **square**-smooth model, **triangle**-45-deg ribbed model, **circle**-90-deg ribbed model, **black** color-DR=0.10, **blue** color-DR=0.15, **red** color-DR=0.20)

Figure 6.9: Wall average Nu/Nu0 vs. Bo, Re=25,000 (Re=20,000 for the smooth model. Figure continued)

6.7 Concluding Remarks

Three models with smooth, 90 deg ribbed and 45 deg ribbed channels of aspect ratio 4:1 are compared in this chapter. The following major conclusions are drawn:

1. Ribbed stationary channels show about 3 times of heat transfer ratio compared to the smooth channel.

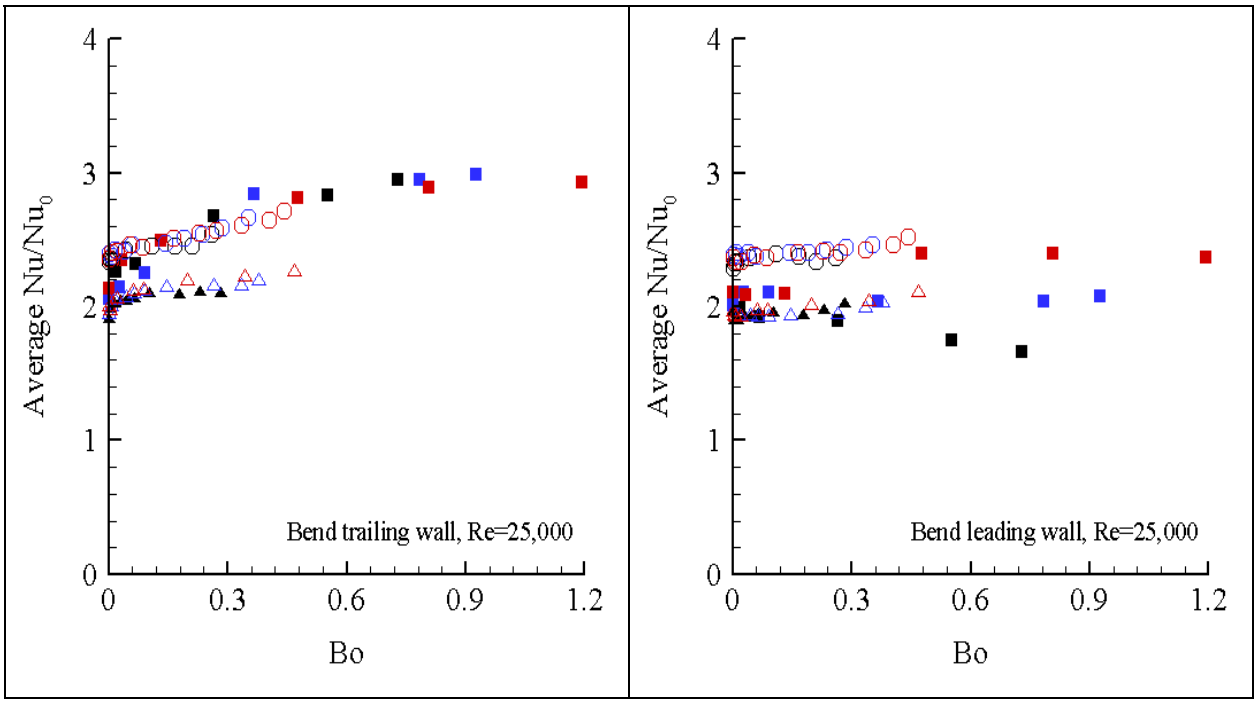

(b) Bend

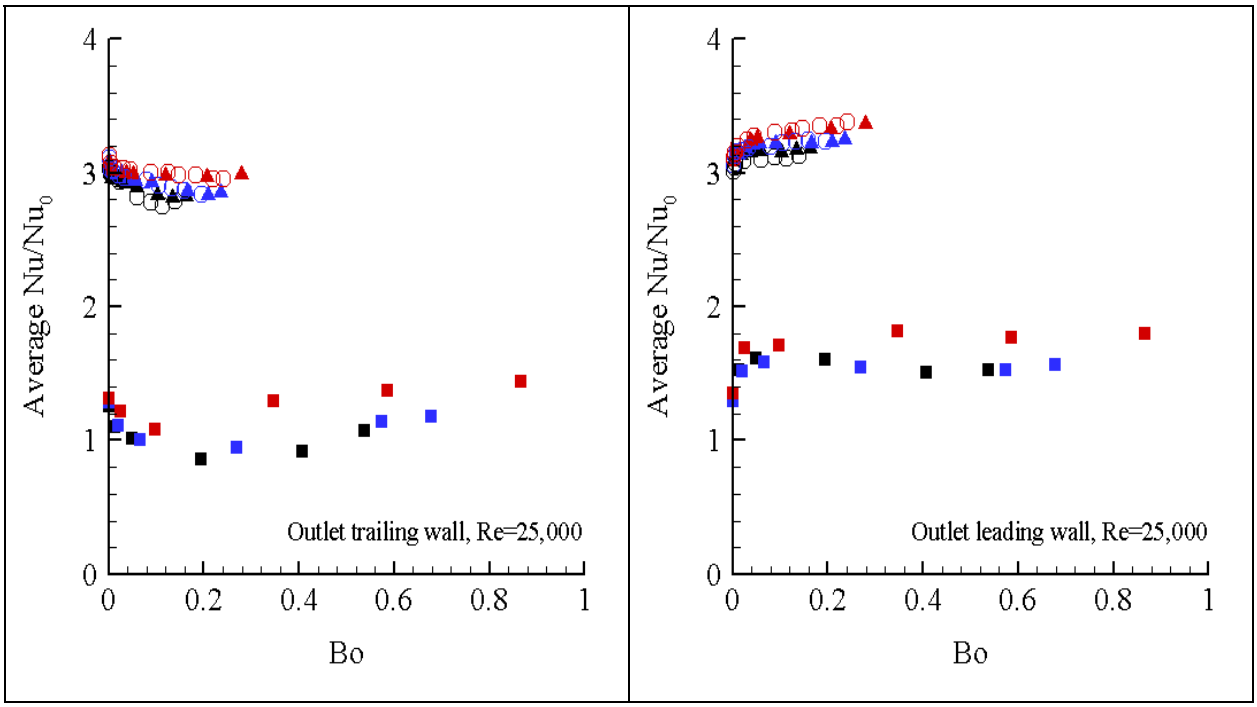

(b) Outlet

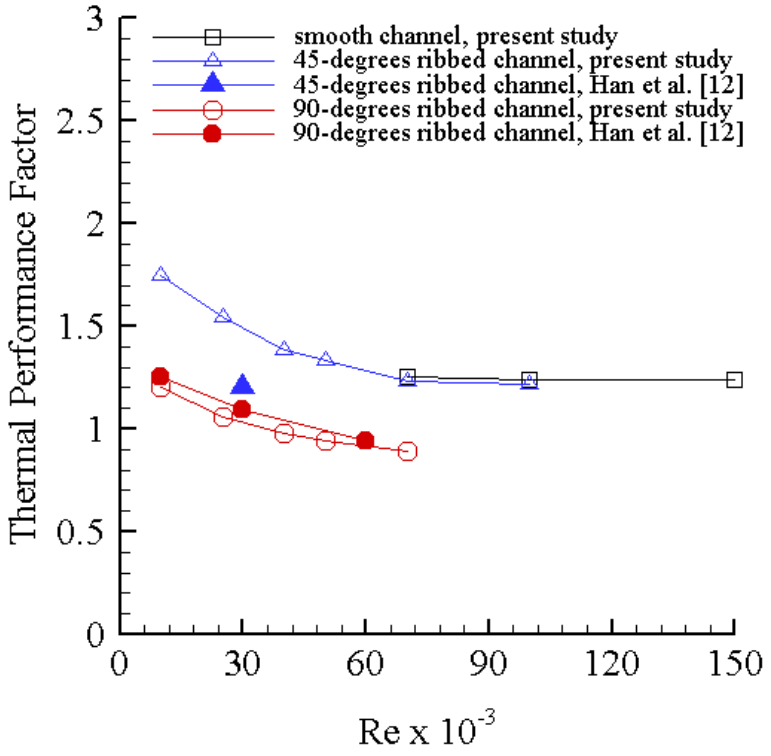

Figure 6.10: Thermal performance factors

2. On the destabilized surfaces (inlet trailing and outlet leading walls), rotation produces a significant enhancement of heat transfer in the inlet of the three models, while in the outlet, this enhancement is almost unnoticeable for the ribbed models.
3. On the stabilized surfaces (inlet leading and outlet trailing walls), rotation reduced heat transfer in both inlet and outlet channels of the two ribbed models, except at high Ro number for 45 deg ribbed inlet-leading wall, where heat transfer increases as Ro reaches to 0.4 and goes beyond. While on the smooth inlet-leading wall, a strong heat transfer enhancement is observed at lower Re numbers (Re=10, 000 and Re=20,000), but this enhancement is not observed at high Re numbers (Re $\geq$40,000) on the same surface. On the smooth outlet-trailing wall, heat transfer enhancement is also noticed at high Ro numbers at Re=10,000 and Re=20,000.

4. In general, smooth channel shows higher rotation effects than the ribbed channels. That is, the heat transfer ratio changes more in the smooth channel compared to the ribbed channels in the same range of Ro number.
5. The three models have the same smooth bend. The heat transfer on the bend does not show significant difference as in the inlet and outlet channels.
6. Higher density ratio DR enhances heat transfer on both leading and trailing walls of the inlet, bend and outlet for the three models.
7. Buoyancy parameter Bo is observed to correlate the Nu/Nu_0 data reasonably well. This correlation is stronger on the inlet-trailing walls,
8. The thermal performance factors (TPF) are calculated for stationary cases. The smooth and 45 deg ribbed models show a TPF about 1.3 when $Re \geq 40{,}000$, while the TPF of the 90 deg ribbed channel drops from 1.2 to less than 1.0 in the range of Re number from 10, 000 to 70,000.

CHAPTER 7

AN INNOVATIVE INTERNAL COOLING TECHNIQUE WITH NEW FINNING STRATEGIES

7.1 Introduction

Heat transfer in internal coolant passages have been studied for about a half century by researchers all over the world. Many cooling techniques have been proposed and tested to enhance the heat transfer between the coolant flow and the wall of the coolant passage. The cooling techniques can be classified into two major categories: the near-wall turbulence intensifying techniques and the core-flow turbulence intensifying techniques.

A variety of near-wall devices, which generate high turbulence intensity in the near wall region, has been investigated in the labs and employed in industrial. These devices include ribs (trip strips) [4-7, 12, 17, 21, 22], pin fins [58, 59], and dimples [46-55, 60]. These near-wall devices work by tripping the boundary layer periodically and inducing repeated flow patterns in the passage leading to high turbulence levels, and by increasing the heat exchange wetted area as well. Ribs have been received the most wide attentions of the researchers and are most commonly used in the air turbine blades. In fact, near-wall turbulence intensifying techniques are typically employed in the situations where the dimension of the internal coolant passage is small, pressure loss is critical and weight is strictly limited, such as in the turbine blades of airplane engines.

In an internal coolant passage, there always is a colder core flow close to the center line of the channel. The difference between the fluid temperature close to the wall

and the fluid temperature along the center line of the passage can be in excess of 100ºK in a big straight passage. If the colder core flow can be diverted towards the heated walls and mixed with the hot near-wall flow, higher heat transfer coefficients could be achieved. The core-flow turbulence intensifying techniques are based on this idea. The theory is fundamentally different from the near-wall devices; it is designed to alter the core flow instead of tripping the boundary layer of the near-wall flow. These techniques are implemented by using special designed flow entry to generate swirl flow or by using helical inserts [61]. Core-flow turbulence intensifying techniques are typically employed in industrial heat exchangers where the dimension of the internal coolant passage is big enough, and pressure loss and extra weight can be tolerated.

The present study attempts to merge the advantages of the near-wall devices into the core-flow turbulence intensifying techniques by attaching elaborately-designed fins onto the passage wall. The fins will force the core flow moving back and forth between the passage walls and the central line of channel, meanwhile the fins will act as near-wall devices in some extent. The goal of the present study is to find a novel technique to promote the heat exchange rate of industrial heat exchangers to a higher level.

In the experimental studies on heat transfer in internal coolant passages, the temperature traditionally is measured with thermocouples. In the past three decades, liquid crystal has become an accurate and commonly accepted tool to record surface temperature. In the present study transient thermochromic liquid crystal (TLC) technique is employed to measure the temperature on the inner walls of the internal channel. TLC was first introduced into heat transfer measurement in 1970s [63, 64], and has been receiving tremendous attentions and improvements since then [65, 66]. Based on the

status of the wall temperature under consideration, TLC methods are classified into two categories: stationary and transient methods. The TLC methods also vary according to the ways interpreting the TLC images to temperature. There are three major approaches to perform the image-temperature correlation: single-color based method for narrow-band TLC [67], hue based [68, 69] and intensity based method [70] for wide band TLC. Ireland et al. [71] presented an overview on TLC techniques covering most important aspects such as the response time; the range of applications and limitations of temperature, pressure, and heat flux; and methods of image processing.

In the discussion that follows, the test model and the fin-geometry, the experimental procedure, and the results will be presented in separate sections.

7.2 Test Models and Test Section

Two models made by a Dimension 3D printer with ABS (Acrylonitrile Butadiene Styrene) plastic material are employed in the tests, which are referred as 30 deg and 45 deg models, respectively. The major features of the 45 deg model are shown in Figure 7.1(a). The model is 10 inches long and 0.815 inches wide. Two rows of fins with an angle of 45 deg to the flow direction are made on the top and bottom surfaces of a thin plate, which is referred as “central plate”. On the top and bottom of the central plate, five short fins and four long fins are located alternatively in equal distance. At the root of each short fin, there are two square through holes (side hole) on each side of the fin. At the base part of each long fin, one rectangular hole (middle hole) with rounded inner corners is made. The model is symmetrical about the horizontal middle plane of the central plate.

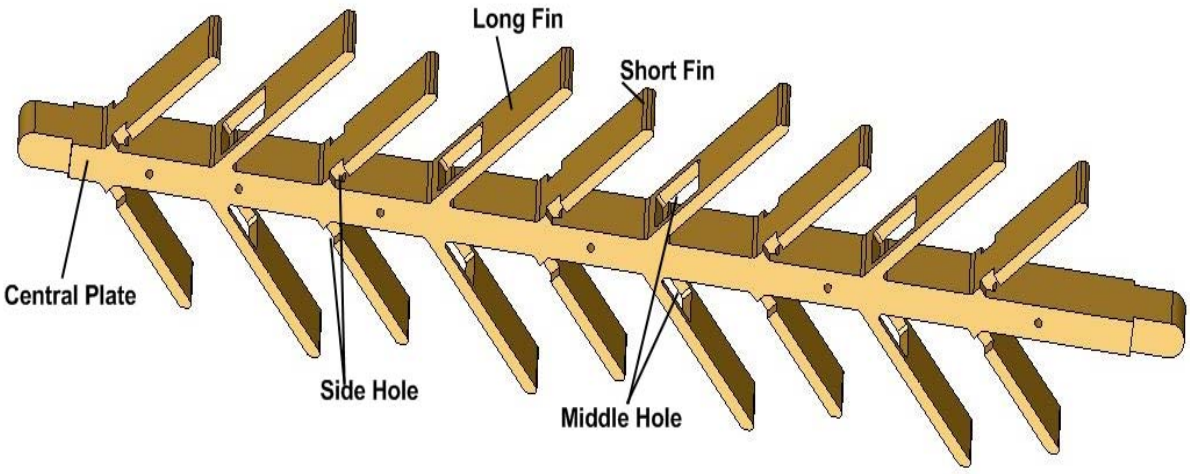

(a) The major features of the model

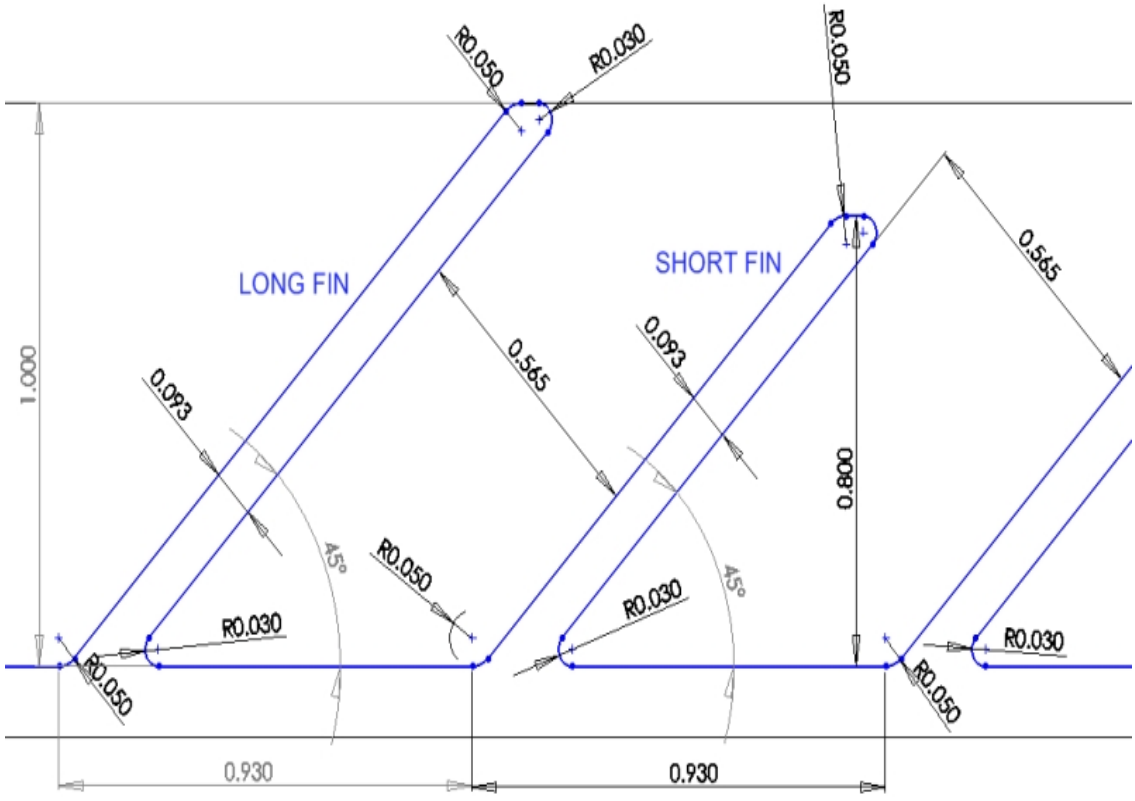

(b) Side view

Figure 7.1: the 45 deg model, cooling air flows from left to right (Figure continued)

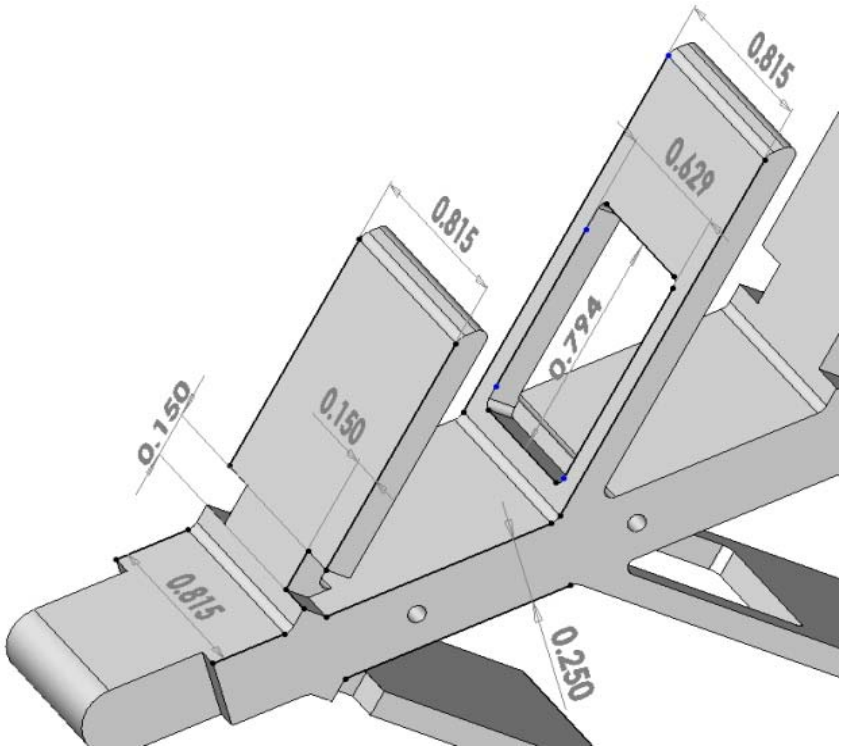

(c) Isometric view

The dimensions of the 45 deg model are shown in Figure 7.1(b) and 7.1(c). The 30 deg model (not shown here to save space) is similar to the 45 deg model. The differences between the two models are listed below:

(1) the angles between the fins and the central plate (or flow direction) are 30 deg in the 30 deg model; (2) the thickness of central plate is reduced from 0.25 inches in the 45 deg model to 0.15 inches in the 30 deg model; (3) the side holes are enlarged from 0.15 inches X 0.15 inches in the 45 deg model to 0.15 inches X 0.55 inches in the 30 deg model, and the middle holes are enlarged from 0.63 inches X 0.79 inches in the 45 deg model to 0.63 inches X 1.12 inches in the 30 deg model; (4) the height (vertical distance from the surface of central plate to the tip of the fin) of the long fins is reduced from 1 inch in the 45 deg model to 0.93 inches in the 30 deg model, and the height of the short

fins is reduced from 0.8 inches to 0.6 inches; (5) the 30 deg model has 5 long fins and 4 short fins on the top or bottom surface.

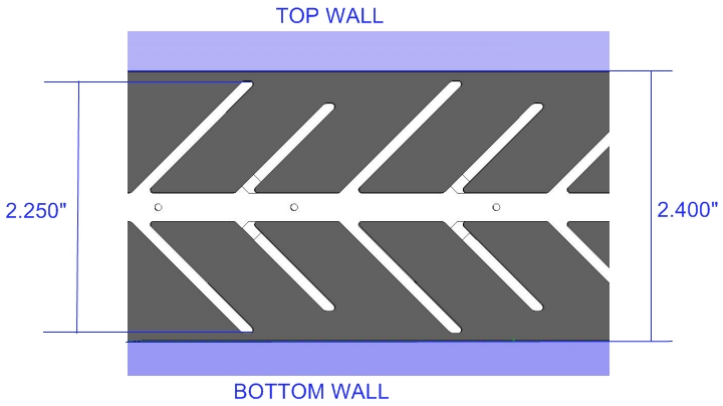

(a)

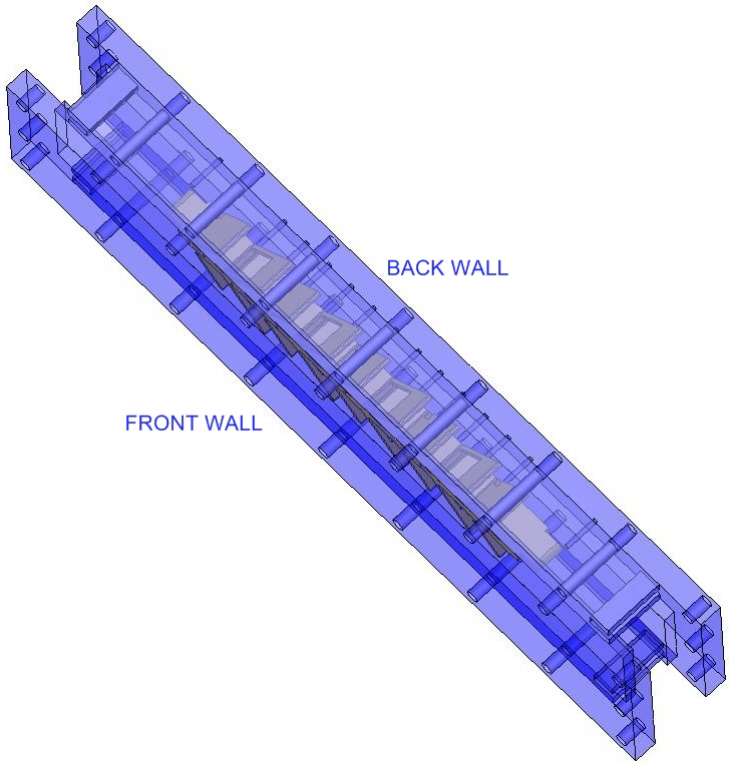

(b)

Figure 2: The 45 deg model in the test section

Figure 7.2 shows the model assembled in the channel of the test section. The channel is formed by four transparent Plexiglas walls (top, bottom, front and back wall) of 16 inches in length. The top and bottom walls are 0.9 inches thick, the front and back

walls are 0.5 inches in thickness. The internal cross-section of the channel is rectangular with a dimension of 2.40 inches X 0.815 inches. Note that the channel and the models have the same width (0.815 inches), so the narrow (vertical) sides of the central plate and the side surfaces of the fins are pressed air-sealed against the front and back walls of the channe1 to simulate the practical applications where the device is supposed to be cast together with the front and back walls of the channel. The model is also pined to the back wall of the test section using the small holes in the central plate shown in Figure 7.1(a) and 7.1(c) to ensure the model aligned accurately with the central line of the channel.

The gap between the tips of the long fins of the 45 deg model and the top/bottom walls of the channel is 0.075 inches, as shown in Figure 7.2(a) with the front wall removed. This gap is 0.16 inches for the case when the 30 deg model is installed. Figure 7.2(b) shows the model in the test section with four walls assembled together.

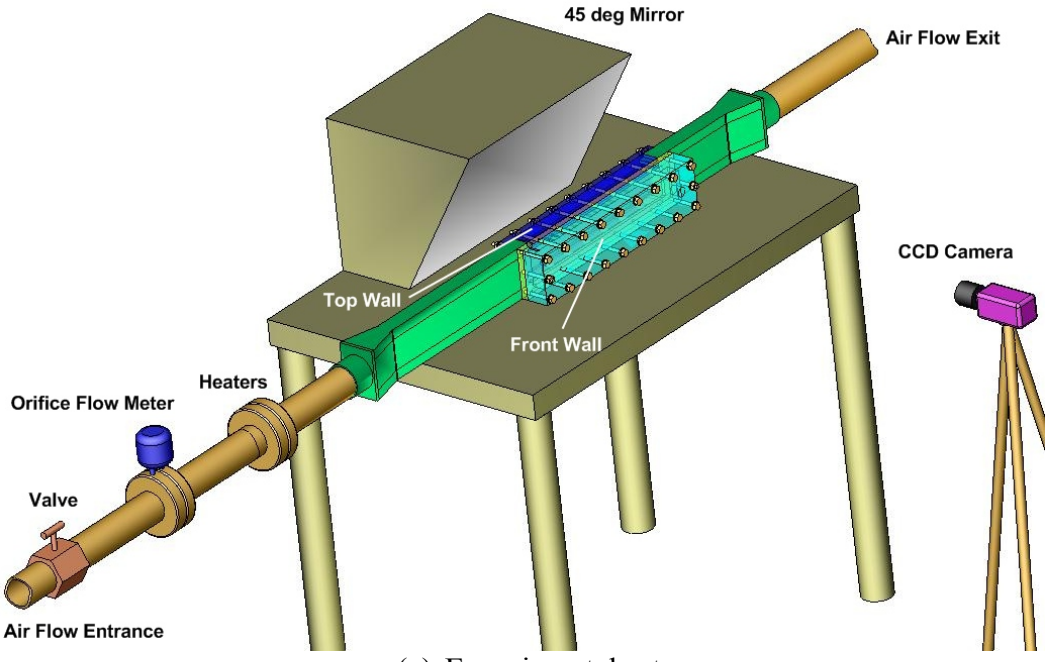

(a) Experimental setup

Figure 7.3: Experimental setup (Figure continued)

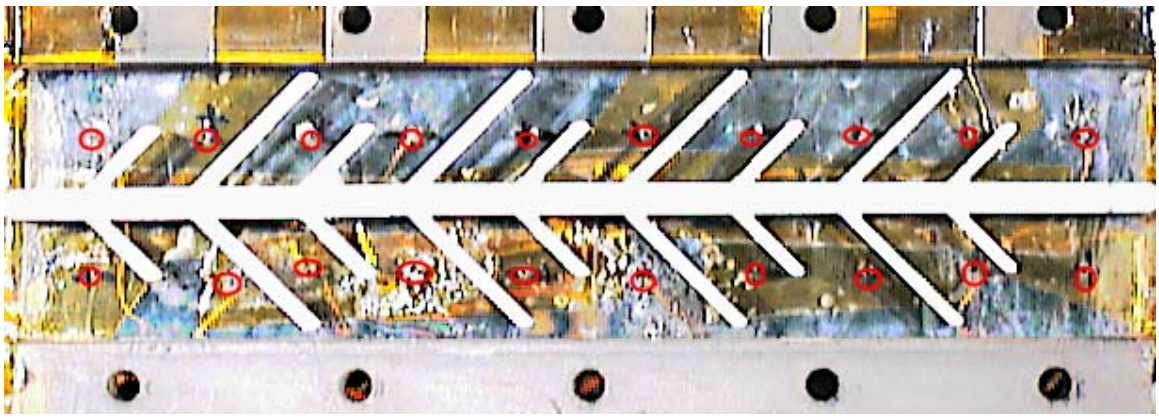

(b) The hole locations in the back wall for measuring the bulk temperature and pressure

7.3 Experimental Setup and Method

(1) Experimental Setup

The experimental setup is shown in Figure 7.3(a) and 7.3(b). The test section is assembled in a 2 inches pipe line and placed on a table. The compressed air enters into the pipe line from the entrance located at the left-hand side of the picture. By adjusting the valve, the expected Re numbers can be obtained. The mass flow rate is measured by using the orifice flow meter. A set of fine mesh heaters is assembled into the pipe line between two flanges in the downstream of the flow meter. The heaters can provide heating power up to 1600W with response time less than 1 second. Then the air flows into the rectangular chamber, which is one foot long, and has the same inner cross-section as the test section. After the flow leaves the test section, it passes a shorter rectangular chamber (0.5 foot long), then the air is discharged into the atmosphere. In the test section, the pressure is slightly higher (0.5 to 6 psig, depending on Reynolds number) than the atmosphere.

On the inner sides of the top wall and the front wall of the test section, a thin layer (0.2 mm) liquid crystal sheet is tightly pressed against the walls with the surface painted with liquid crystal pointing outwards. On the back wall of the test section, ten K-type thermocouples are inserted into the channel through ten holes, which are equally-distributed along the streamwise direction holes on the wall. These ten thermocouples are to measure the bulk temperature of the flow. One thermocouple is embedded on the inner surface at each end of the top wall, and two thermocouples are embedded on the inner surface at each end of the front wall, in order to measure the initial surface temperature. The temperatures on the outer sides of top and front walls are also measured using thermocouples to monitor if the heat transfer penetrates the wall thickness. All thermocouples are then connected to an Agilent 34970A unit (not shown in the picture), and controlled by a customer-made computer program. The local pressure in the test section is also measured through the holes in the back wall by using an Omega HHP-2020 pressure transducer.

A 45-deg mirror is placed above the test section to reflect the images on the top wall to the same plane of the front wall. A Sony XCD color CCD digital camera with IEEE 1394/firewire interface is used to record the liquid crystal images on the front wall and on the top wall simultaneously. The camera is connected to the same computer which measures the temperature using thermocouple, so the time of recording temperature and images can be synchronized.

(2) Experimental Method

In the present study, single-color (green) based, transient TLC method is employed. Hallcrest 1 ºC narrow band liquid crystal sheets are used. The TLC sheet is

black at room temperature, then changes color to orange and red as temperature increases, then turns green at 35.2 ºC, and starts to change green to blue at 36 ºC. It becomes dark blue as temperature continues increasing and eventually turns back to black. As stated above, the bulk temperature of the air flow in the test section are measured using thermocouples while the TLC images are recorded by a Sony color CCD camera. The images are recorded at a speed of four frames per second. To ensure heat transfer will not penetrate the Plexiglas walls, the duration of each test is controlled within 30 to 90 seconds, and the temperatures on the top and front walls are monitored during the tests.

Due to the fact that the bulk temperature in the test channel changes with time, so the Duhamel's superposition theorem is employed to calculate heat transfer coefficient h, as shown in the equation below.

$$T_w - T_i = \sum_{j=1}^{N}\left[\left[1-\exp\left(\frac{h^2\alpha(t-\tau_j)}{k^2}\right)*erfc\left(\frac{h\sqrt{\alpha(t-\tau_j)}}{k}\right)\right]*\left[T_b(j)-T_b(j-1)\right]\right] \quad (1)$$

In the equation, T_i is the uniform initial wall temperature measured by the thermocouples embed at both ends of the wall. T_w is the local wall temperature (35.2 ºC) at the location (x, y) recorded in TLC images when the color starts turning to green. t is the time duration for the location at (x, y) when the temperature increases from T_i to T_w. t varies from location to location. τ_j is the time (defining $\tau_0 = 0$ when wall temperature is T_i , and τ_N = t when wall temperature is T_w =35.2 ºC) when bulk temperature $T_b(j)$ is recorded. Therefore, the heat transfer coefficient h at location (x, y) can be iteratively calculated from the equation, and the heat transfer distributions for the entire walls are available by going through every pixel in the TLC images of the top and front wall.

Nusselts number is then obtained.from heat transfer coefficient h:

$$Nu = h \cdot D_h / k \qquad (2)$$

where D_h is the hydraulic diameter of the test channel or sub channel. Then Nu is normalized by the Dittus-Boelter correlation:

$$Nu_0 = 0.023 \cdot Re^{0.8} \cdot Pr^{0.4} .$$

Thus,

$$Nu/Nu_0 = h \cdot D_h / \left(k \cdot 0.023 \cdot Re^{0.8} \cdot Pr^{0.4}\right) \qquad (3)$$

7.4 Results and Discussion

Tests are done at nominal Reynolds number Re=10000, 20000, 30000 and 40000 based on the hydraulic diameter of the main channel of the test section. Each test is repeated two or three times. Notice that $X/D_h = 0$ is defined at the front tip of the central plate of the models.

(1) Validation tests in the Smooth Channel

To validate the experimental instruments, the test method and the data reduction procedure, a set of tests on the smooth channel (the same channel used later to perform the tests on the models) without test models installed inside is carried out first. Tests are done at four Re numbers from 9,600 to 39,400. Selected results are shown in Figure 7.4 and Figure 7.5.

Figure 7.4 is an original picture taken by the Sony CCD color camera at Re=28,450 and τ=51.5 second The image of the top wall is reflected by the 45 deg mirror into the same frame with the image of the front wall, so the images of the two walls can be recorded simultaneously. In the picture, the air flows from the left to the right side. The green color indicates that the local wall temperature has reached to 35.2 ºC or above, while the black color and orange/red color indicate lower wall temperature areas. The picture clearly shows that lower wall temperature occurs on the downstream part of the

top wall, compared to the front wall at the same streamwise location. This is caused by the narrow cross-section of the channel. The top wall is 1.2 inches away from the central line of the channel, while the front wall is only 0.407 inches away. So the top wall has a thicker velocity boundary layer than the front wall. The lower wall temperature implies lower heat transfer on the top wall in the smooth channel.

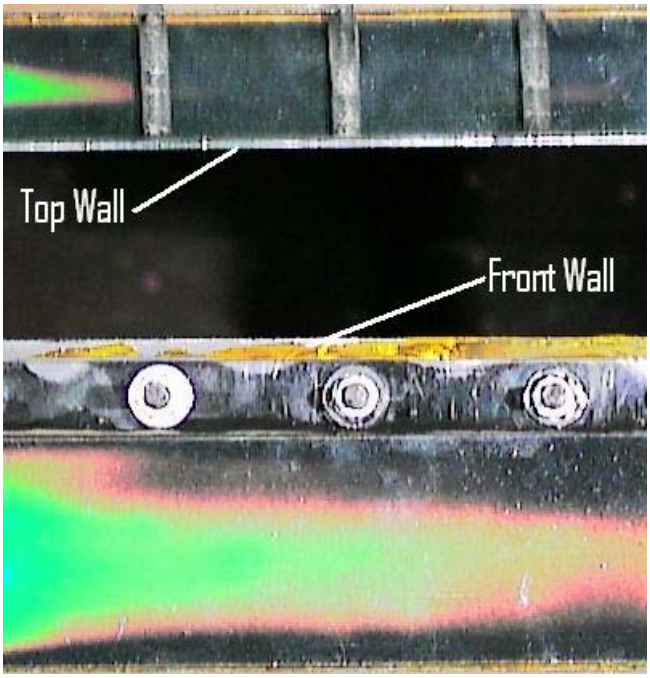

Figure 7.4: Liquid crystal images on the top and front walls in the smooth channel, Re=28,450, τ =51.5 second

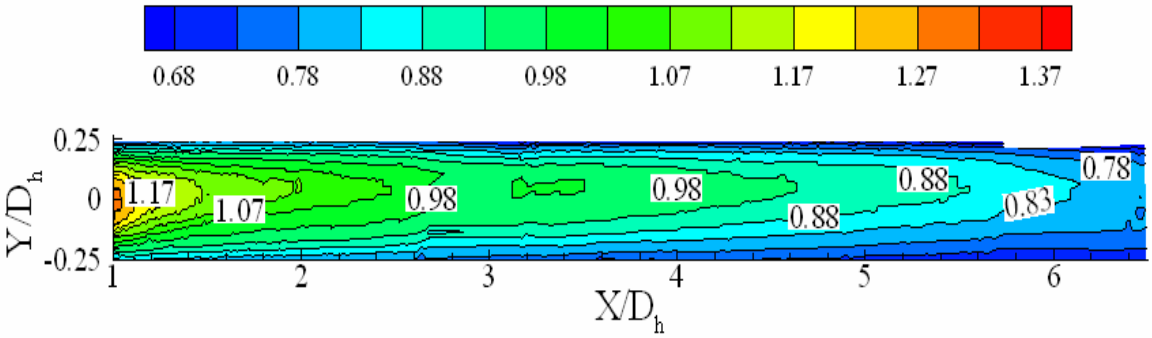

(a) Top wall

Figure 7.5: Nu/Nu_0 on the walls in smooth channel (Figure continued)

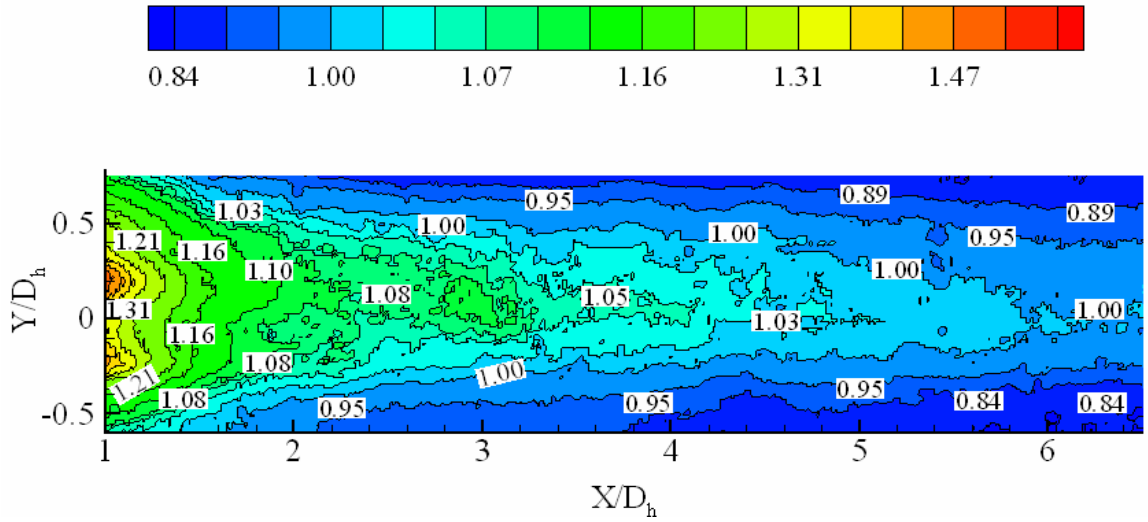

(b) Front wall at Re=28.450

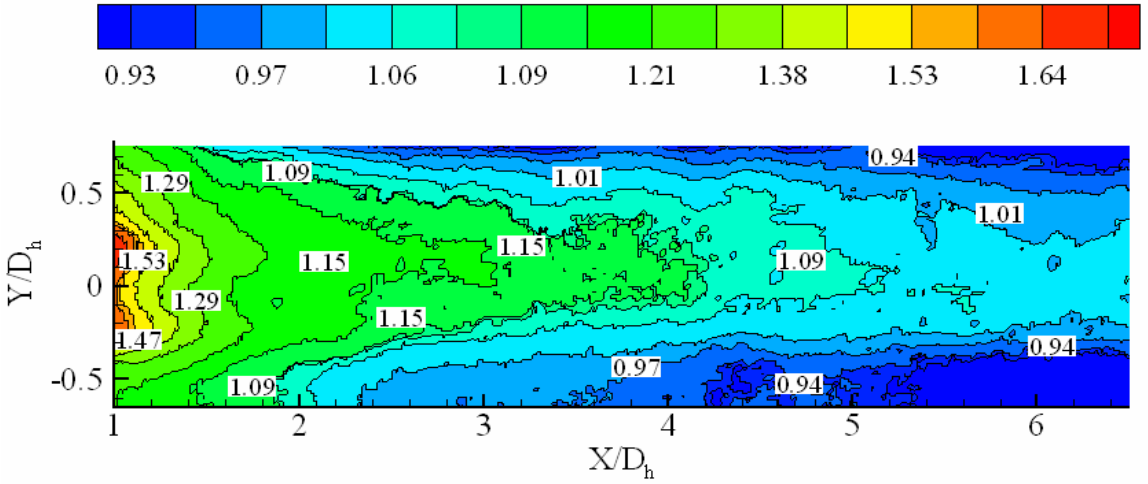

(c) Front wall at Re=18,400

Figure 7.5 shows the Nu/Nu_0 distributions on the top wall (Figure 7.5(a) at Re=28,450) and front walls (Figure 7.5(b) at Re=28,450, and Figure 7.5(c) at Re=18,400). Apparently the Nu/Nu_0 values on the front walls are close to unity. The top wall shows a smaller heat transfer ratio of 0.8 in the downstream area. The pressure data (friction factor) and thermal performance factor (shown and discussed later in "**(3)**

Friction factor and thermal performance") are also comparable with previous published data on the smooth channels.

(2) Heat Transfer with Finned Models in the Channel

When the finned models are installed in the channel in the test section, the channel is equally separated into two sub channels by the central plate of the test model. The aspect ratio (the width of front wall divided by the width of top wall) changes from 2.94 for the main smooth channel to 1.32 when the 45 deg model is installed; and to 1.38 when the 30 deg model is installed. The hydraulic diameter D_h is 1.21 inches for the main smooth channel. D_h changes to 0.93 inches and 0.95 inches when 45 deg and 30 deg model is installed into the channel, respectively. Therefore, Re number and Nu/Nu_0 based on the sub channel changes accordingly. In the sections followed, Re_{sub} and Nu/Nu_0 are based on the hydraulic diameter of the sub channel where the models are installed in the test section, while X/D_h and Y/D_h are always based on the hydraulic diameter (D_h=1.21 inches) of the main channel for geometrical consistency with the smooth main channel.

(a) 45 Deg Model

Figure 7.6 shows an original picture taken at Re=18,900 (Re_{sub}=29,100), and τ =29.5 second when 45 deg model is installed in the channel. On the front wall, the dark strip (low wall temperature area) along the central line is caused by the non-conductive central plate of the model. Notice that in realistic application, the device is supposed to be made of conductive metal, so this low temperature area will not appear, a high temperature area due to the high heat conduction of metallic material will occur instead. It is necessary to point out that in this picture the majority area of the top wall has turned into blue while most part of the front wall is still green. That means the top wall endures

higher wall temperature than the front wall implying higher heat transfer on the top wall. This is shows much clearer in Figure 7.7(a).

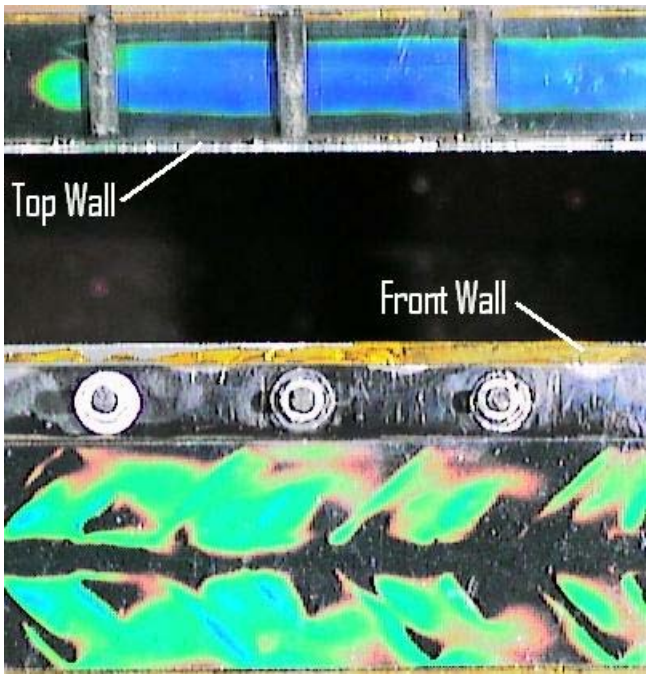

Figure 7.6: Liquid crystal images on the top and front walls with 45 deg model in the channel, Re=18,900 (Re_{sub}=29,100), τ =29.5 second

. In the channel with 45 deg finned model installed, as the flow enters into the channel from the right end, the flow first encounters the short fins (please refer to Figure 7.1(a)) on the top\bottom surface of the central plate, which force the core flow to move upward\downward. The majority of the flow is accelerated due to the blockage of the fins, then passes over the tips of the short fins, and may impinge on the top\bottom walls of the channel if the short fins are close enough to the walls, and then move back toward the central plate. At the same time, a small amount of coolant air is forced to squeeze through the two side holes of each short fin to eliminate the possible dead-flow area behind it.

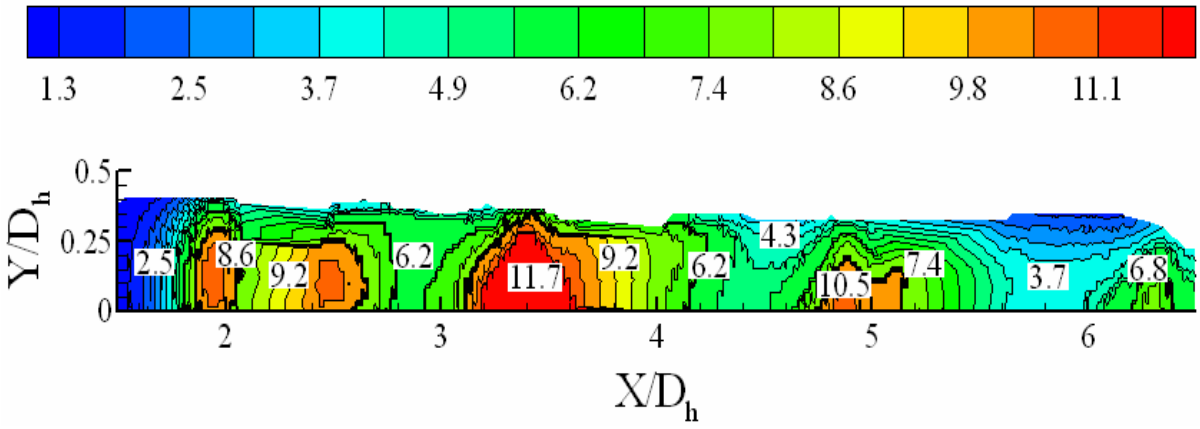

(a) Top wall (Re=10,300, Re_{sub}=15,300)

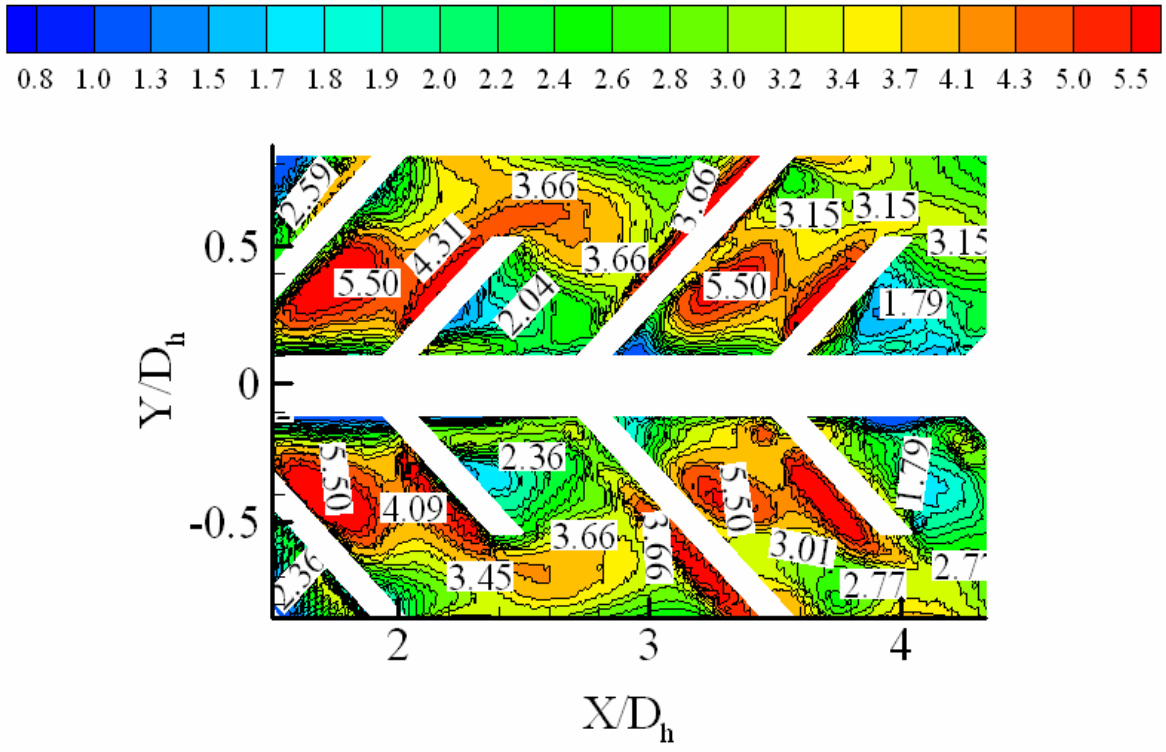

(b) Front wall (Re=10,300, Re_{sub}=15,300)

Figure 7.7: Nu/Nu_0 on the front wall and top walls with 45 deg model in the channel (Figure continued)

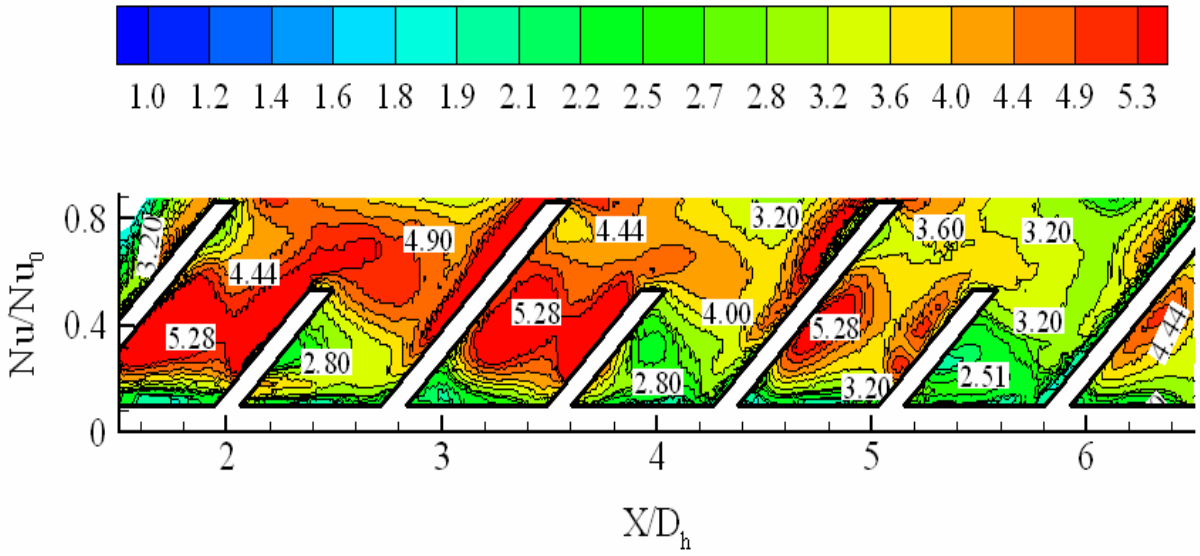

(c) Front wall (Re=18,900, Re_{sub}=29,100)

As the air flows to downstream, the air flow is accelerated again and passes through the middle hole in the long fin. Notice that the two legs of the long fin works as ribs on the front wall and back wall of the channel. Simultaneously, a small amount of air is pushed through the narrow gaps between the tip of the long fin and the top and the bottom walls of the channel. Then the flow repeats the same patterns as it reaches the next short fin.

Figure 7.7(a) shows the Nu/Nu_0 (all Nu/Nu_0 in the cases with models installed in the channel is based on the hydraulic diameter of sub channel) distributions on the top wall at Re_{sub}=15,300. Some local areas show very high heat transfer ratio, for instance, Nu/Nu_0 reaches to 11.7 at X/D_h=3.3 to 3.5. By checking Figure 7.7(b) and 7.7(c), it turns out that this area is right on the top of a long fin. Obviously this high heat transfer area is induced by the strong flow acceleration in the narrow gap (only 0.075 inches, or 1.9 mm in height), and flow impingement on the top wall by the flow runs upwards along the

surface of the long fin. This speculation is confirmed at X/D_h=2.0, 4.9 and 6.4 in the same Figure by observing high Nu/Nu_0 at these streamwise locations. It is also observed at other Reynolds numbers for the 45 deg model (not shown in this paper).

Figure 7.7(b) and 7.7(c) show Nu/Nu_0 distributions on the front walls. Figure 7.7(b) shows good symmetry of Nu/Nu_0 induced by the top row and bottom row of fins. So for clarity, only upper half of the front wall will be shown in the section followed. The most conspicuous fact on the front wall is that the legs of the long fins are found to act as ribs: The legs enhance flow turbulence, and generate higher Nu/Nu_0 in the immediate downstream area of each leg. In Figure 7.7(b) and 7.7(c), the local Nu/Nu_0 in the downstream areas adjacent to the legs of long fins reaches to above 5. The second heat transfer enhancement is found in narrow areas along the upper partial of the short fins and in the areas over the tips of short fins. This is caused by the flow impingement on the short fin surface by the flow passing through the middle hole of the upstream long fin, and caused by the strong mixing with the flow which passes through the narrow gap between the tip of the long fin and the top/bottom wall in that area. On majority area of the front wall, Nu/Nu_0 reaches to 3 or more.

(b) 30 Deg Model

In Figure 7.8, an original TLC picture is shown when the 30 deg finned model is installed in the test channel at Re=29,300 (Re_{sub}=43,400) and τ =30.75 second. This picture is similar to Figure 7.6 except one thing: the temperature on the top wall is lower compared to the front wall. This is reasonable by recalling the fact that the gap between the tip of the long fin and the top wall is widen to 0.16 inches (4.06 mm) when the 30 deg model is installed in the channel, so the acceleration effect is weakened. Figure 7.9(a)

shows the Nu/Nu_0 contours on the top wall. Notice that the Nu/Nu_0 on the top wall is almost equivalent to the smooth channel in the upper stream, while on the downstream part Nu/Nu_0 increases as flow turbulence is intensified by the fins.

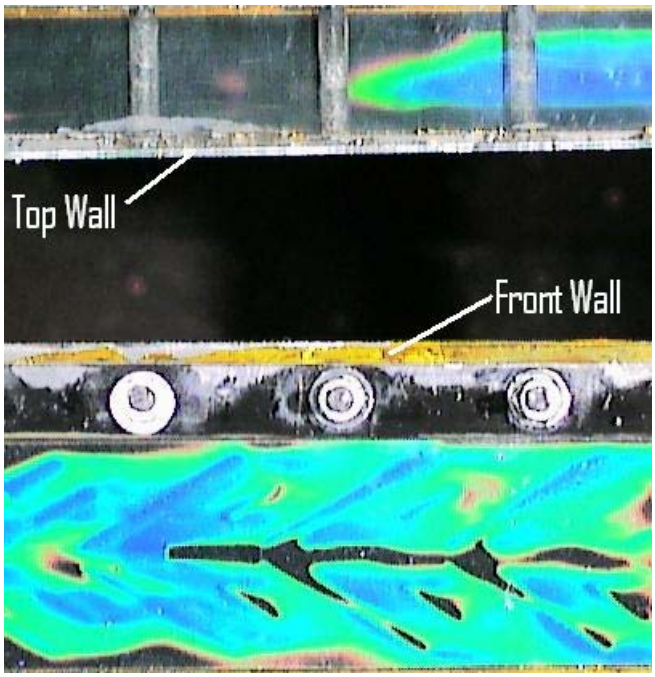

Figure 7.8: Liquid crystal images on the top and front walls with 30 deg model in the channel, Re=29,300, Re_{sub}=43,400, τ =30.75 second

The major features of the Nu/Nu_0 distributions on the front walls with the 30 deg model in the channel are almost identical to that with 45 deg model. The legs of the long fins work as ribs and enhance the heat transfer in the adjacent downstream areas; and the heat transfer enhancement is also observed in narrow areas along the upper partial of the short fins and in the areas over the tips of short fins. However, by comparing Figure 7.7(c) and Figure 7.9 (c) where the Reynolds numbers are almost the same, it is evident that the 30 deg model generates a slightly lower heat transfer on the front wall that the 45 deg model does. And it is worthy to point out that in Figure 7.9(b) and 7.9(c), the heat transfer enhancement generated by the side holes in the short fins is more noticeable than

that with 45 deg model. This is due to the enlarged size of the side holes in the 30 deg model.

.

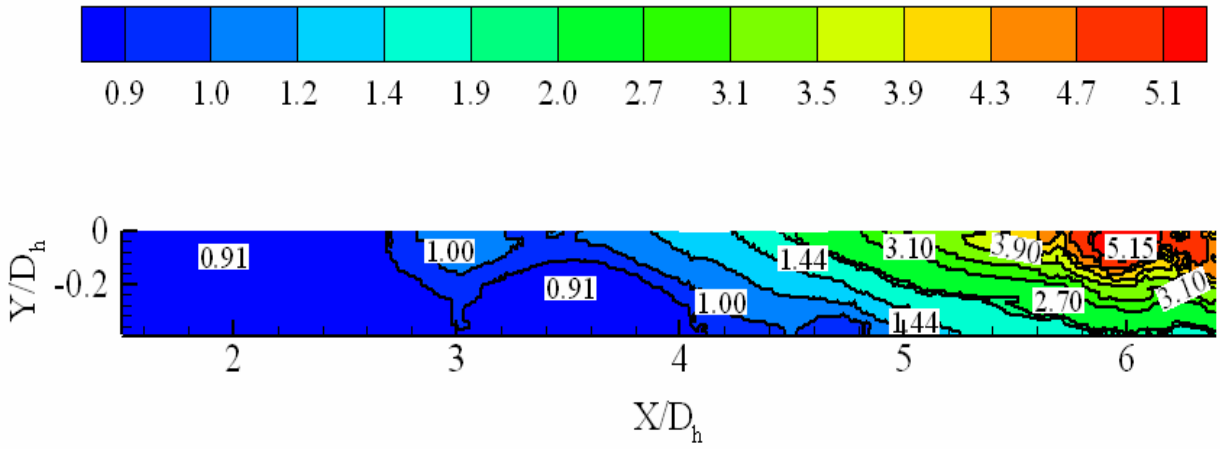

(a) Top wall (Re=29,300, Re_{sub}=43,400)

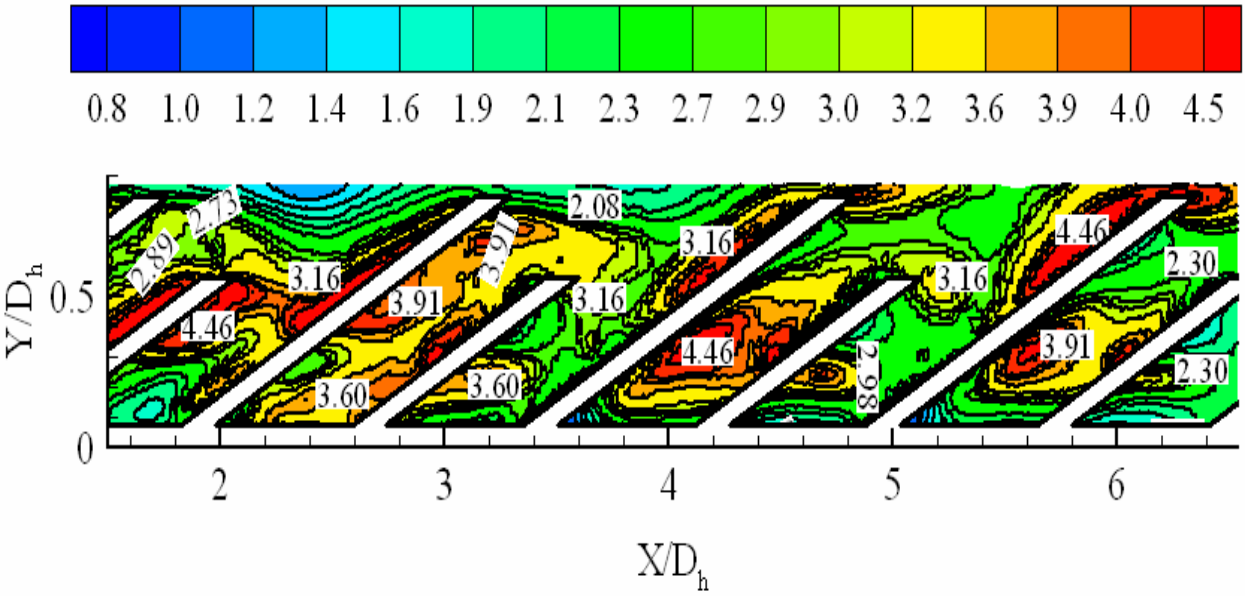

(b) Front wall (Re=29,300, Re_{sub}=43,400)

Figure 7.9: Nu/Nu_0 on the front wall and top wall (Figure continued)

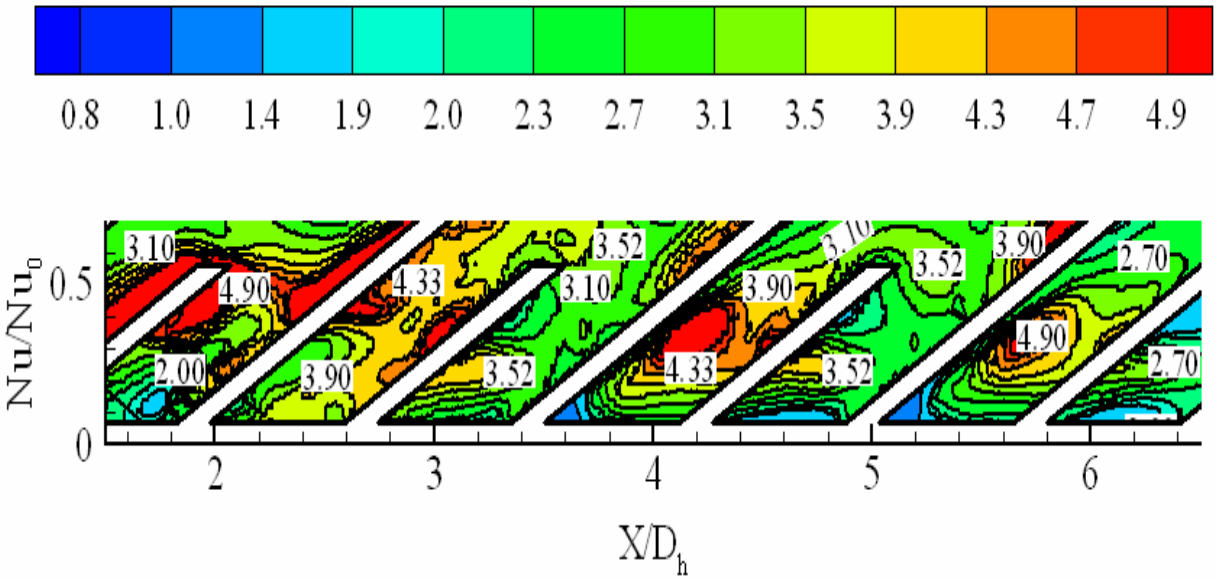

(b) Front wall (Re=18,940, Re_{sub}=27,690)

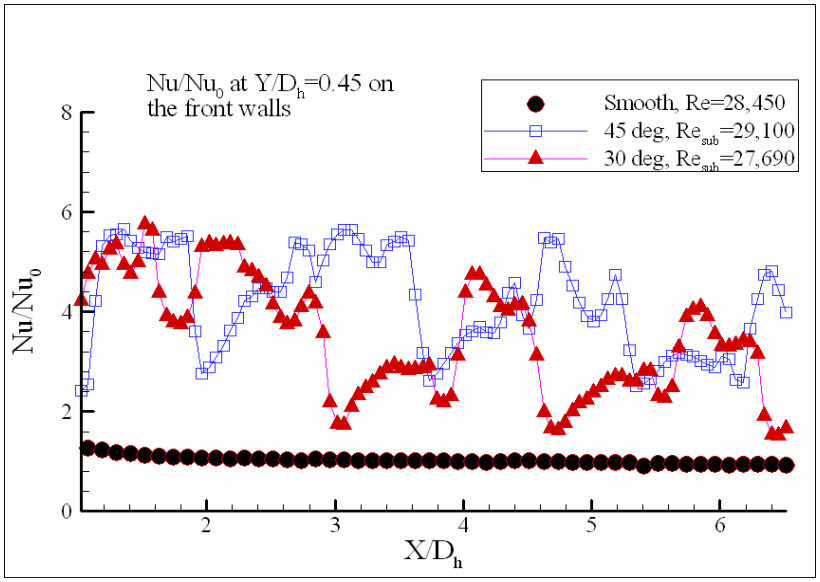

Figure 7.10: Local Nu/Nu_0 distributions along the streamwise direction

Figure 7.10 provides another view for the Nu/Nu_0 distributions. It shows the local Nu/Nu_0 distributions along the streamwise direction on front wall (Y/D_h=0.45, passing

the middle hole in the long fins of the 30 deg and 45 deg models) for the three test cases. In Figure 7.10(b) the periodical peak Nu/Nu_0 values correspond to the middle holes on the long fins, which can reach to the range between 5.5 and 5.75. Notice that the streamwise locations of the long fins and the shorts of the two models are not the same: the first fin of the 45 deg model is a short fin, while the 30 deg model starts with a long fin.

The average Nu/Nu_0 is shown in Figure 7.11. The average Nu/Nu_0 is obtained by averaging the Nu/Nu_0 value at each pixel in the images of the top wall and front wall. As mentioned above, Nu/Nu_0 is always based on the sub channels for the walls with models installed, so the Reynolds numbers shown is also based on the sub channels for the cases with models installed. It is easy to see that the average Nu/Nu_0 for smooth walls is close to unity as expected, and the average Nu/Nu_0 on the walls with models is enhanced to 3 or above. The 45 deg model generates the highest average Nu/Nu_0.

Keep in mind that the present experiment is performed with non-thermal-conductive plastic models, while in realistic applications the models will be turned into high conductive metallic devices cast together with the front and back walls. Considering the intentionally-designed large heat transfer areas in these models, even higher average Nu/Nu_0 is promising with metallic devices in real applications.

(3) Friction Factor and Thermal Performance Factors

The pressure drop along the streamwise direction is measured in the smooth channel and in the channels with models installed. It is found that, at the same Reynolds

number based on the main channel, the 30 deg model induces about 50% pressure drop (not shown here) compared to that found with the 45 deg model.

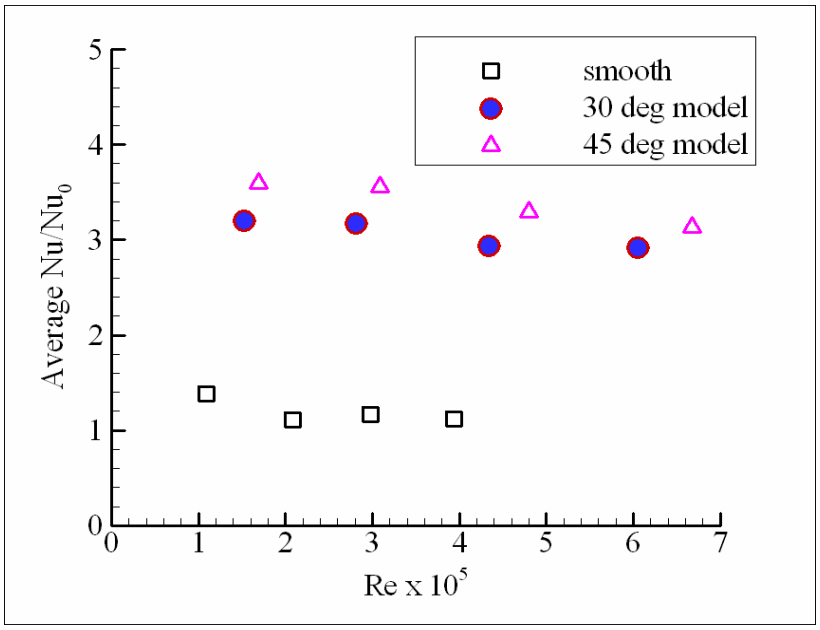

Figure 7.11: Average Nu/Nu_0

The friction factor, fr, is calculated by:

$$fr = (\Delta P \cdot D_h)/(4L \cdot \tfrac{1}{2} \cdot \rho \cdot V^2) \qquad (4)$$

where Δp is the pressure drop, L is the distance (1 foot in the present study) along which Δp is measured, ρ is the flow density, and V is the mean velocity of the flow. Then fr is normalized by the Karman-Nikuradse equation [15], $fr_0 = 0.046 \cdot Re^{-0.2}$:

$$fr/fr_0 = (\Delta P \cdot D_h)/(4L \cdot \tfrac{1}{2} \cdot \rho \cdot V^2 \cdot 0.046\, Re^{-0.2}) \qquad (5)$$

The friction factors are shown in Figure 12. The fr/fr_0 for the smooth channel is close to unity as expected. It is 14 to 17.5 for the 30 deg model, and 20.5 to 26.5 for the 45 deg model.

The thermal performance factor TPF is calculated by:

$$TPF = (Nu/Nu_0)/ (fr/fr_0)^{1/3} \qquad (6)$$

The resulted thermal performance factors are shown in Figure 13. The TPF for the two models are slightly greater than the smooth channel.

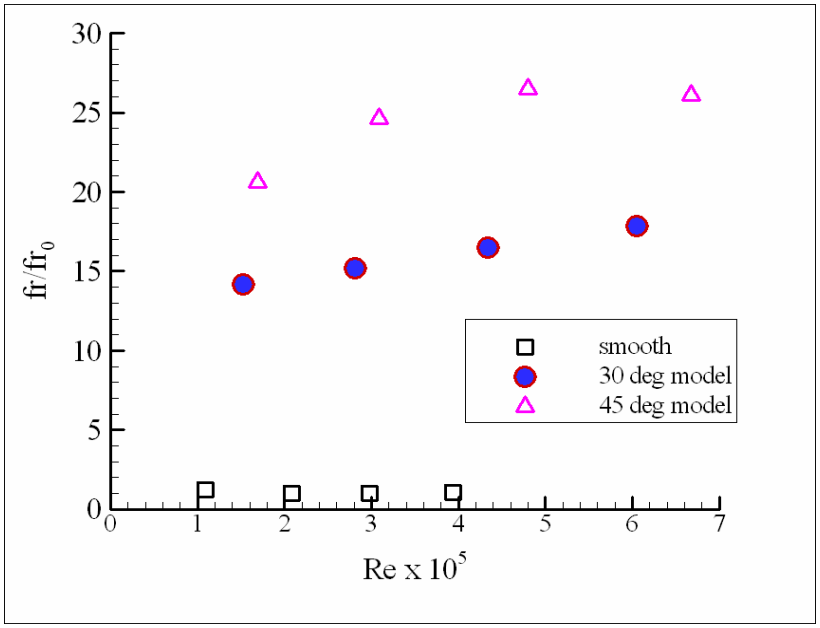

Figure 7.12: Friction factors

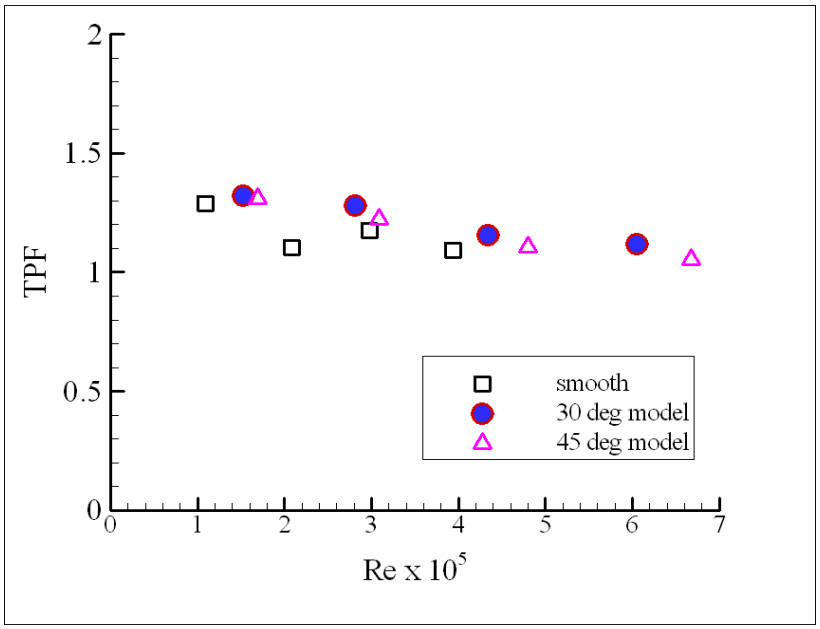

Figure 7.13: Thermal performance factors

7.5 Conclusion Remarks

The present study presents two fined passages with 30 deg and 45 deg non-conductive fins attached on the front and back walls, respectively. Heat transfer measurement on the inner channel walls are performed with transient crystal technique. It is found that in the two fined passages, the overall average Nu/Nu_0 is enhanced to 3 and above. On the front walls, the areas of heat transfer enhancement are indentified and related to the fin structure. On the top wall, the Nu/Nu_0 is observed to be enhanced dramatically for the passage where very narrow gap between the tips and the top wall is designed, the local Nu/Nu_0 reaches to more than 11 at specific locations. Pressure drop is measured as well, and friction factors and thermal performance factors are provided.

Considering the realistic application where the cooling channel and cooling devices are all metallic, the heat conduction will contribute a significant part to the overall heat transfer, and the overall heat transfer of the present devices can be even better benefited from the intentionally-designed large heat exchange areas. Further experiments are required to verify the overall heat transfer and thermal performance.

CHAPTER 8

CONCLUSIONS

The major conclusions of this dissertation are summarized below.

1. Rotation Experiments on the AR 4:1 Channels

Three models with smooth, 90 deg ribbed and 45 deg ribbed channels of aspect ratio 4:1 are compared in this chapter. The following major conclusions are drawn

1. Ribbed stationary channels show about 3 times of heat transfer ratio compared to the smooth channel.
2. On the destabilized surfaces (inlet trailing and outlet leading walls), rotation produces a significant enhancement of heat transfer in the inlet of the three models, while in the outlet, this enhancement is almost unnoticeable for the ribbed models.
3. On the stabilized surfaces (inlet leading and outlet trailing walls), rotation reduced heat transfer in both inlet and outlet channels of the two ribbed models, except at high Ro number for 45 deg ribbed inlet-leading wall, where heat transfer increases as Ro reaches to 0.4 and goes beyond. While on the smooth inlet-leading wall, a strong heat transfer enhancement is observed at lower Re numbers (Re=10, 000 and Re=20,000), but this enhancement is not observed at high Re numbers ($Re \geq 40{,}000$) on the same surface. On the smooth outlet-trailing wall, heat transfer enhancement is also noticed at high Ro numbers at Re=10,000 and Re=20,000.

4. In general, smooth channel shows higher rotation effects than the ribbed channels. That is, the heat transfer ratio changes more in the smooth channel compared to the ribbed channels in the same range of Ro number.
5. The three models have the same smooth bend. The heat transfer on the bend does not show significant difference as in the inlet and outlet channels.
6. Higher density ratio DR enhances heat transfer on both leading and trailing walls of the inlet, bend and outlet for the three models.
7. Buoyancy parameter Bo is observed to correlate the Nu/Nu_0 data reasonably well. This correlation is stronger on the inlet-trailing walls,
8. The thermal performance factors (TPF) are calculated for stationary cases. The smooth and 45 deg ribbed models show a TPF about 1.3 when $Re \geq 40{,}000$, while the TPF of the 90 deg ribbed channel drops from 1.2 to less than 1.0 in the range of Re number from 10, 000 to 70,000.

2. Finned Passages

Two fined passages with 30 deg and 45 deg non-conductive fins attached on the front and back walls are studied, respectively. Heat transfer measurement on the inner channel walls are performed with transient crystal technique. It is found that in the two fined passages, the overall average Nu/Nu_0 is enhanced to 3 and above. On the front walls, the areas of heat transfer enhancement are indentified and related to the fin structure. On the top wall, the Nu/Nu_0 is observed to be enhanced dramatically for the passage where very narrow gap between the tips and the top wall is designed, the local Nu/Nu_0 reaches to more than 11 at specific locations. Pressure drop is measured as well, and friction factors and thermal performance factors are provided.

Considering the realistic application where the cooling channel and cooling devices are all metallic, the heat conduction will contribute a significant part to the overall heat transfer, and the overall heat transfer of the present devices can be even better benefited from the intentionally-designed large heat exchange areas. Further experiments are required to verify the overall heat transfer and thermal performance.

REFERENCES

[1] Mori, Y., Fukada, T., and Nakayama, W., 1971, "Convective Heat Transfer in a Rotating Circular Pipe (2nd Report)", *Int. J. Heat Mass Transfer*, 14, pp. 1807-1824.

[2] Metzger, D. E., and Stan, R. L., 1977, "Entry Region Heat Transfer in Rotating Radial Tubes", *AAIA paper* No. 77-189.

[3] Morris, W. D., and Ayhan, T., 1979, "Observations on the Influence of Rotation On Heat Transfer in the Cooling Channels of Gas Turbine Rotor Blades," *Proc. Inst. Mech. Engrs.*, Vol. 193, pp. 303-311.

[4] Wagner, J.H., Johnson, B.V., and Hajek, T.J., 1991, "Heat Transfer in Rotating Passages with Smooth Walls and Radial Outward Flow", *Journal of Turbomachinery*, 113, pp. 42-51.

[5] Wagner, J. H., Johnson, B. V., and B.V., Kopper, F.C., 1991, "Heat Transfer in Rotating Serpentine Passages With Smooth Walls," *Journal of Turbomachinery*, 113, pp 321-330.

[6] Wagner, J. H., Johnson, B. V., Graziani, R. A., and Yeh, F. C., 1992, "Heat Transfer in Rotating Serpentine Passages With Trips Normal to the Flow", *Journal of Turbomachinery*, 114, pp 847-857.

[7] Johnson, B. V., Wagner, J. H., Steuber, G. D., and Yeh, F. C., 1994, "Heat Transfer in Rotating Serpentine Passages With Trips Skewed to the Flow", *Journal of Turbomachinery*, 116, pp 113-123.

[8] Guidez, J., 1989, "Study of the Convective Heat Transfer in a Rotating Coolant Channel," *Journal of Turbomachinery*, 111, pp. 43-51.

[9] Morris W. D., and Ghavami-Nasr, G., 1991, "Heat Transfer Measurements in Rectangular Channel With Orthogonal Mode Rotation," *Journal of Turbomachinery*, 113, pp. 339-345.

[10] Iacovides, H., and Launder, B. E., 1991, "Parametric and Numerical Study of Fully Developed Flow and Heat Transfer in Rotating Rectangular Ducks," *Journal of Turbomachinery*, 113, pp. 331-338.

[11] Soong, C. Y., Lin, S. T., and Hwang, G., J., 1991, "An Experimental Study of Convective Heat Transfer in Radially Rotating Rectangular Ducts," Journal *of Heat Transfer*, 113, pp. 604-611.

[12] Han, J. C., park, J. S., and Ibrahim, M. Y., 1986, “Measurement of Heat Transfer and Pressure Drop in Rectangular Channels With Turbulence Promoters”, NASA CR 4015

[13] Griffith, T. S., Al-Hadhrami, L., and Han, J. C., 2002, “Heat Transfer in Rotating Rectangular Cooling Channels (AR = 4) with Angled Ribs,” *Journal of Heat Transfer*, 124, pp 1-9

[14] Iacovides, H., 1998, “Computation of Flow and Heat Transfer Through Rotating Ribbed Passages.” *International Journal of Heat and Fluid Flow,* Vol. 19, pp. 393-400.

[15] Kays, W. M., and Crawford, M. E., 1993, Convective Heat and Mass Transfer, Third Edition, McGraw Hill

[16] Kline, S. J., and McClintock, F. A., 1953, “Describing Uncertainties in Single-sample Experiments,” *Mech. Engineering*, Vol. 75, No. 1, pp. 3-8.

[17] Johnson, B. V., Wagner, J. H., and Steuber, G. D., 1993, “Effects of Rotation on Coolant Passage Heat Transfer, Volume II—Coolant Passages With Trips Normal and Skewed to the Flow”, NASA CR 4396

[18] Willett, F. T., and Bergles, A. E., “Heat Transfer in Rotating Narrow Rectangular Ducts With Heated Sides Oriented at 60 deg to the R-Z Plan,” J*ournal of Turbomachinery.*, 123, pp. 288–295; ASME Paper No. 2000-GT-224.

[19] Rache, P. H., and Johnston, J. P., 1979, “Free Shear Layer Behaviors in Rotating System”, ASME *Journal of Fluids Engineering*, Vol. 101, pp. 117-120

[20] Mochizuki, S., Takamura, J., Yamawaki, S., and Yang, Wen-Jei, 1994, “Heat Transfer in Serpentine Flow Passages with Rotation,” Journal of Turbomachinery, Vol. 116, pp. 133-140.

[21] Han, J. C., 1984, “Heat Transfer and Friction in Channels with Two Opposite Rib-Roughened Walls”, *ASME Journal of Heat Transfer*, Vol. 106, Nov., pp 774-784

[22] Han, J.C. and Park, J. S., 1988, “Developing Heat transfer in Rectangular Channels with Rib Turbulators.” *International Journal of Heat and Mass Transfer,* Vol. 31, No. 1, pp 183-195.

[23] Han, J. C., Dutta, S., and Ekkad, S., 2000, Gas Turbine Heat Transfer and Cooling technology, Taylor and Francis, New York.

[24] Han, J. C., and Zhang, P., 1991, “Effects of Rib-Angle Orientation on Local Mass Transfer Distributions in a Three-Pass Rib-Roughened Channel”, *Journal of Turbomachinery*, Vol.113, pp 123-130.

[25] Liou, T. M., Chang, Y. and Huang, D. W., 1990, "Experimental and Computational Study of Turbulent Flows in a Channel with Two Pairs of Turbulence Promoters in Tandem", *Journal of Turbomachinery*, Vol.112, pp 302-310.

[26] Liou, T. M. and Huang, D. W., 1992, "Turbulent Heat Transfer Augmentation and Friction in Periodic Fully Developed Channel Flows", *Journal of Turbomachinery*, Vol.114, pp 56-64.

[27] Taslim, M. E., Li, T. and Kercher, D. M., 1996, "Experimental Heat Transfer and Friction in Channels Roughed with Angled, V-Shaped, and Discrete Ribs on Two Opposite Walls", Journal *of Turbomachinery*, Vol. 118, pp 20-28.

[28] Taslim, M. E., Li, T. and Spring, S. D., 1998, "Measurement of Heat Transfer Coefficients and Friction Factors in Passages Rib-Roughed on All Walls", *Journal of Turbomachinery*, Vol. 120, pp 564-570.

[29] Acharya, S., Myrum, T., Qiu, X., and Sinha, S., 1997, "Developing and Periodically Developed Flow, Temperature and Heat Transfer in a Ribbed Duct", International Journal *of Heat and Mass Transfer*, Vol. 40, pp 461-479

[30] Talslim, M. E., Rahman, A. and Spring, S. D., 1991, "An Experimental Investigation of Heat Transfer Coefficients in a Spanwise Rotating Channel with Two Opposite Rib-Roughed Walls", *Journal of Turbomachinery*, Vol.113, pp 75-82.

[31] Hart, J. E., 1971, "Instability and Secondary Motion in a Rotating Channel Fflow", *Journal of Fluid Mechanics*, vol. 45, pp 341-351.

[32] Johnston, J. P., Halleen, R. M., and Lezius, D. K., 1972, "Effects of Spanwise Rotation on the Structure of Two-Dimensional Fully Developed Turbulence Channel Flow", *Journal of Fluid Mechanics*, Vol. 56, pp 533-557.

[33] Acharya, S., Dutta, S., Myrum, T.A., and Baker, R.S., 1993, "Periodically Developed Flow and Heat Transfer in a Ribbed Duct." *International Journal of Heat and Mass Transfer*, Vol. 36, No. 8, pp 2069-2082.

[34] Dutta, S., Andrews, M. J., and Han, J. C., 1996, "Prediction of Turbulent Heat Transfer in Rotating Smooth Square Ducts", *International Journal of Heat and Mass Transfer*, Vol. 39, pp 2505-2514.

[35] Saha, A. and Acharya, S., 2004, "Unsteady RANS Simulations of Turbulent Flow and Heat Transfer in Ribbed Coolant Passages of Different Aspect Ratios," GT2004 53986

[36] Murata, A., and Mochizuki, S., 2004, "Centrifugal buoyancy effect on turbulent heat transfer in a rotating two-pass smooth square channel with sharp 180-deg turns", *International Journal of Heat and Mass Transfer,* Vol. 47, pp 3215-3231.

[37] Murata, A., and Mochizuki, S., 2004, "Aiding and opposing contributions of centrifugal buoyancy on turbulent heat transfer in a two-pass transverse- or angled-rib-roughened channel with sharp 180° turns", *International Journal of Heat and Mass Transfer,* Vol. 47, pp 3721-3743.

[38] Sleiti, A. K., and Kapat, J.S., 2004, "Fluid Flow and Heat Transfer in Rotating Curved Duct at High Rotation and Density Ratios" GT2004-53028, *Proceedings of ASME Turbo Expo 2004, Power for Land, Sea, and Air,* June 14-17, 2004, Vienna, Austria.

[39] Sleiti, A. K., and Kapat, J.S., 2004, "Effect of Coriolis and Centrifugal Forces on the Turbulence and Heat Transfer at High Rotation and Buoyancy Numbers in a Rib-Roughened Internal Cooling Channel." GT2004-53018, *Proceedings of ASME Turbo Expo 2004, Power for Land, Sea, and Air,* June 14-17, 2004, Vienna, Austria.

[40] Ligrani, P. M., Harrison, J. L., Mahmood, G. I., and Hill, M. L., 2001, "Flow structure due to Dimple Depression on a Channel Surface," *Physics of Fluids,* Vol. 13, pp. 3442-3451.

[41] Ligrani, P. M., Mahmood, G. I., Harrison, J. L., Clayton, C. M., and Nelson, D. L., 2001, Flow Structure and Local Nusselt Number Variations in a Channel with Dimples and Protrusions on Opposite Walls," *International Journal of Heat and Mass Transfer,* Vol. 44, , pp. 4413-4425.

[42] Schukin, A. V., Koslov, A. P., and Agachev, R. S., 1995, "Study and Application of Hemispheric Cavities for Surface Heat Transfer Augmentation," *ASME Paper No. 95-GT-59, ASME 40th Intl. Gas Turbine and Aeroengine Congress and Exhibition*, Houston, Texas, U.S.A.

[43] Terekhov, V. I., Kalinina, S. V., and Mshvidobadze, Yu. M., 1997, "Heat Transfer Coefficient and Aerodynamic Resistance on a Surface with a Single Dimple," *Enhanced Heat Transfer,* Vol. 4, pp. 131-145.

[44] Chyu, M. K., Yu, Y., Ding, H., Downs, J. P., and Soechting, F., 1997, "Concavity Enhanced Heat Transfer in an Internal Cooling passage," *ASME Paper No. 97-GT-437, ASME 42nd Intl. Gas Turbine and Aeroengine Congress and Exhibition,* Orlando. Florida, U.S.A.

[45] Lin, Y. l., Shih, T. I. P., and Chyu, M. K., 1999, "Computations of Flow and Heat Transfer in a Channel with Rows of Hemispherical Cavities," *ASME paper No. 99-GT-263, ASME 44th Intl. Gas Turbine and Aeroengine Congress and Exhibition,* Indianapolis, Indiana, U.S.A.

[46] Moon, H. K., O'Connell, T., and Glezer, B., 1999, "Channel Height Effect on Heat Transfer and Friction in a Dimpled Passage," ASME paper No. 99-GT-163, *ASME 44th Intl. Gas Turbine and Aeroengine Congress and Exhibition,* Indianapolis, Indiana, U.S.A.

[47] Moon, H. K., O'Connell, T., and Sharma, R., 2002, "Heat Transfer Enhancement Using a Convex-Patterned Surface," *Paper No. GT-2002-30476, Proceedings of ASME Turbo Expo 2002,* Amsterdam, the Netherlands.

[48] Mahmood, G. I., Hill, M. L., Nelson, D. L., Ligrani, P. M., Moon, H. K., and Glezer, B., 2001, "Local heat transfer and Flow Structure on and Above a Dimpled Surface in a Channel," *Journal of Turbomachinery,* Vol. 123, No. 1, pp. 115-123.

[49] Mahmood, G. I., and Ligrani, P. M., 2002, "Heat Transfer in a Dimpled Channel: Combined Influences of Aspect Ratio, Temperature Ratio, Reynolds Number, and Flow Structure," *International Journal of Heat and Mass Transfer,* Vol. 45, No. 10, pp. 2011-2020.

[50] Burgess, N. K., Oliveira, M. M., and Ligrani, P. M., 2003, "Nusselt Number Behavior on Deep Dimpled Surfaces within a Channel," *Journal of Heat Transfer,* Vol.123, pp. 11-18.

[51] Griffith T. S., Al-Hadhrami L, and Han, J. C., 2003, "Heat Transfer in Rotating Rectangular Cooling Channels (AR=4) with Dimples", *Journal of Turbomachinery,* Vol. 125, pp. 555-564.

[52] Choudhury, D., and Karki, K. C., 1991, "Calculation of fully developed flow and heat transfer in streamwise-periodic dimpled channels," *Journal of Thermophysics and Heat Transfer,* Vol 5, n 1, p 81-88.

[53] Isaev, S. A., Leontiev, A. I. and Baranov, P. A., 2001, "Identification of Self-Organized Vortexlike Structures in Numerically Simulated Turbulence Flow of a Viscous Incompressible Liquid Streaming Around a Well on a Plane," Turbulence Physics Letters, Vol. 26, No. 1, pp. 15-18.

[54] Isaev, S. A., Leontiev, A. I., Kudryavtsev, N. A., and Pyshnyi, I. A., 2003, "The Effect of Rearrangement of the Vortex Structure on Heat Transfer under Conditions of Increasing Depth of a Spherical Dimple on the Wall of a Narrow Channel,", *High Temperature*, Vol. 41, No. 2, 2003, pp. 229–232. (Translated from Teplofizika Vysokikh Temperatur, Vol. 41, No. 2, 2003, pp. 268–272).

[55] Isaev, S. A. and Leontiev, A. I., 2003, "Numerical Simulation of Vortex Enhancement of Heat Transfer under Conditions of Turbulent Flow Past a Spherical Dimple on the Wall of a Narrow Channel," *High Temperature,* Vol. 41, No. 5, 2003, pp. 665–679. (Translated from Teplofizika Vysokikh Temperatur, Vol. 41, No. 5, 2003, pp. 755–770).

[56] Acharya, S., Zhou, F., Lagrone, J;, Mahmood, G., and Bunker, R. S. , 2005, "Latticework (Vortex) Cooling Effectiveness: Rotating Channel Experiments",*ASME Journal of Turbomachinery,* Vol. 127, pp 471-478.

[57] Bunker, R.S., 2004, "Latticework (Vortex) Cooling Effectiveness Part 1: Stationary Channel Experiments", Paper No GT-2004-54157, IGTI Turbo Expo, Vienna.

[58] Van Fossen G. J.. 1982,"Heat Transfer Coefficients For A Staggered Array Of Short Pin Fins", Journal of Engineering for Power, Vol. 104, pp. 268-274.
Simoneau R. J., Van Fossen G. J. Jr., 1984,"Effects Of Location In An Array On Heat Transfer To A Short Cylinder In A Crossflow", Journal of Heat Transfer, Vol. 106, pp. 42-48.

[59] Chyu M. K., Natarajan V., 1992,"Heat/Mass Transfer From Pin Fin Arrays With Perpendicular Flow Entry", ASME Heat Transfer Division, Vol. 226, pp. 31-39.

[60] Zhou, F., and Acharya, S., 2001, "Mass/Heat Transfer in Dimpled Two-Pass Coolant Passages with Rotation", Annals of the New York Academy of Sciences, Vol. 934, pp 424–431.

[61] Lagrani, P. M., Oliveira, M. M., and Blaskovich, T., 2003, "Comparison of Heat Transfer Augmentation Techniques," *AIAA Journal,* Vol. 41, No. 3, pp. 337-772.

[62] Zhou, F., Lagrone, J., and Acharya, S., 200, "Internal Cooling in 4:1 AR Passages at High Rotation Numbers", *Journal of Heat Transfer,* Vol.129, pp 1666-1675.

[63] den Ouden, C. and Hoogerdoom, C. J.. 1974, "Local Convective Heat transfer Coefficients for Jets Impinging on a Plate. Experiments using a Liquid Crystal Technique", *Heat Transfer, Proceedings of the 5th Int. Heat Transfer Conf.*, Vol. V, Tokyo, Japan, pp 293-297.

[64] Cooper, T. E., Field, R. J., and Meyer, J. F., 1975, "Liquid Crystal Thermography and its Application to the Study of Convective Heat Transfer", *Journal of Heat Transfer*, Vol. 97, Vol. 3, pp 442-450 .

[65] Moffat, R. J. 1990, "Experimental Heat Transfer," *Proceedings of the 9th International Heat Transfer Conference, Jerusalem,* Israel, Vol. 1, pp 187-205.

[66] Jones, T. V., 1992, "The Use of Liquid Crystals in Aerodynamic and Heat Transfer Testing," *Transport Phenomena in Heat and Mass Transfer (ISTP-IV), J. A. Reizes, ed,* Amsterdam, Elsevier, NY, pp 1242-1273.

[67] Baughn, J. W., 1995, "Liquid crystal methods for studying turbulent heat transfer," *International Journal of Heat and Fluid Flow*, Vol. 16, Issue 5, pp 365-375.

[68] Hollingworth, D. K., Boehman, A. L., Smith, E. G., and Moffat, R. J., 1989, "Measurement of Temperature and Heat Transfer Coefficient Distributions in a Complex Flow Using Liquid Crystal Thermography and True-Color Image Processing," *ASME Collected Papers in Heat Transfer, HTD*, Vol. 123, pp 35-42.

[69] Camci, C., Kim, K., and Hippensteele, S. A., 1992, "A New Hue Capturing Technique for the Quantitative Interpretation of Liquid Crystal Images Used in Convective Heat Transfer Studies", *Journal of Turbomachinary*, Vol 114, pp 765-775.

[70] Wang, Z., Ireland, P. T. and Jones, T. V., 1991, "A Technique for Measuring Convective Heat Transfer at Rough Surface," *Trans. Inst. Meas. Control*, Vol. 13, pp 145-154.

[71] Ireland, P. T. and Jones, T. V., 2000, "Liquid Crystal Measurement of Heat Transfer and Surface Shear Stress", *Meas. Sci. Technol.* Vol. 11, pp 969-986.

[72] Al-Hadhrami, Luai and Han, J. C., 2003, "Effect of Rotation on Heat Transfer in Two-Pass Square Channels with Five Different Orientations 0f 45^0 Angled Rib Turbulators", *International Journal of Heat and Mass Transfer*, Vol. 46, pp 653-669.

VITA

Fuguo Zhou was born in Hunan Province in China. He received the Bachelor of Science in Aerospace Engineering (Jet Propulsion) from Beijing University of Aeronautics and Astronautics, Beijing, China, in 1985; and he received the Master of Science in Aerospace Engineering (Rocket Propulsion) from Beijing University of Aeronautics and Astronautics in 1988. Then he worked as an instructor in a university in Wuhan, Hubei Province, and studied one year in Purdue University, West Lafayette, Indiana. He then joined the graduate program at Louisiana State University, Baton Rouge, in fall, 1999. He worked as a research assistant in Turbine Innovation and Energy Research (TIER) Center on experimental and numerical studies on internal cooling in turbine blades. He received the degree of Master of Science in Mechanical Engineering from Louisiana State University in the summer 2007. Since December of 2007, he has been working in an engineering company in Baton Rouge as a mechanical engineer.